Building blocks for cavity quantum electrodynamics in on-chip buckled dome microcavities

by

Sanaa Al-Sumaidae

A thesis submitted in partial fulfillment of the requirements for the degree of

Doctor of Philosophy

in

Photonics and Plasmas

Department of Electrical and Computer Engineering
University of Alberta

Abstract

Technologies for controlling spontaneous emission have attracted considerable attention over the past few decades, and have most recently been concerned with the realization of several quantum light sources such as the threshold-less laser and the controlled source of single photons. The emission rate and directivity of an atomic emitter can be modified through the appropriate design of the surrounding electromagnetic environment. Optical microcavities play a central role in efforts to modify the spontaneous emission rate. The interaction between a cavity mode and an emitter can lead to an enhanced rate of emission into a desired mode and/or a suppressed /inhibited rate of emission into undesired modes.

This research is mainly a theoretical and experimental study of the control/modification of the spontaneous emission rates for dipole emitters embedded inside 'half-symmetric' curved-mirror Fabry Perot cavities with omnidirectional mirror claddings. These cavities are fabricated using a monolithic 'buckling' self-assembly process. In theoretical work, we demonstrated that omnidirectional Bragg reflectors can enable significant inhibition of background emission, and thus might greatly enhance the single-atom cooperativity and the spontaneous emission coupling factor into a desired mode of such cavities. In experimental work, we explored monolithic strategies to embed various emitters, including erbium-doped thin films, inside these cavities. Preliminary evidence for cavity-enhanced emission was achieved, although further optimization of these fabrication strategies is left for future work.

The upper mirror in buckled dome microcavities is essentially a flexible membrane, offering unique options for tuning the resonance spectra. Resonance tuning is a pre-requisite for many cavity quantum electrodynamics (CQED) applications, such as those mentioned above. From another perspective, the shift in cavity resonance in response to changes in ambient pressure and

temperature can be viewed as a modality for optical sensing. The feasibility of utilizing such cavities as optical pressure sensors was investigated experimentally and theoretically, for two different sizes of buckled dome cavities with a-Si/SiO$_2$-based mirrors. These studies showed the potential for high sensitivity (< 10 Pa), and good linearity over a pressure range > 100 kPa for domes of 100 and 50 μm base diameters. We also measured the mechanical resonance frequencies for those domes, confirming theoretical predictions that the fundamental resonance frequencies lie in the MHz range. With potential for high-speed response and on-chip fabrication in large arrays, buckled dome microcavities might be an interesting candidate for dynamic pressure sensing applications such as photo-acoustic imaging. On the other hand, this study also suggests that rapid tuning of the optical resonance might be possible through control of the external pressure, a property which might be useful for some CQED applications such as the single-photon sources mentioned above.

Preface

Various part of this thesis has been published in a peer-reviewed journals and also presented at the conference. A version of chapter 3 has been published as S. Al-Sumaidae, M. H. Bitarafan, C. A. Potts, J. P. Davis, and R. G. DeCorby. "Cooperativity enhancement in buckled-dome microcavities with omnidirectional claddings". *Optics Express*, vol 26, no.9 pp. 11201, 2018. I was responsible for the writing of the script for the Lumerical simulation, and data analysis. M. H. Bitarafan, C. A. Potts, J. P. Davis helped in the editing. R. G. DeCorby was the supervisory author and was involved in concept information, theoretical and manuscript preparation.

Chapter 5 in this thesis has been published as S. Al-Sumaidae, L. Bu, G. J. Hornig, M. H. Bitarafan, and R. G. DeCorby. "Pressure sensing with high-finesse monolithic buckled dome microcavities". *Applied Optics*, vol. 60, no.29, 2021. I was responsible for the optical measurements, data collection and analysis, and manuscript preparation. L.Bu helped in designing the chamber and set up preparation. G. J. Hornig, M. H. Bitarafan, provided the comments. G. DeCorby was the supervisory author and was involved in concept information, theoretical and manuscript preparation.

Acknowledgments

Quite a few people supported my effort to accomplish the goals of the current work. So, I would like to express my deepest thanks to those who helped and encouraged me to be persistent in the way for this thesis.

I would like to recognize the invaluable assistance of Dr. Ray DeCorby. His patience, enthusiasm, cooperation, and suggestions made me present this research work to produce in the present form. This research work would not be possible without hit stimulation inspiration and cooperation. I am extremely grateful that you took me on as a student and continued to have faith in me over the years.

I would like to express my deepest appreciation to my committee, Prof. Ying Tsui, Prof. Manisha Gupta, Prof. Vein Van, Prof. Al Meldrum, and Prof. Safa Kasap, for their comments and feedback. In addition, I'm deeply indebted to Prof. Al Meldrum at the Department of Physics for allowing me to do many depositions in his lab. In particular, I would like to thank technician Mr. Greg for assisting in the deposition.

To all members of the integrated Optics Lab, I am extremely thankful for your valuable suggestions, ever encouraging, motivating guidance, and lively discussion. I would like to thank Danny Pulikkaseril, James Maldaner, Lintong Bu, Timothy Harrison, Graham Hornig, Kyle Scheuer, and Mohammad Bitarafan for providing additional knowledge in microfabrication techniques. You have each had a hand in this work.

I also want to thank all my friends whom I met at the University of Alberta. The years I have spent at the University of Alberta with them have been unforgettable.

Special thanks to Pinder Bains for being so cooperative and helpful through my graduate study

My special thanks to all the staff of the nanoFAB, particularly to Stephanie and Scott Munro, for providing me with their valuable suggestions regarding lithography and etching processes.

I would like to acknowledge the Iraqi Ministry of Higher Education and Scientific Research (IMHESR) for providing me with the scholarship to support my Ph.D. study at the University of Alberta.

Contents

List of Tables

List of Figures

Figure 3.1. (a) Microscope image of a portion of a large array of 50-μm-base-diameter domes. (b) Typical wavelength scan showing a fundamental resonance (at ~1610 nm for this particular cavity) and several higher-order transverse resonances. The solid lines are Lorentzian fits, and mode-field-intensity images associated with each resonance are

List of Symbols and Abbreviations

Symbols

A	Absorption.
c	Speed of light in vacuum.
C	Cooperativity.
d	Thickness of the film
d_H	Thickness of the higher index.
d_L	Thickness of the Low-index layer.
dp	Penetration depth
E	Young's modulus.
E_1	the upper energy levels of the atom.
E_2	lower energy levels of the atom.
F_p	Purcell factor.
F	Finesse.
F_R	Reflectance finesse.
g_0	Atom-cavity coupling rate.
g_1	Degeneracies of levels 1.
g_2	Degeneracies of levels 2.
h	Mirror thickness (Chapter 5)
$\hbar$	Planck constant.
I	Intensity profile (Chapter 2).
I_0	On-axis intensity at the beam waist
J_0	Bessel function of order zero and first kind.
k	Wave number.
k_0	Free-space wave number
$k_{//}$	In-plane component of the wave-vector
k_B	Boltzmann constant
k_q	Wave number in the cavity.
k_Z	Normal component of the wave vector in the air-core layer (Chapter 3).
K_0	Effective spring constant.
L	Length of a Fabry-Perot cavity.
$Leff$	Effective cavity length (chapter 4)
m	Longitudinal mode order (chapter 4 and chapter 6).
m_0	mass for the fundamental vibrational mode
n	Refractive index.
n_0	Refractive index of the input
n_H	Refractive index of the higher layer in the mirror.
n_L	Refractive index of the lower layer in the mirror.
n_s	Refractive index of the substrate
$N_{1,2}$	Number of atoms per unit volume in energy state $E_{1,2.}$
N	Number of layers.
q	Longitudinal mode number (chapter 2)
Q	Quality factor.

Q_{EM}	Effective quality factor of the emitter
R	Reflectance.
R_{Bragg}	Bragg reflectance.
$R(z)$	Radius of curvature of the phase front of a Gaussian beam.
R_{CD}	Radius of Curvature
r^+	Fresnel reflection coefficients at the interface between the air cavity and the upper.
r^-	Fresnel reflection coefficients at the interface between the air cavity and the lower mirror.
S_{Pl}	Pressure sensitivity.
$S_{P\lambda}$	Pressure response,
T	Transmission.
v	Poisson's ratio of the stacked layer.
V_m	Mode volume.
w_0	Minimum spot size of the beam waist.
$w(z)$	Spot size of the beam waist.
z_0	Rayleigh range
β	spontaneous emission coupling factor
γ	Non-resonant decay rate
γ_0	free-space emission rate
γ_{CLAD}	Emission rate into the cladding modes.
γ_C	Cavity mode Emission rate
δ	Peak height of the buckle dome.
δ_{v_m}	FWHM spectral linewidth of the resonance mode m.
Δv	frequency spacing between transverse modes
$\Delta(r)$	Profile of a circular delamination buckle.
$\Delta\lambda_T$	transverse mode spacing
$\Delta\lambda_{Bragg}$	Stop band of Bragg mirror.
$v_{l,q,m}$	Mode frequency spacing between higher order modes.
v	Frequency.
v_f	free spectral range
λ_B	Bragg wavelength
κ	the photon decay rate of the cavity
μ	first zero of the Bessel function of the first kind and order one.
σ	Film Stress.
σ_c	Critical film stress.
θ_B	Brewster's angle
ψ	potential transmittance
ϕ	Phase shift.
$\rho(\omega)$	spectral energy density of the electromagnetic field at the resonant frequency
ω_0	Vibrational resonance,
TL	(Tube lens),
BS	(Beam Splitter),
DM	(Dichroic Mirror),
LP	(long Pass Filter),

MO	Microscope Objective lens
FC	Fiber Collimator,
MMF	Multimode Fiber
GMMF	Grad Multimode Fiber
SP	Short Pass Filter

Abbreviations

1D	One-dimensional.
2D	Two-dimensional.
3D	Three-dimensional
a-Si	Amorphous silicon
CQED	cavity quantum electrodynamics
DBR	distributed Bragg reflector.
EFPI	extrinsic Fabry-Perot interferometers
FESEM	
FDTD	Finite difference time domain
FIB Focused ion beam	FIB Focused ion beam
FOM	figures of merit
FPC	Fabry-Perot cavity
FPI	Fabry-Perot interferometer
FSR	free spectral range
FWHM	full width at half-maximum.
HG	Hermite-Gaussian.
HWHM	Half width at half maximum
ICPRIE	inductively coupled plasma reactive ion-etching.
IPA	isopropal alcohol.
LAL	low-adhesion layer.
LEDs	Light-emitting diodes.
LDOM	local density of modes.
LG	Laguerre-Gaussian.
MEMS	MEMS Microelectromechanical systems.
NDs	Nanodiamonds.
NIR	near infrared.
PC	Photonic crystals
PVD	physical vapour deposition.
PL	Photoluminescent.
QD or qdot	quantum dots
QWS	quarter-wave stack.
RIE	reactive-ion etching.
RTA	rapid thermal annealing.
SEM	scanning electron microscope.
SiC	single-crystal silicon carbide
SiO:Er	Erbium doped silicon monoxide.

SNR	SNR Signal-to-noise ratio.
SPS	single-photon-sources.
TE	TE Transverse electric.
TM	TM Transverse magnetic.
VASE	variable-angle spectroscopic ellipsometer.
ZYGO	ZYGO NewView 5000 optical profilometer.

Chapter 1

Introduction

This thesis work encompassed theoretical and experimental studies of some potential applications for 'buckled dome' Fabry-Perot microcavities, which are a new class of on-chip optical resonators that emerged in 2011 [1]. Two main themes were explored. First, the use of these cavities as enablers for on-chip cavity quantum electrodynamics (cavity QED) systems was investigated through both a theoretical study of spontaneous emission by an embedded emitter and through experimental attempts to embed various candidate emitters. Second, a detailed study of the use of these cavities as pressure sensors was completed. While apparently disparate topics at first glance, a potential link can be drawn from the fact that cavity QED systems invariably require some means to tune the optical resonance of the cavities (i.e., into alignment with the emission frequency of an emitter), while the pressure sensitivity of the buckled dome cavities suggests one possible means for achieving such tunability.

Optical microcavities confine light to very small volumes at certain resonant frequencies. The optical cavity has become an indispensable tool in many applications such as quantum information [2–5], optical filtering [6], lasers [7], and sensing [8]. There are several important figures of merit (FOM) that are used to characterize an optical cavity. A key FOM is the so-called finesse ($\mathcal{F}$), which is roughly equivalent to the average number of 'round trips' that a resonant photon transits before being absorbed or leaking from the cavity. Finesse is closely related to the quality factor (Q), and both of these parameters are essentially measures of the temporal confinement of photons within the cavity. Another important FOM is the so-called spontaneous emission coupling factor (β), which is essentially the fraction of photons emitted (by an emitting 'atom' inside the cavity) into the desired cavity mode. This is an important parameter for characterizing the efficiency of light sources such as lasers, light-emitting diodes (LEDs), and single-photon sources (SPS). As discussed in more detail below, achieving high β generally requires that an emitter is confined inside a microcavity with a small mode volume and a high Q-factor.

The desire to improve the efficiency of light sources has prompted widespread studies of concepts for the enhancement of emission into the desired mode [9–11] or the suppression/inhibition of emission into undesired modes [12,13]. Activity in this field was greatly accelerated by the work of Yablonovitch [13], which introduced the concept of a photonic crystal. In principle, three-dimensional (3D) photonic crystals can be used for complete control of the electromagnetic environment surrounding an emitter and thus for completely controlling spontaneous emission. However, 3D photonic crystals have proven difficult to implement at optical frequencies because of the requirements for 3D micromachining on the nanometer-scale.

In general, spontaneous emission can be modified by engineering the electromagnetic boundary conditions surrounding the emitter, with 3D photonic crystals perhaps representing the ultimate but most complex solution. As first shown by Purcell [14], significant benefits can be gained by confining an emitter inside a small optical resonant cavity. From those experiments, a famous result is the so-called Purcell factor: $F_P = 3Q(\lambda/n)^3/4\pi^2 V_M$, where Q and V_M are the quality factor and mode volume respectively, and n is the refractive index of the cavity medium. In this form, the Purcell factor quantifies the enhanced rate of emission into a cavity mode (i.e. relative to the free-space emission rate), for an emitter that is perfectly aligned to the cavity mode. Perfect alignment implies a dipole emitter located at the peak of the modal electric field profile, and whose transition energy and polarization are also aligned with the cavity mode field. Furthermore, it is often the case that the cavity does not significantly inhibit emission into non-resonant modes, in which case follows the well-known result that $\beta \sim (F_P/F_P+1)$. This furthermore implies that high β can be achieved by confining the emitter to a cavity with small V_M and high Q.

This chapter will summarize some historical efforts towards the integration of microcavities having small mode volume and high finesse, including efforts to embed emitters inside the optical cavities. As a precursor to the work described in the last part of the thesis, a review of some works involving the use of optical cavities for pressure sensing is also provided.

1.1 Controlling spontaneous emission

The manipulation and control of light emission, and in particular the engineering and modification of spontaneous emission, has garnered much attention in the field of quantum optics. In nature, the majority of light comes from spontaneous emission, and one of the most fundamental examples of

this spontaneous emission process is the thermal radiation emitted by hot objects. Typically, light emitted via spontaneous emission is not directional and is not coherent (i.e., it is a collection of 'wavetrains' having a random phase and central frequency distributed over some range). However, the dynamics of spontaneous emission can be influenced or controlled by placing the emitter inside an acceptable micro- or nano-structure that has a relevant dimension either on the wavelength- or sub-wavelength-scale. Thus, spontaneous emission is not a fixed property of an emitter. Instead, it is dependent on the electromagnetic environment in which the emitter is located. In fact, quantum mechanics shows us that spontaneous emission can be viewed as the emission of a photon mediated (or stimulated) by zero-point energy (viz. electric field) fluctuations of the vacuum modes. For an atomic emitter in an excited state, the zero-point energy can interact with the emitter and 'stimulate' it to transition to the lower energy level by emitting a photon. It follows that the spontaneous emission rate of an atom can be modified (either enhanced or inhibited) by altering its environment (i.e. altering the electromagnetic boundary conditions near the emitter). Controlling spontaneous emission in such a way can significantly influence the performance of many optoelectronic devices such as sensors [8], light-emitting devices [7], and quantum devices [2–5].

Optical cavities have long been studied for their ability to localize light (i.e. to 'trap' photons in small volumes and for long periods of time) and to accordingly modify the spontaneous emission of emitters embedded inside the cavity. The most extreme examples of such microcavity effects are provided by 3-dimensional photonic crystals, which can in principle completely inhibit the existence of propagating electromagnetic modes within engineered 'stop bands' or 'band gaps'. In this thesis, it is demonstrated that the simpler and more easily fabricated 'open access' Fabry Perot microcavity, when properly designed, can be used to implement a similar degree of control over spontaneous emission to that provided by 3-dimensional photonic crystal microcavities. The next sections will provide a brief summary of nanophotonic structures (with various types of emitters) that have been used to study and control spontaneous emission, as well as the basic principles behind the modifications induced by these structures.

1.1.1 Optical cavities for control of spontaneous emission

The modification of spontaneous emission using microcavity effects has been the subject of intensive studies for the past several decades. A wide variety of candidate optical resonators have

been studied, including photonic crystal 'defect' microcavities [2,13,15,16], 'open-access' Fabry-Perot microcavities [17–20], and plasmonic microcavities such as those based on metallic nanoparticles [21–25]. All of these systems modify the photonic environment of an emitter via changes to the local density of the available electromagnetic states (or modes). In the effort to alter/control spontaneous emission, many attempts have been carried out using different emitters inside various types of optical microcavities. However, here, we restrict the discussion to photonic-crystal-based light confinement (i.e., periodic dielectric media with 1-, 2-, or 3-dimensional periodicity) and include Fabry-Perot microcavities, which is most relevant to work described in the remainder of the thesis. Recent reviews on the control of spontaneous emission using plasmonic effects can be found elsewhere [26,27]. It is also worth noting that the interaction of resonant cavity modes with quantum emitters has been studied using a variety of 'atomic' emitters. Such emitters include isolated (i.e. typically cooled and trapped, gas-phase) atoms or ions [28–32], quantum dots (QD) [33], and light-emitting defects (i.e. so-called 'color centers') in 3-dimensional or 2-dimensional crystalline hosts such as diamond [34–37] or hexagonal boron nitride, hBN [38–41].

1.1.1.1 Photonic crystal microcavities for spontaneous emission control

As mentioned, three-dimensional (3D) photonic crystals can in principle provide a complete photonic bandgap (PBG) characterized by a total absence of electromagnetic modes (in all directions) over some finite range of frequencies. Thus, 3D photonic crystals can be used for complete control of the electromagnetic environment surrounding an emitter and accordingly for completely controlling spontaneous emission. The idea of using photonic crystals to control spontaneous emission is usually attributed to Yablonovitch [13], who introduced the concept of an artificial medium with a 3D-periodic refractive index (i.e., a photonic crystal) and invoked analogies with electronic behavior in solid crystalline materials such as semiconductors. Since that time, the enticing possibilities described by Yablonivitch have spurred countless theoretical and experimental research works. For instance, Ogawa *et al*. [42] fabricated 'stacked-stripe' layered (woodpile) 3D photonic crystals using electron beam lithography and dry etching in a III-V semiconductor system, which could also function as an efficient direct band-gap light emitter (see

Figure 1.1). Using this approach, they were able to demonstrate nearly complete inhibition of emission over frequency ranges lying within the photonic stop bands, as well as Purcell-enhanced emission into 'defect' cavity modes.
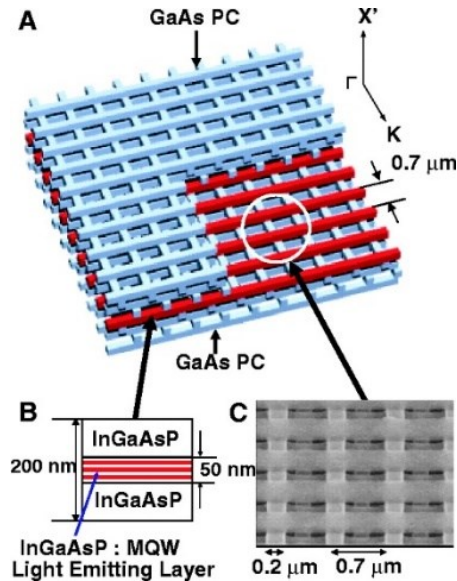
Figure 1.1. A 3D woodpile photonic crystal with embedded multiple quantum well (MQW) emitter layers [adapted from [43]].

Using a related approach in 2008, Ventura *et al.* [43] employed a direct femtosecond laser writing method to fabricate woodpile 3D photonic crystals in PbSe quantum dot (QD)-doped polymer. They exhibited fluorescence lifetime reductions for QD emission outside the bandgap, while lifetimes became higher when the QD emission band overlapped with the bandgap (see Figure 1.2). In other work, the strongly inhibited emission of semiconductor quantum dots [44] has been observed in silicon 3D inverse-woodpile photonic crystals at the telecom range. 3D inverse-woodpile photonic crystals were also formed using a CMOS-compatible method [45], in which two perpendicular sets of pores were etched (using reactive ion etching) to form the 3D photonic crystals. Subsequently, emitters were introduced in the form of PbS colloidal quantum dots suspended in toluene by immersing the crystal into a solution containing the quantum dots [44].
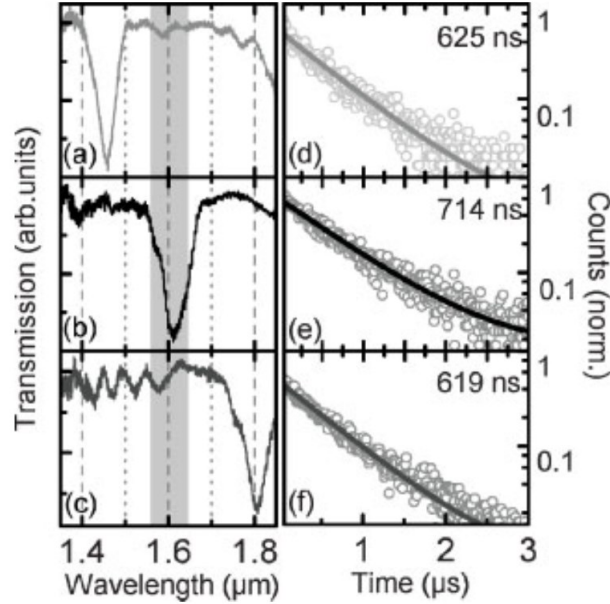
Figure 1.2. The transmission spectra of a 3D PC overlaid with the spontaneous emission spectrum of the PbSe QDs (shaded region) for [adapted from [45]], (a) cavity resonant wavelengths shorter than, (b) in line with, and (c) longer than the PbSe emission spectrum. (d)- (f) fluorescence lifetime curves corresponding to the scenarios outlined in (a)-(c) respectively.

The control of emission rate and direction has also been a priority for light sources such as threshold-less lasers, and single-photon sources (SPS). For example, the manipulation of spontaneous emission in 3D photonic bandgap structures has been exploited for achieving low-threshold lasing [46]. The authors in this study [46] used a self-assembly method to fabricate a 'colloidal' photonic crystal (i.e., a photonic crystal self-assembled through the distillation of microspheres from a solution, see Figure 1.3). They furthermore used rhodamine-B dye-doped nanospheres as an active emitter, and reported lasing in the visible wavelength range at room temperature.
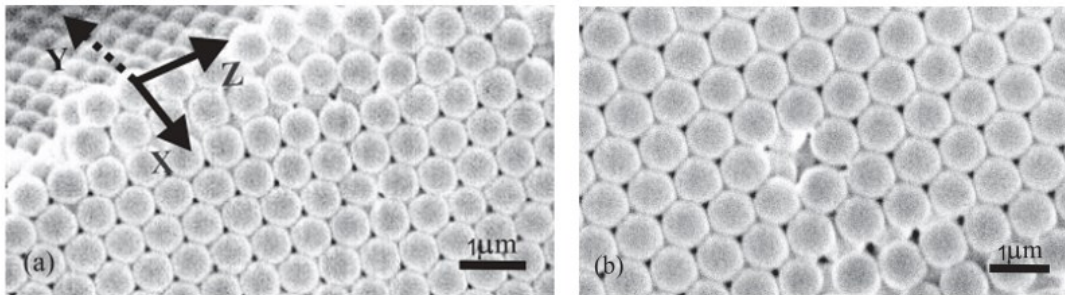
Figure 1.3. FESEM image for (a) the structure of a colloidal Photonic crystal (b) Top surface of well hexagonal ordering in the (111) plane of the fcc lattice [adapted from [47]].

Remarkable progress in the integration of emitters with 2D photonic crystals has also been reported as a means to control spontaneous emission. Compared to 3D photonic crystals, 2D photonic crystals are not as ideal for controlling spontaneous emission because the light is not strongly confined in three dimensions, such that complete photonic bandgaps spanning all directions cannot be realized. Nevertheless, significant modification of the spatial-spectral photonic mode density is still possible. Several reports over the past years have been published on modifying the spontaneous emission of emitters using 2D photonic crystals, such as enhanced spontaneous emission from the coupling of PbSe quantum dots to silicon 2D photonic crystal microcavities [47]. In that work, the investigators used a PbSe nanocrystal solution to deposit quantum dots in a central hole (i.e., defect) in a 2D silicon photonic crystal (Figure 1.4). A Purcell factor and spontaneous emission coupling factor of ~ 35, and ~ 0.04, respectively, were estimated.
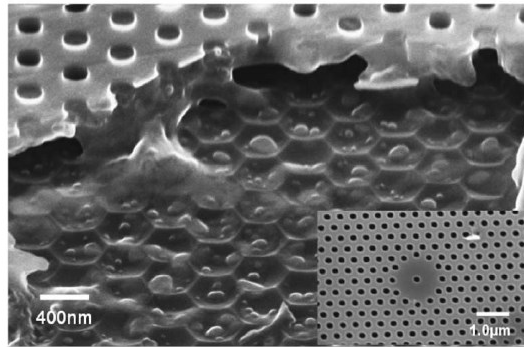
Figure 1.4. SEM image of cleaved 2D silicon photonic crystals, showing PbSe quantum dots stuck in the air holes [taken from [49]].

In similar work, Makarova *et al*. [48] coupled erbium-doped silicon-rich silicon nitride nanocrystals to a 2D photonic crystal. The study showed the *Q*-factor of the PC resonance decreased by increasing the pump power, this observed decrease indicates a change in the refractive index of the cavity when the sample is heated (see Figure 1.5). A Purcell factor of 1.4 was predicted from the observed 20-fold enhancement of the emission of Erbium coupled to the PC cavity at high pump power, while a 44-fold enhancement was observed at low pump power.
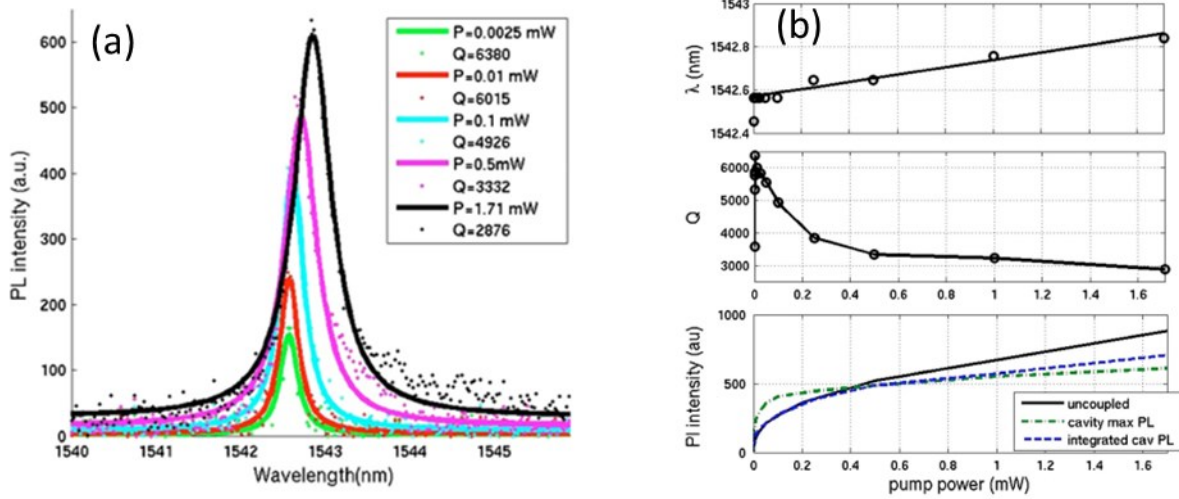
Figure 1.5. (a) Plot of the PL intensity shows a redshift due to high pump power, thus leading to a reduction in the resonance Q of the cavity. (b) Effect of increasing pumping power on the cavity resonant wavelength, *Q*-factor, and PL intensity [adapted from [50]]

Using the same fabrication method as above, Yiyang Gong *et al.* [49] also achieved a high Q-factor and small mode volume cavity, which narrowed the emission linewidth. Their experiment was performed at different temperatures to estimate the varying Purcell enhancement. At cryogenic temperatures, they observed Purcell enhancement of 11-to 17-fold; however, at room temperature, they found only 2.4-fold enhancement. Another study by Y. Wang *et al.* [50], fabricated 2D slab non-airbridge and airbridge heterostructure photonic crystals microcavities coupled to Er-doped silicon. For their fabricated airbridge structures, they observed high *Q*-factor and photoluminescence enhancement at 1.5 μm. The study demonstrated a PL enhancement of 3 in the airbridge cavity (higher than the non-airbridge cavity) at room temperature.

Of greatest relevance to the work described here, one-dimensional (1D), omnidirectional Bragg reflectors have also been studied for their potential to modify the spontaneous emission rate of emitters. It is now well-known that Bragg reflectors with sufficiently high refractive index contrast can exhibit an 'omnidirectional' reflection band for light incident from a lower index medium; i.e., high reflection over a finite wavelength range for plane waves of any incident angle and polarization state. However, these structures always support in-plane guided modes at frequencies inside the omnidirectional band, and thus are not able to completely prohibit the existence of optical modes in the way that 3-D phtonic crystals can. Nevertheless, it has been

8

shown that a 1D ODR enables the inhibition of spontaneous emission for an emitter located in the low index layer at a sufficient distance from the mirror to reduce coupling to the guided modes [51].

Moreover, Yariv *et al.* [52,53] proposed and fabricated a new class of 1D omnidirectional-spherical Bragg resonator called 'onion' cavities. The SEM image (see Figure 1.6) shows the onion resonator with a spherical air-core surrounding Si/SiO_2 cladding. They studied both the enhanced spontaneous emission into cavity modes and the suppression of spontaneous emission into background radiation modes. Their study showed that the air core is essentially isolated from free space due to the omnidirectional Bragg cladding. However, this structure is not trivial to fabricate, and it is also difficult to efficiently couple external beams to the cavity modes. Nevertheless, this work is conceptually similar to our proposal to control spontaneous emission using omnidirectional-mirror cladded buckled-dome cavities, detailed in Chapter 3.
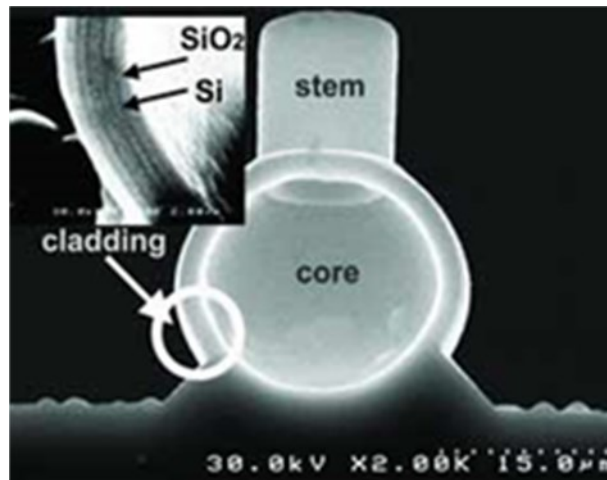
Figure 1.6. SEM image of Bragg 'onion' resonator. The inset shows the Si/SiO_2 cladding pairs. [adapted from [55]].

1.1.1.2 'Open-access' Fabry-Perot microcavities for spontaneous emission control

So-called 'open-access' Fabry-Perot microcavities (such as shown in Figure 1.7) have attracted significant attention over the past decade. These cavities confine light between a pair of micro-structured mirrors, at least one of which is curved to enable 3D mode confinement. In principle, open-access Fabry-Perot cavities enable an arbitrary emitter to be located in the high-field region

(i.e., the open space) between the mirrors, and they also allow for straight forward tuning through control of the mirror spacing. These are significant advantages compared to many other types of microcavities such as 3D photonic crystals where tuning of the cavity resonant wavelength must typically rely on thermo-optic or non-linear optic effects.
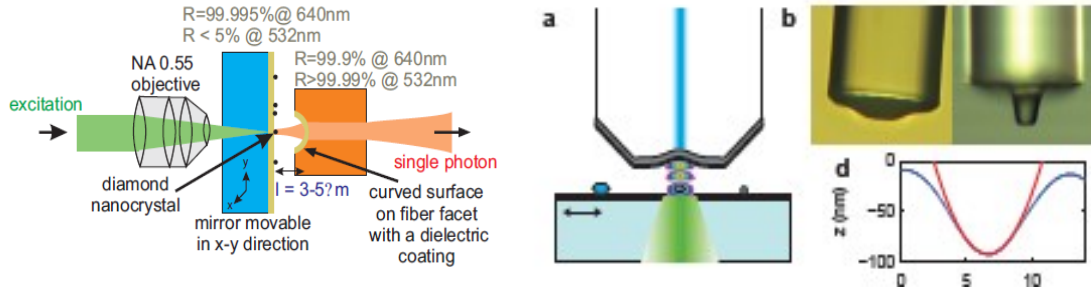
Figure 1.7. Schematic representations of some fiber-based curved-mirror microcavities reported in the literature [adapted from [52], [53]].

Much recent work has focused on reducing the size of such cavities, which were traditionally fabricated using mechanically polished macroscopic curved mirrors. The goal is essentially to realize cavities with small mirror spacing and small mirror radius of curvature, which, as detailed below, corresponds to both a small mode -waist and -volume. This has motivated researchers to explore various micro-machining techniques such as CO_2 laser ablation [54], focused ion beam (FIB) milling [55], and dry etching [56] to form ultra-small and atomically smooth curved surfaces as substrates for high reflectance dielectric mirrors. A typical approach to the construction of such cavities is to form a micro-scale curved mirror on either a substrate or a fiber end facet, and to carefully align (typically using piezo positioners) this curved mirror with a second mirror deposited on a flat substrate (as shown in Figure 1.7). This type of hybrid construction is complex and is difficult to scale to a large number of cavities, but on the other hand does allow great flexibility in terms of introducing and aligning atomic emitters inside the cavity.

A few historical examples of such hybrid-assembled micro-scale curved-mirror cavities follow. In 2005, Trupke *et al.* [57] used wet etching to produce ultra-smooth concave surfaces in glass, suitable for the subsequent deposition of curved mirrors. Later, Biedermann *et al.* [56] showed that high finesse $\mathcal{F}$ ($\sim 64,000$) cavities could be realized using mirrors deposited on curved surfaces formed by dry etching (see Figure 1.8 (a)). In 2010, Muller et al. [58] reported high-finesse low-mode-volume cavities, in which smooth concave spherical surfaces on the end facets

10 of 143

10

of optical fibers were formed by CO2 laser ablation (see Figure 1.8 (b)). Forming the curved mirror surface on the face of an optical fiber has proven very popular, and Muller has been followed by numerous research groups over the past decade. Dolan *et al.* [55] introduced a focused ion beam (FIB) milling process to produce arrays of concave surfaces suitable for high-finesse mirrors (see Figure 1.8 (c)). By aligning these curved mirrors with a second (flat) mirror substrate, they have achieved small mode volumes and Q-factors exceeding 10,000.

(a)   (b)

(c)
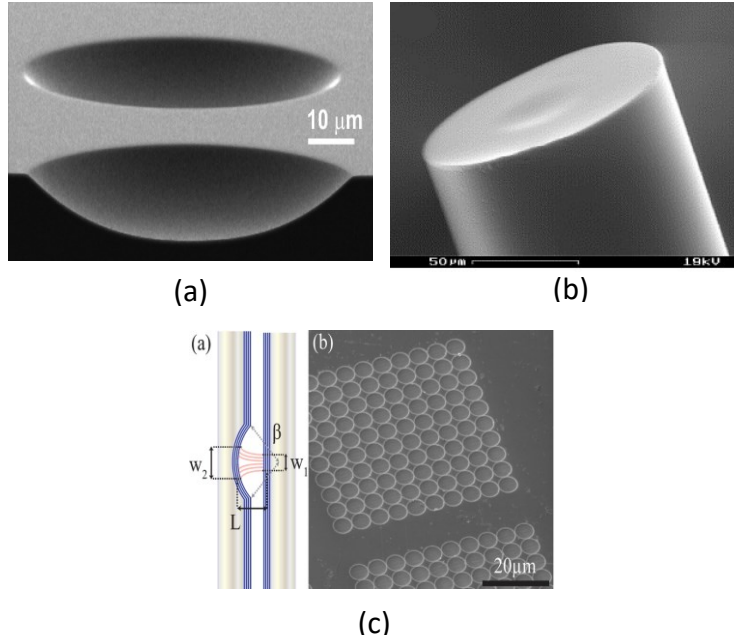
Figure 1.8. Microscope images showing: (a) Two ultra-smooth micromirrors fabricated using dry etching [adapted from [56]]; (b) laser machined fiber end face [adapted from [58]]; (c) Concave features milled into silica using FIB [adapted from [55]].

Many groups have already applied such micro-scale, open-access Fabry-Perot cavities to studies of cavity quantum electrodynamics (CQED), a topic which is described in greater detail below. For example, in 2013, Hanno *et al.* [59] fabricated an open-access cavity consisting of one planar dielectric mirror, onto which fluorescent nanodiamonds (NDs) were deposited, and a second curved mirror fabricated by laser machining on the end facet of an optical fiber. A cavity finesse of $\mathcal{F}=20000$ was achieved, and the study illustrated some powerful features of such a hybrid-assembled, fiber-based open cavity for use in CQED. First, the cavity can easily be aligned to a previously identified emitter of interest by using micro-positioners. Second, piezo-positioners can be used to adjust the mirror spacing, so that the cavity resonance can be readily tuned relative to

the emission line of interest. Third, both pump (excitation) light and the emitted (fluorescent) light can be efficiently coupled into the optical fiber (with appropriate design of the cavity properties), greatly simplifying the experimental setup. These attributes provided the researchers with unprecedented flexibility for studying Purcell effects. For example, the scaling of the fluorescence emission lifetime (for light-emitting NV-vacancy centers in nanodiamonds) was studied as a function of spectral alignment between the cavity resonance and the emitter (i.e., both on- and off-resonance conditions). Similar studies have been reported using semiconductor QDs embedded inside the flat mirror substrate of such 'open-access' cavities (see Figure 1.9 (b), [60]). In another related work, Gallego *et al.* [61] observed a high Purcell enhancement by trapping a Rb atom inside an open-access fiber-based cavity.

(a)   (b)
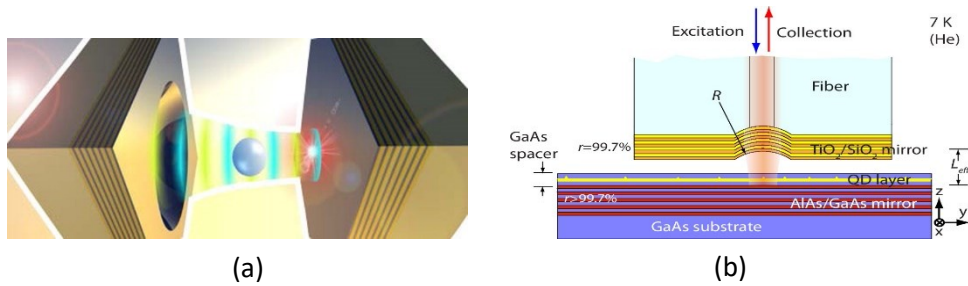
Figure 1.9. (a) Nanoparticles trapped inside open cavity [adapted from [63]]; (b) Schematic of coupling quantum dots to external-mirror [adapted from [60]].

These studies illustrate significant advantages of fiber-based, hybrid-assembled open-access Fabry-Perot cavities, particularly for theoretical studies of Purcell effects and CQED. However, the serial processing techniques used for curved mirror fabrication, and the hybrid assembly of the cavity, present challenges with respect to scaling up to large numbers of cavities. For many applications of CQED, it is envisioned that large numbers of emitter-cavity systems will be needed, and monolithic approaches for implementing emitter-embedded cavity arrays on a single chip are sought [62].

1.2 Pressure sensing

Microelectromechanical systems (MEMS) pressure sensors have received a great deal of attention in recent years. This is due to their light weight, small volume, high performance, and low cost.

Such pressure sensors are required for many applications in the biomedical field, as well as in the automobile, aerospace, and industrial sectors. As there are many different principles used for the function of a pressure sensor, such sensors are typically classified as piezoresistive, capacitive, piezoelectric, optically resonant, and fiber optic interferometric sensor types [63].

Amongst these different types of pressure sensors, optical pressure sensors have many advantages, including an immunity to electromagnetic interference (EMI), small size, high accuracy and resolution, and the capability to work in harsh environments. Many different architectures for fiber optic sensors exist, such as microstructural sensors [64] diaphragm-based sensors [65], Mach-Zehnder interferometer sensors [66], and Fabry-Perot (FP) interferometer sensors [67–69]. In the next section, a brief review of some recent research on Fabry-Perot (FP) interferometer sensors is presented.

1.2.1 Fabry-Perot interferometer sensors

Recently, Fabry-Perot interferometer (FPI) sensors have attracted significant research interest, due to their simplicity of operation, robust nature, and immunity to EMI. FPIs are similar to optical microcavities in that they are based on the prototypical Fabry-Perot resonator (i.e., two parallel reflecting surfaces separated by a certain distance). The FPI sensors can be classified into two simple configurations, extrinsic Fabry-Perot interferometer [70,71] and intrinsic Fabry-Perot interferometer [72,73] depending on the fabrication method of the reflectors. Figure 1.10 shows the typical structure of the FPI sensor. Diaphragm-based extrinsic Fabry-Perot interferometers have been the most commonly studied in the pressure-sensing literature due to their high sensitivity, high resolution, and typically low-cost fabrication. The sensitivity of such an extrinsic cavity depends on the material and thickness of the diaphragm. A variety of different materials have been used to fabricate the diaphragm, including SiN, polymer, and silica.
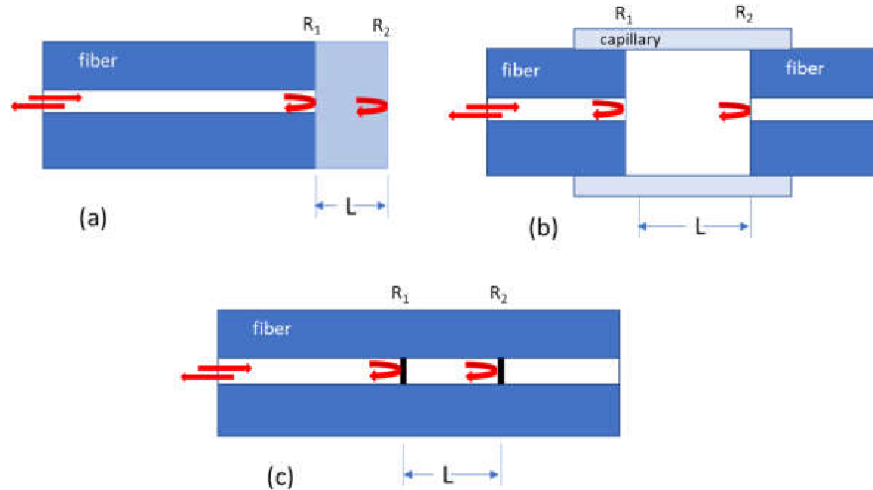
Figure 1.10. Two configurations of FPI [adapted from [75]], (a) Extrinsic FPI where the membrane is deposited on the top of the fiber. The interfaces between the membrane/fiber and membrane/environment forms a weak cavity that is used for sensing. (b) Extrinsic FPI where the cavity is composed of two fibers, and each fiber face forms the cavity reflectors. (c) A second intrinsic FPI, where the cavity reflectors are produced by inducing a refractive index change along the length of the fiber.

In 2001, Don C. Abeysinghe *et al.* [74] developed a novel MEMS pressure sensor for the measurement of pressure at temperatures up to 600 °C using a silicon diaphragm, which was fabricated on the end face of an optical fiber. This sensor operated at lower pressure (0 to 80 psi) with a sensitivity of about 0.11 mV/psi. Other techniques have been proposed to improve the fabrication of the diaphragm material, such as by Li *et al.* [75] who used simple micromachining techniques to fabricate a miniature optical Fabry Perot interferometric pressure sensor with a highly linear response in the range from 0.2-1 MPa and a sensitivity of 10.07nm/MPa. An EFPI pressure sensor based on an nm-range thick silver diaphragm was demonstrated, and showed a much higher sensitivity of 70.5 nm/kPa [65]. Li. Jiang *et al.* [76] reported a single-crystal silicon carbide SiC diaphragm-based extrinsic Fabry-Perot interferometer (EFPI) pressure sensor which showed good linearity in the range from 0.1-0.9 MPa, with a resolution of 0.27 % of full scale (F.S.) at room temperature. An alternative sensor design was proposed by Daniel *et al.* [77], where they utilized metal-embedded optical fiber as a Fabry-Perot optical pressure sensor for high-frequency dynamic pressure measurements which could potentially be used in harsh environments.

Moreover, various attempts to miniaturize EFPI sensors for high temperature operation were developed. For example, Pevec and Donlagic [78] presented a miniature FP fiber optic sensor to

simultaneously detect pressure and temperature, with a demonstrated sensitivity of 36nm/bar. Weiyi Ma *et al.* [79] presented an all-fiber extrinsic Fabry-Perot interferometer (EFPI) pressure sensor with a diameter of only 125 µm measured under high temperatures up to 800 °C. Pure silica was used as the diaphragm, and a femtosecond laser was used to reduce the thickness of the diaphragm and increase sensitivity. The reported sensitivity of this sensor was 70.8 nm/MPa. Recently, a very high finesse, Fabry-Perot interferometric MEMS pressure sensor was reported [80], with a high sensitivity of 1.598 µm/MPa at room temperature, with 0.002% of full scale (F.S.) resolution over a pressure range of 1MPa.

1.3 Monolithic Fabry-Perot microcavities

Over the past several years, our research group has developed a new 'buckling self-assembly' technique [1,81] for manufacturing arrays of air-core, half-symmetric microcavities on a chip (see Figure 1.11). The fabrication method is monolithic and integrated, allowing thousands of highly symmetric high finesse cavities ($\mathcal{F} \sim 3500$ [82]) to be produced on a single wafer.
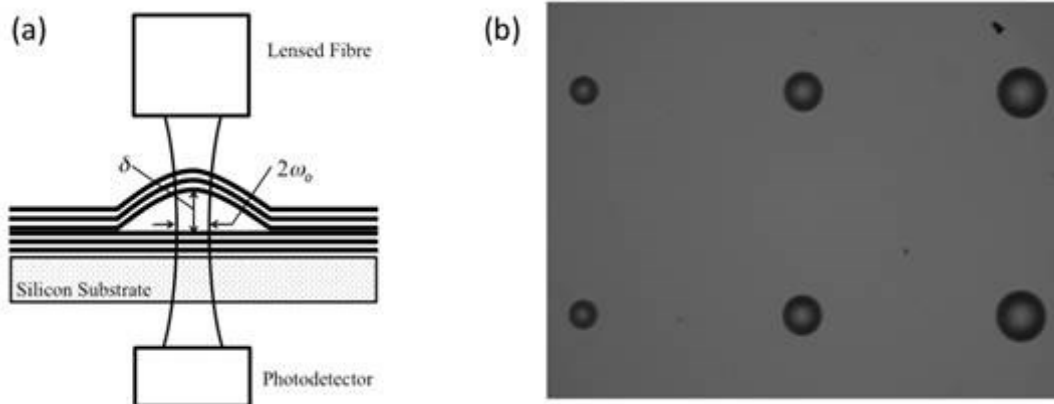
Figure 1.11. Buckled dome microcavities: (a) Schematic showing a cross-sectional profile of a typical dome (not to scale), and the experimental arrangement used to study the optical properties; (b) microscope image of different sizes of domes [adapted from [1]].

These microcavities could find important applications in the study of CQED systems and for use in proposed quantum networks which would employ large arrays of emitter-cavity nodes. Through lithographic patterning, different sizes and shapes of these microcavities can be fabricated on a single chip. Of most interest here, a circular lithographic feature results in the formation of a half-symmetric curved-mirror Fabry-Perot cavity (as in Figure 1.11). In previous work, moderately

high finesse and Q factors of $\sim 3\text{x}10^3$ and $\sim 4\text{x}10^4$, respectively, have been demonstrated in both the 1550 nm and 780 nm wavelength ranges targeting the emission wavelengths of Er and Rb emitters [1]. However, these buckled cavities are inherently closed structures, with an inner air core isolated from the external environment. A first attempt to fabricate open access versions of these cavities, by FIB milling of access holes in the upper curved mirror was reported by C.A. Potts *et al*. [82]. That work described an array of SiO_2/Ta_2O_5 based cavities with $\mathcal{F} \sim 3500$ and mode volume $\sim 35\lambda^3$, but also showed that the optical properties were detrimentally affected by contaminations introduced during the milling process. The serial nature of the focused ion beam (FIB) technique represents another drawback, implying that long and tedious processing may be needed to make holes in multiple cavities.

Another approach for creating open access buckled microcavities was demonstrated by M. Bitarafan *et al.* where in addition to demonstrating high-density arrays of buckled cavities operating in a fundamental (longitudinal) mode regime, with $Q > 10^3$ and mode volume as small as $a \sim 1.3\lambda^3$ at 1550 nm [83], they also described the fabrication of dome cavities intersected by air-core channels (see Figure 1.12 (a)). The straight-sided channels might function as waveguides for pump or trapping laser beams, or as microfluidic channels for introducing an emitter or analyte. Importantly, these channel-connected dome microcavities were shown to retain excellent optical properties.

<div align="center">(a)   (b)</div>
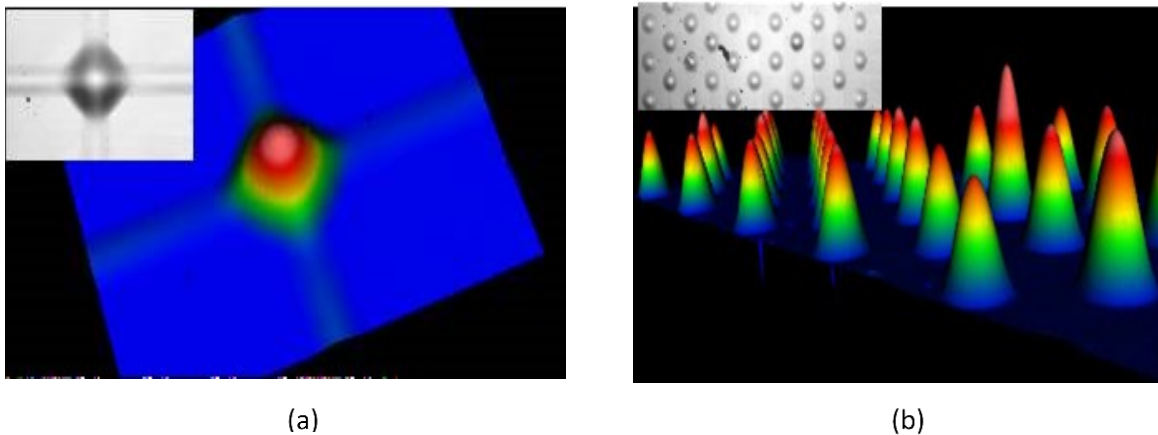
Figure 1.12. (a) Surface profile plot (Zygo optical profilometer) showing a channel-connected dome. The inset shows a microscope image for a similar device [adapted from [83]]; (b) Surface profile plot for an array of domes with a base diameter of 50μm. The inset shows a microscope image for a similar array [adapted from [83]].

More recently, J. Maldaner *et al.* [84] reported a monolithic process to fabricate open access cavities (see Figure 1.13), by using a wafer-scale reactive ion etching process to etch photolithographically aligned holes into buckled domes. The etched cavities retained excellent optical properties, essentially unaffected by the additional steps needed to introduce access holes through the top mirror.
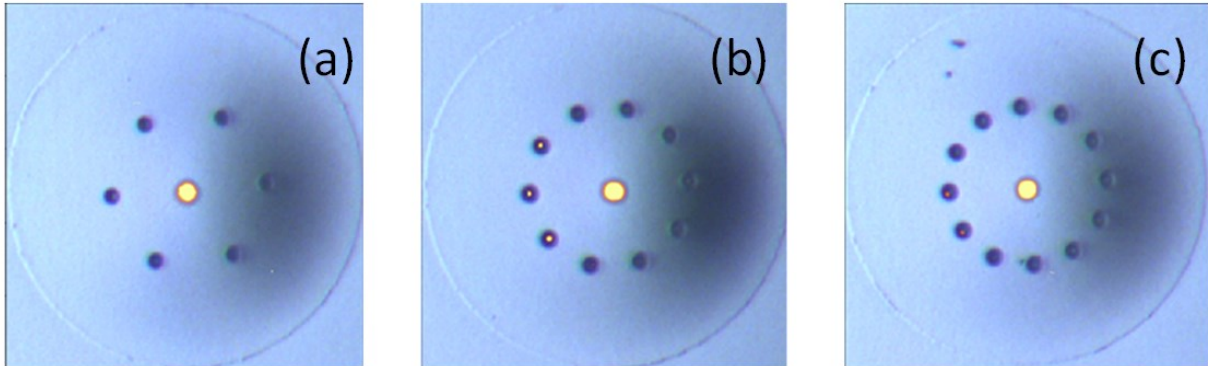
Figure 1.13. (a-c) Optical microscope images of domes with variable numbers of etching holes [adapted from [84]].

These cavities were used to study the infiltration of liquids inside the microcavities, and to study how the liquid modified the modes of the cavities (as seen in Figure 1.14). Such liquid infiltration provides an opportunity to incorporate 'atomic' emitters in solution into these microcavity arrays, and this was one target goal of this thesis. For example, PbS quantum dots could be drop cast on the top of the cavity, such that some of the QDs would infiltrate the cavity. Any QD that successfully infiltrated the cavity would be trapped inside the cavity and act as an active medium. Such a method could be used to produce a single-photon source or an on-chip laser.
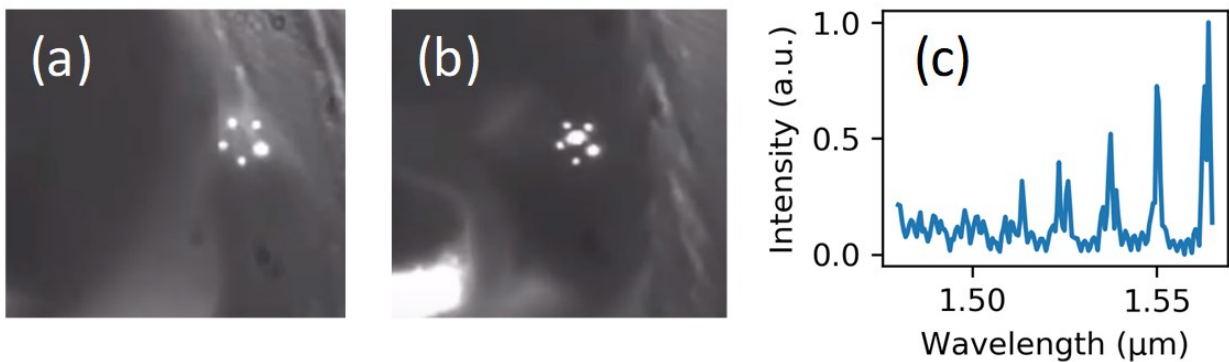
Figure 1.14. (a), (b) Images captured before/after dispensing IPA. A cavity mode is only visible after IPA has successfully infiltrated the cavity. c) Measured cavity resonances [adapted from [84]].

1.4 **Dissertation outline**

The thesis is organized as follows:

The introductory Chapter 1 provided a brief background and literature review about the modification of spontaneous emission in dielectric microcavities (in particular 'open-access' microcavities), thereby motivating this dissertation project. Diaphragm-based optical pressure sensors were also briefly reviewed, as a precursor to pressure-sensitivity studies described later in the thesis.

Chapter 2 outlines some of the theoretical background related to the main thesis topics. First, the basics of the planar Fabry-Perot cavity and quality factor are introduced. Next, relevant parameters of the spherical mirror Fabry-Perot cavity such as Gaussian beam modes, resonance frequencies, and mode volume are overviewed. Finally, laser rate equations used in spontaneous and stimulated emission, and related figures of merit, including cooperativity (C) and Purcell factor (F_p) are discussed.

Chapter 3 was published as "Cooperativity enhancement in buckled-dome microcavities with omnidirectional claddings" [85], and explains the theoretical model used to calculate the emission rate of a dipole emitter embedded inside buckled-dome microcavities relative to the free-space emission rate. This theoretical study presents small mode volume Fabry-Perot cavities based on a-Si/SiO$_2$ mirrors similar to those fabricated in Ref. [83]. A 3D finite-difference time-domain (FDTD) simulation (Lumerical) was used to predict the cooperativity and Purcell factor of these cavities. The top mirror (curved) of the buckled-dome cavity was described by using the Bessel function shape predicted by elastic buckling theory [86].

In Chapter 4, the fabrication process of the buckled cavities is described, including two attempts to embed erbium-doped films as emitting layers into this process. A detailed description of the optical setup developed to perform microscope-based PL experiments is also provided, along with some preliminary PL results.

Chapter 5 describes a theoretical and experimental study of the effects of changes in ambient pressure on the resonance frequencies and other optical properties of the buckled-dome cavities. We showed that these cavities exhibit linear pressure response over ranges that can be customized by choice of cavity size, as well as high vibrational mechanical resonance frequencies, and that

they might be of interest for sensing of dynamic pressure signals such as in photo-acoustic or ultrasound applications.

Finally, the thesis work, research contributions, and possibilities for future studies are summarized and presented in Chapter 6

Chapter 2

Theoretical Background

This section provides background information concerning Bragg reflectors, conditions for omnidirectional reflectance by Bragg reflectors, planar and curved mirror FPCs, and optical modes in spherical mirror resonators. These are requisite topics for understanding the material in chapters 3, 4, and 5.

2.1 Distributed Bragg reflectors

Dielectric mirrors, also known as distributed Bragg reflectors, are composed of alternating materials with different refractive indices. A special and important case is commonly called a quarter-wave stack (QWS). The quarter-wave-stack condition can be expressed as:

$$\lambda_B = 4n_L d_L = 4n_H d_H \quad , \tag{2.1}$$

where λ_B is the Bragg wavelength, and d_H/n_H and d_L/n_L are the thicknesses/refractive indices of the higher and lower index layers, respectively. It can be shown that the QWS provides the highest reflection and widest stop band for a given pair of materials and the number of periods in the Bragg reflector. Figure 2.1 shows an example of a Bragg reflector, with a high index layer next to an air incident medium and the incident light partially reflected at each boundary. At and near the Bragg wavelength (i.e., in a so-called 'stop-band'), strong reflection occurs due to constructive interference of the sub-reflections of light at each interface in the stack.
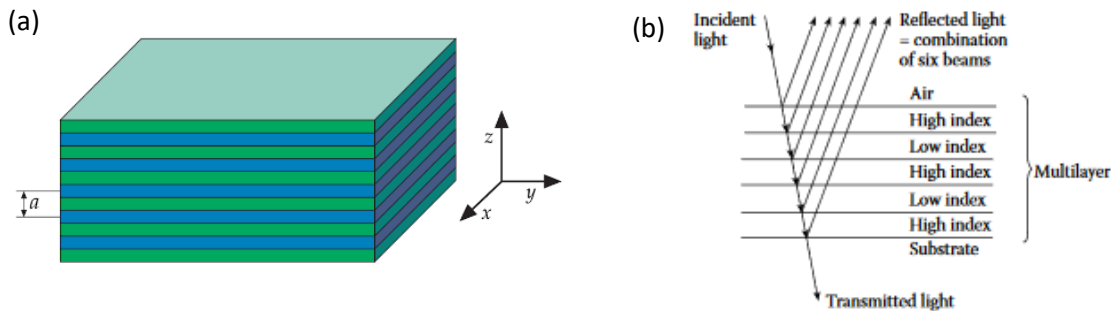
Figure 2.1. (a) Schematic illustration of a 1D photonic crystal (i.e., a Bragg reflector) comprising alternating layers of high and low refractive indices, with periodicity an along the z-axis [adapted from [15]]; (b) Schematic showing the partial reflection of light at each interface [adapted from [87]].

At normal incidence, the maximum reflectance of an N-period QWS is given by [87]

$$R_{Bragg} = \left[\frac{1-(n_s/n_0)(n_L/n_H)^{2N}}{1+(n_s/n_0)(n_L/n_H)^{2N}}\right]^2 . \qquad (2.2)$$

The QWS mirror exhibits high reflectance for a range of wavelengths. The width of the fundamental stop-band (centred at the Bragg wavelength defined above) at normal incidence can be expressed [87]:

$$\Delta\lambda_{Bragg} = \lambda_{Bragg}\frac{4}{\pi}\arcsin\left[\frac{|n_H-n_L|}{n_H+n_L}\right] . \qquad (2.3)$$

The stopband width is thus highly dependent on the index contrast of the two materials.

2.2 Omnidirectional reflectance

Metallic mirrors reflect strongly for all polarization states and incident angles. However, they have relatively high absorption losses, which limits their maximum reflectance and also their potential transmittance, and thus presents obstacles for some applications such as CQED that require ultra-low-loss mirrors. Dielectric mirrors, compared to metallic mirrors, can be relatively non-absorbing through a choice of suitable transparent materials in a given wavelength range of interest. Conventional dielectric (e.g., QWS) mirrors reflect light over a limited spectral bandwidth and over a limited range of angles of incidence, and are often restricted to a particular state of polarization (in the case of off-normal incidence).

However, it has been recognized since the late 1990s [88] that a one-dimensional photonic crystal (i.e. a Bragg mirror) can provide omnidirectional reflection (high reflection for all incidence angles and states of polarization, over some finite spectral range) if certain conditions are met. Specifically, omnidirectional reflection requires that the following two criteria are satisfied. First, the index contrast between the two constituent materials must be sufficiently high, and second, the refractive index of the incident medium must be sufficiently less than the refractive index of the lower index material comprising the mirror layers. Figure 2.2 illustrates the ω-k diagram, for instance, corresponding to a 1-D (infinite) periodic medium with $n_1 = 1.7$ and $n_2 = 3.5$. The bold solid lines are the 'light lines' in an external air incident medium. Free-propagating modes (i.e.,

radiation or plane-wave modes) in air lie above this light line. On this diagram, the greyed regions represent the combinations of ω and k for which light can propagate 'freely' through the periodic medium, while the white regions represent combinations that are subject to constructive back-scattering (see Figure 2.1 above) and are thus 'prohibited' inside the periodic medium. In other words, the grey regions represent 'passbands' and the white regions are 'stopbands'. All propagating modes in the external air region lie between the vertical axis of the plot (i.e., normal incidence on the periodic medium interfaces) and the light line in air (i.e., grazing incidence). Thus, if the medium has a stopband that spans some finite range of frequencies for both TE and TM polarizations and for all angles from normal to grazing incidence, this corresponds to a so-called 'omnidirectional' reflection band. As shown by the labels in Figure 2.2, the QWS considered here does present such an omnidirectional band for incidence from an external air medium.

As is well known, for TM polarization there is a specific angle of incidence, known as the Brewster angle ($\theta_B = \tan^{-1}\left(\frac{n_H}{n_L}\right)$), at which the sub-reflections depicted in Figure 2.1(b) are precisely zero. At this angle, depicted by the dotted line in Figure 2.2, there is therefore a 'closing' of the stop band. As Fink *et al.* [89] showed, a key pre-requisite for omnidirectional reflectance is thus that the Brewster angle (inside the Bragg stack) is not 'accessible' for plane waves incident from the external medium. In practice, this implies that a suitable choice for n_L is needed. Specifically, the ratio of this index to the incident-medium index ($n \sim 1$ for air) must exceed some minimum threshold, which can be calculated using Snell's law and the Brewster angle expression above. The second pre-requisite for omnidirectional reflection is simply that the index contrast (n_H/n_L) is sufficiently high, so that the stopband width is large enough to ensure that some range of frequencies remains inside the stop band for all angles of incidence. While analytical expressions are not available for this criterion, numerical calculations show, for example, that for air incidence and $n_L \sim 1.5$, n_H must exceed ~ 2.2 in order for an omnidirectional band to exist.
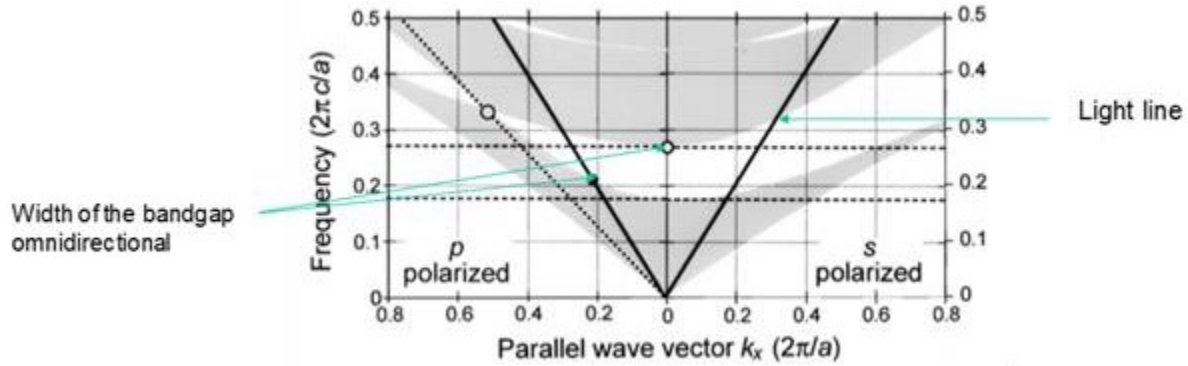
Figure 2.2. Predicted band structure for an infinite 1D-periodic medium (i.e. a Bragg reflector) with $n_1 = 1.7$ and $n_2 = 3.4$ [adapted from [88]]. The bold lines indicate the light lines in an external air medium. The dotted line indicates the Brewster angle inside the periodic medium.

Finite Bragg reflectors exhibit the features depicted in Figure 2.2, but of course with sub-unity reflectance and passband ripple due to finite medium effects. As an example, Figure 2.3 shows the predicted reflectance for a 4-period Bragg mirror with a normal-incidence Bragg wavelength of $\lambda_B = 1550$ nm and based on a-Si ($n \sim 3.7$) and SiO$_2$ ($n \sim 1.47$), as calculated using a transfer matrix technique. Similar mirrors are employed in our buckled dome microcavities; as shown, they have sufficient index contrast to provide a wide omnidirectional reflection band for incidence from air. As depicted by the series of plots, as the incident angle is increased the stop-bands shift towards higher frequencies (shorter wavelengths), consistent with Figure 2.2. Also, for the increasing angle of incidence, the stop-band for TE becomes wider while the stop-band for TM becomes narrower. Nevertheless, because these mirrors handily satisfy the conditions mentioned above, a wide omnidirectional 'stop' band (i.e., band of high reflectance for both polarization states) spans the wavelength range from ~1300 to 1700 nm.

It is important to mention that a 1D periodic medium, even with 'omnidirectional' reflection properties, differs significantly from a 3D photonic crystal, which can possess a truly omnidirectional bandgap. The reason is that 1D periodic media can typically support in-plane guided modes at all frequencies. A typical example is shown in Figure 2.4, for a 5-period Bragg reflector. This Bragg reflector can also be viewed as a 5-core coupled waveguide system, in which each high index layer of the Bragg stack is the core of a slab waveguide. In-plane guided modes are confined by total internal reflection inside these high-index layers. They lie beneath the light line of the low-index Bragg layers, and thus of course beneath the light line of the air incident

23

medium (i.e. in the grey regions beneath the light line in Figure 2.2). Nevertheless, energy from an external source, even with frequencies within an omnidirectional band of the type discussed above, can couple into these guided modes if the source is sufficiently close to the interface such that it interacts with the evanescent fields of the guided modes. This coupling has important implications on the spontaneous emission rate and spatial profile of dipole emitters placed near to the surface of a Bragg mirror, as discussed in Chapter 3.

For the 5-period waveguide system, each mode of the isolated individual waveguide cores splits into 5 'supermodes' of the coupled system, as shown in Figure 2.4 (a). Also, for the asymmetric structure shown (i.e. with air on one side and a substrate on the other), one of the 5 coupled modes is essentially a surface wave. This surface mode will exist when the separation between the adjacent waveguides satisfies certain criteria [90] and, roughly speaking, the energy of the surface mode is confined to the surface by total internal reflection at the air interface and by coherent Bragg scattering (see Figure 2.4(b)) on the other side.
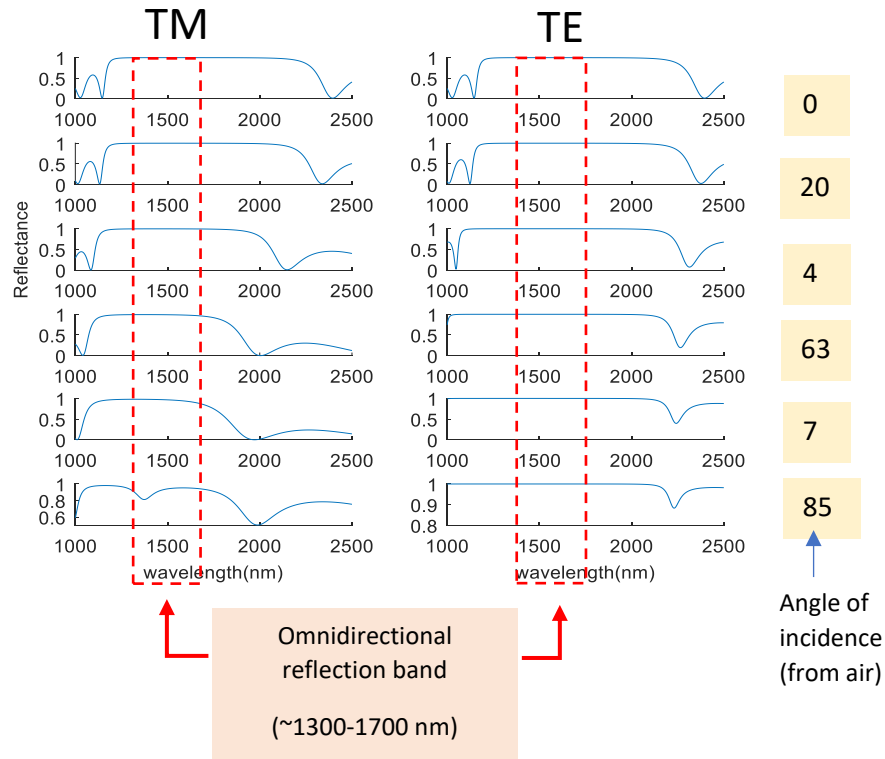
Figure 2.3. Transfer-matrix calculations of reflectance for 4-period a-Si/SiO$_2$ mirror as described in the main text. An omnidirectional band of high reflectance (for both TE and TM polarizations) is indicated in the ~ 1300-1700 nm wavelength range.

a

b
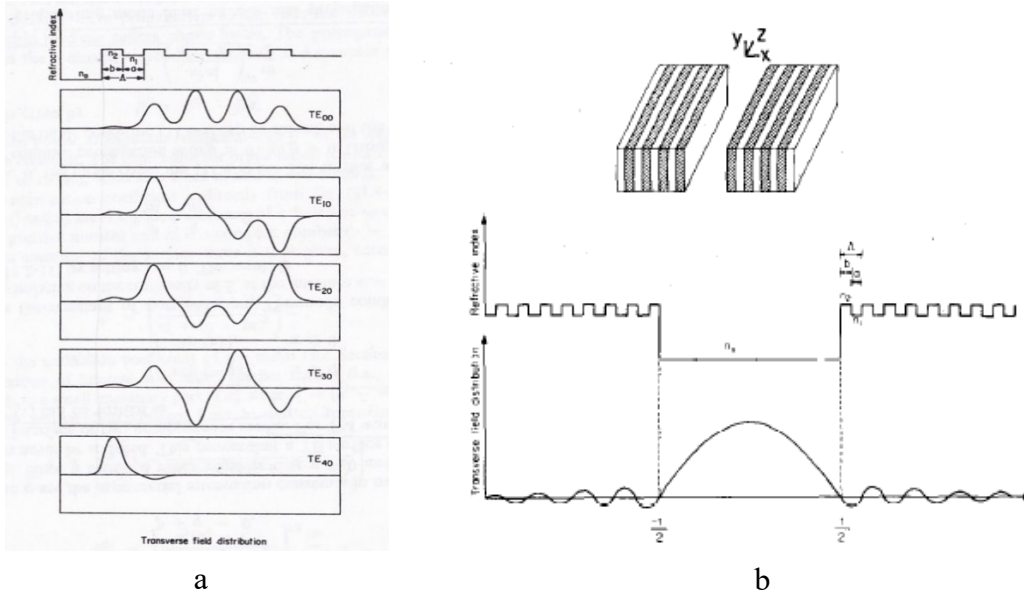
Figure 2.4. (a) Field profiles for a five-channel waveguide with indices n_1=2.89, n_2=3.38, n_a=1, a=b=0.5λ [adapted from [90]]; (b) Field distribution of the fundamental mode of a Bragg reflection waveguide with n_a= 1.0, n_2 =3.38, n_l=2.89, λ=1.15µm, a=b=0.5 Λ =0.1µ, t=153µm[adapted from [91]]. .

2.3 Optical cavities

In simple terms, an optical cavity traps and confines light at specific (resonant) frequencies. Optical cavities play a vital role in numerous fields, such as in optical sensor applications, optical filters, lasers, and other cavity-enhanced light sources such as resonant-cavity LEDs. Recently, an emerging application of the optical cavity is found in the field of cavity quantum electrodynamics (CQED), which encompasses interactions between photons and atoms confined inside an optical cavity. Optical resonators of many different types are studied in the literature, including planar and curved-mirror Fabry-Perot cavities, waveguide-based ring resonators, and defect-cavities in 2-D and 3-D photonic crystals [92]. Here, we focus only on the planar and spherical FPCs, which are the basis of the work described in subsequent sections.

2.3.1 The planar mirror Fabry-Perot resonator

The planar Fabry Perot resonator is the most basic form of the optical cavity, and arguably the most important kind of optical resonator. It consists of two planar mirrors separated by a distance *L*, between which a light beam can 'bounce' (back and forth), as depicted in Figure 2.5 (a). If the

mirrors are assumed to have an infinite extent, the modes of the planar cavity are expressed in terms of idealized monochromatic (single frequency) plane waves (A, B), as shown in Figure 2.5(a).
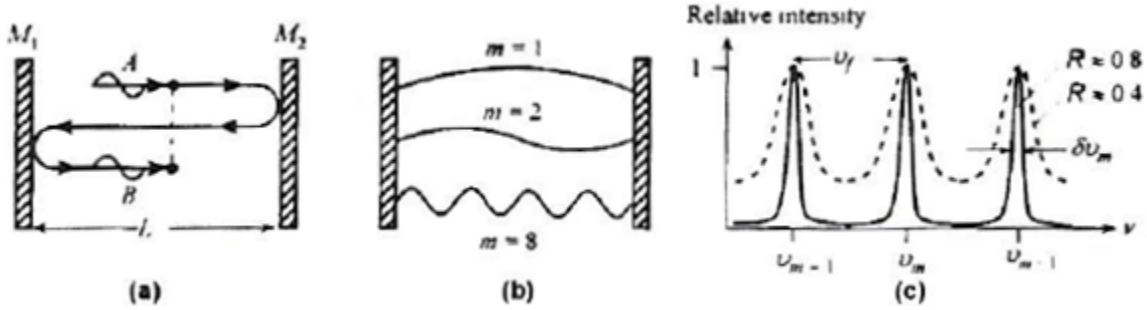
Figure 2.5. Schematic of the Fabry-Perot cavity which [adapted from [93]].

For simplicity, consider the case of normal incidence on the planar mirror, thus plane waves travelling along the axis of the cavity. An infinite set of sub-reflected wave components can be envisioned inside the cavity, and they are subject to interference with each other. Cavity modes correspond to frequencies at which this infinite set of sub-reflected waves achieve constructive interference. For a hard-mirror boundary condition (i.e., neglecting field penetration into the mirrors), the resonant mode condition is that the 'bouncing' plane wave plane, when it travels one round trip, must experience a phase shift (2ϕ) equal to an integer multiple of 2π :

$$2\phi = n\left(\frac{4\pi}{\lambda_0}\right)d = 2m\pi, \tag{2.4}$$

where m is the longitudinal mode order and n is the refractive index of the cavity medium between the mirrors. Of course, this is simply the 'standing wave' condition, $d = m\,\lambda_0/2n$, depicted in Figure 2.5(b). By using $\nu = c/\lambda_0$ we can express the resonance frequencies (Figure 2.5 (c)) as:

$$\nu_m = \frac{mc}{2nd}. \tag{2.5}$$

The free spectral range (FSR)is the frequency separation between two adjacent resonant modes (i.e., m and $m+1$) and is given by:

$$\nu_f = \frac{c}{2nd}. \tag{2.6}$$

26

Two key figures of merit used to characterize the light-storage capabilities of any optical resonator are the finesse ($\mathcal{F}$) and the quality factor (Q). Finesse has several physical interpretations, including that it indicates the average number of the round trips that a resonant photon makes before 'leaving' the cavity. It also represents the number of independent channels that can be resolved when the FPC is used as a spectroscopic instrument. It can be defined as

$$\mathcal{F} = \frac{v_f}{\delta_{v_m}} , \tag{2.7}$$

where v_f is the free spectral range, and δ_{v_m} is the FWHM spectral linewidth of the resonance mode m. By assuming a symmetric and low-loss cavity, and neglecting defects such as mirror roughness, unintended mirror curvature, or deviation from parallelism between mirrors, the finesse reduces to the so-called 'reflection finesse', $\mathcal{F}_R$, which is determined solely by the reflectance R of the mirrors:

$$\mathcal{F}_R = \frac{\pi \sqrt{R}}{1-R} . \tag{2.8}$$

A related measure of the photon storage time is the so-called quality factor, which is a universal measure applied to resonators, quantifying the number of 'cycles' (i.e., periods at the resonant optical frequency) for which a resonant photon is stored on average. Referring to Figure 2.5, it can be expressed:

$$Q = \frac{v_m}{\delta_{v_m}} = m\mathcal{F}_R , \tag{2.9}$$

where δ_{v_m} is known as the FWHM spectral linewidth (see Figure 2.5 (c)) of a resonant mode, and m is the longitudinal mode order ($m=1,2,3,\ldots$).

2.3.2 Spherical-mirror Fabry-Perot cavities

The planar Fabry-Perot etalon discussed above is the prototypical structure used as a model for understanding the behavior of all optical cavities, and some cavities used in spectroscopy and lasers are well-approximated by such a simple model. However, it is clearly an idealization, since it assumes mirrors of infinite extent and modes that are plane waves. Furthermore, such an idealized cavity does not provide transverse confinement of light in the directions perpendicular to the cavity axis. To achieve 3D confinement of light, one or both of the planar mirrors is replaced

by a spherical or curved mirror. Spherical mirrors essentially refocus light that is circulating inside the cavity, thereby compensating diffraction. From a ray optics viewpoint, stable modes of such a cavity correspond to ray trajectories that retrace the same path as they bounce back and forth between the mirrors, as shown in Figure 2.6. From a more fundamental perspective, the electromagnetic modes of the spherical mirror cavity are the well-known Hermite-Gaussian (or Laguerre-Gaussian) beams discussed next.
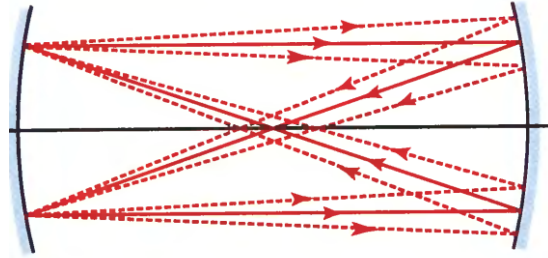
Figure 2.6. Schematic representation of light rays that' retrace themselves' as they bounce back and forth between the concave mirror and mirror refocus the circulating light [adapted from [92]].

2.3.2.1 Gaussian beam modes

The boundary conditions presented by spherical mirror resonators, under the right conditions (i.e., combinations of mirror curvature and spacing), can result in stable electromagnetic modes which are the well-known Hermite-Gaussian beams [92]. In other words, Hermite-Gaussian beams are the modes of the spherical-mirror resonator; they are also solutions of the paraxial Helmholtz equation. These well-known solutions can be utilized to predict the resonance frequencies and intensity distributions of the resonator modes. In simple terms, the Gaussian beams that are the 3-D confined modes of such cavities have wavefront curvature at the position of the mirrors that matches the curvature of the spherical mirrors (as shown in Figure 2.7)
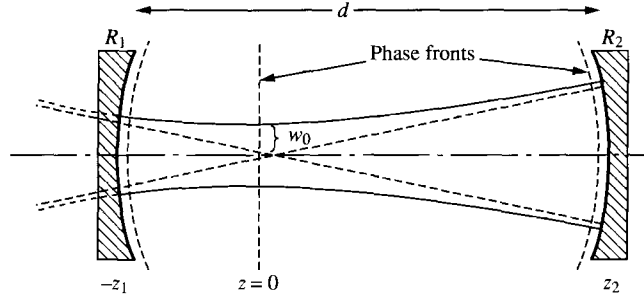
Figure 2.7. Diagram showing a spherical cavity supporting a stable Gaussian beam mode. The Gaussian beam wavefront curvature at the positions of the mirrors must match the curvature of the mirrors [adapted from [94]].

The fundamental (i.e., lowest-order, TEM$_{00}$) Gaussian beam has a radially symmetric 'Gaussian' field profile, with an intensity distribution given by the following equation:

$$I = I_0 \left(\frac{w_0}{w(z)}\right) \exp\left[\frac{-2(x^2+y^2)}{w^2(z)}\right] , \qquad (2.10)$$

where I_0 is the on-axis intensity at the beam waist, w_0 is the beam waist radius (minimum spot size at the beam waist), and $w(z)$ is the z-dependent beam spot size.

The minimum spot size radius occurs at the 'focal plane' ($z = 0$) of the beam. The minimum spot size (w_0), is the radial distance (at the beam waist) at which the intensity has fallen to $1/e^2$ of its on-axis value. This minimum spot size determines many key beam characteristics. For example, away from the beam waist, the beam diverges due to diffraction effects and the transverse dimensions correspondingly increase. The z-dependent spot size of the beam can be expressed as:

$$w(z) = w_0\sqrt{1 + \left(\frac{z}{z_0}\right)^2} , \qquad (2.11)$$

where z_0 is referred to as the `Rayleigh range' or `depth of focus', and is specified by:

$$z_0 = \frac{\pi w_0^2}{\lambda_0} , \qquad (2.12)$$

The wavefronts are spherical surfaces with radius of curvature given by:

$$R(z) = z + \frac{z_0^2}{z} . \qquad (2.13)$$

Thus, a Gaussian beam can be the stable solution of a spherical mirror resonator when the wavefront curvature (at the mirror locations) matches the mirror curvature.

More generally, solutions of the paraxial wave equation generate families of modes, in addition to the lowest-order (fundamental) mode discussed above. These are referred to as Hermite-Gaussian (HG) or Laguerre-Gaussian (LG) modes. Both HG and LG mode families represent a complete set of orthogonal basis solutions, and thus any HG mode can be represented as a weighted sum of LG modes, and vice-versa. The choice of HG or LG basis functions depends on the coordinate system (i.e., either Cartesian or cylindrical) chosen for the transverse planes. For a Cartesian coordinate system, Hermite-Gaussian modes are appropriate and can be denoted as $TEM_{l,m}$, where (l,m) are the numbers of nodal points in the electric field distribution along the x and y directions. In most practical spherical mirror resonators, there is significant deviation from cylindrical symmetry, so that the HG modes are observed in the majority of experimental systems. LG modes have mode indices that indicate numbers of nodes along the radial and azimuthal directions in a cylindrical coordinate system, and are only observed in experimental systems with extremely good spherical symmetry. The intensity profiles of some low-order Hermite-Gaussian and Laguerre-Gaussian modes are shown in Figure 2.8.
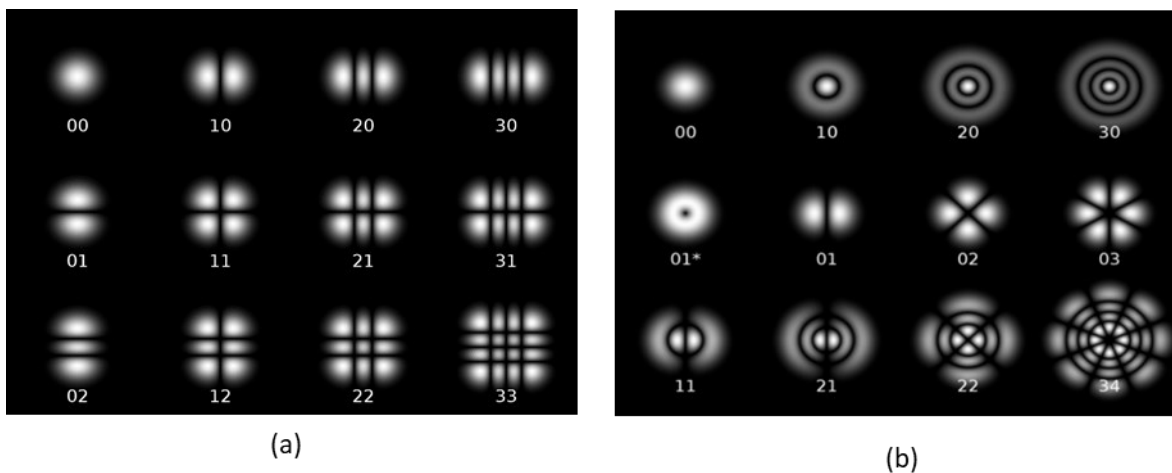
Figure 2.8. The intensity profiles of some low-order: (a) Hermite-Gaussian modes. (b) Laguerre-Gaussian modes [adapted from [95]].

2.3.2.2 Resonance frequencies

As for the planar Fabry-Perot, the longitudinal resonance condition is that a circulating wave must accumulate a round trip phase equal to the integer multiple of 2π (i.e. this is the 'integer number of half wavelengths' condition). However, due to their non-plane-wave nature, the accumulated phase shift for a Hermite-Gaussian beam must take into account the so-called 'Gouy' phase shift, which is unique for each HG mode and leads to a more complicated longitudinal phase condition [96]:

$$k_q d - (l + m + 1)\left[\tan^{-1}\frac{z_2}{z_0} - \tan^{-1}\frac{z_1}{z_0}\right] = q\pi \ . \tag{2.14}$$

Here, l and m are the transverse mode indices mentioned above, k_q is the wave number in the cavity medium, d is the axial mirror spacing, and q is the longitudinal mode order (q=1,2,3…). Furthermore, z_1 and z_2 are the positions of the cavity mirrors, as shown in Figure 2.7.

From the phase condition, the resonance frequency of a given mode can be expressed as:

$$\nu_{l,m,q} = \frac{c}{2d}\left[q + \frac{(l+m+1)}{\pi}\cos^{-1}\left[\sqrt{\left(1 - \frac{d}{R_1}\right)\left(1 - \frac{d}{R_2}\right)}\right]\right] . \tag{2.15}$$

Here, R_1 and R_2 are the radii of curvature of the mirrors. From Eq. (2.15), the first term is the longitudinal modal spacing, which is independent of the mirror curvature and identical to the result for the planar mirror resonator. However, the second term depends on the mirror curvature. The transverse field profile is identical for modes with a given combination of transverse mode indices (l,m), regardless of the longitudinal mode order q. The frequency spacing between transverse modes is given by:

$$\Delta\nu = \frac{c}{2\pi n d}\Delta(l + m)\left[\tan^{-1}\frac{z_2}{z_0} - \tan^{-1}\frac{z_1}{z_0}\right], \tag{2.16}$$

where n is the refractive index of the cavity medium. In the case of a nearly planar resonator (typical of many practical cavities with stable mode solutions), where z_1 and z_2 are comparatively smaller than z_0, i.e. R_1, R_2>>d, the preceding equation simplifies to the following result [96]:

$$\Delta\nu = \frac{c}{2\pi n z_0}\Delta(l + m) . \tag{2.17}$$

Figure 2.9 illustrates typical 'families' of resonant frequencies for such a cavity. The longitudinal mode orders (i.e., for fundamental TE$_{00}$ mode profiles) are separated by the "free spectral range" from above, i.e. $v_f = c/2\mathrm{n}d$. Higher-order transverse modes have resonant frequencies slightly above that of the corresponding TE$_{00}$ mode for a given longitudinal mode order, and the spacing between transverse modes is given by Eq. (2.17).
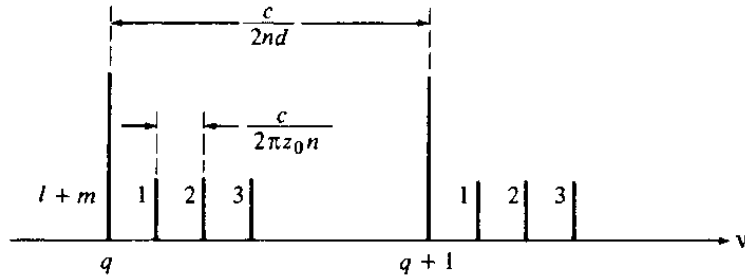
Figure 2.9. Schematic resonance frequency spectrum for a near-planar spherical mirror resonator, with d≪R$_1$,R$_2$.. The spacing between longitudinal mode orders is given by the free spectral range, while the spacing between transverse modes belonging to a particular longitudinal mode order is given by Eq. (2.17) [Adapted from [96]].

2.3.2.3 mode volume

Mode volume is another important parameter in many applications of microcavities. Conceptually speaking, the mode volume quantifies the degree of spatial confinement of light by the cavity in the same way that the Quality factor quantifies the degree of temporal confinement of the light by the cavity. The mode volume is generally defined as [94]:

$$V_M = \iiint \frac{E(x,y,z)E(x,y,z)dxdydz}{|E_0|^2} \ , \tag{2.18}$$

where E_o is the peak electric field of the cavity mode. The mode volume for any TEM$_{00}$ mode of the spherical-mirror FPC can be approximated by the following equation [54]:

$$V_M = \frac{\pi w_0^2}{4} d \ . \tag{2.19}$$

Here, w_0 is the mode waist associated with the TEM$_{00}$ mode and d is the cavity length (i.e., mirror spacing).

For the case of the half-symmetric optical cavity, the beam waist lies on the planar mirror, the beam waist (radius) for the fundamental mode can be approximated as [54]:

$$w_0 = \sqrt{\frac{\lambda}{\pi}} (L_{\text{eff}} R_{CD})^{1/4} ,\qquad\qquad 2.20$$

where L_{eff} is the effective cavity length and R_{CD} is the radius of curvature for the curved mirror (describe later). Here, $L_{\text{eff}} = \delta + 2dp$, where dp is the penetration depth into the mirrors [27].

2.4 **Laser rate equations**

According to quantum theory, matter can exchange energy with the electromagnetic field through either creation (emission) or annihilation (absorption) of a photon. Significant insight is obtained by considering a simple two-level atom interacting with a resonant optical field, where $h\nu \sim E_2 - E_1$, with $h\nu$ the photon energy and E_2 and E_1 the upper and lower energy levels of the atom. The interaction between atom and field initiates an energy exchange between them. As summarized below, there are three fundamental processes by which the atom and the field can exchange energy.

2.4.1 **Spontaneous and stimulated emission**

Photon emission occurs when the atom descends from the upper level to the lower level, thereby emitting energy. In some systems, the energy might be released via a nonradiative process, such as for example by the emission of phonons (thermal energy). The rate of spontaneous photon emission is governed by the Einstein coefficient for the transition according to the following rate equation [97]

$$\frac{\mathrm{d}N_2}{\mathrm{d}t} = -A_{21}N_2 ,\qquad\qquad (2.21)$$

Here, the proportionality constant is known as the Einstein A_{21} coefficient, and N_2 is the number of atoms per unit volume in energy state E_2.

Einstein showed that an incoming photon that is resonant with the transition can also induce a downward transition, in a process referred to as stimulated emission. This process is illustrated in Figure 2.10 (b). The rate of stimulated emission can be expressed as:

$$\frac{\mathrm{d}N_2}{\mathrm{d}t} = -B_{21}N_2\rho(\omega),\qquad\qquad (2.22)$$

Where N_2 denotes the number of atoms per unit volume in energy state $E_2[\text{m}^{-3}]$, $\rho(\omega)$ signifies the spectral energy density of the electromagnetic field at the resonant frequency $(\text{Jm}^{-3}(\text{rad/s})^{-1})$, and B_{12} is termed the Einstein B₁₂ coefficient.
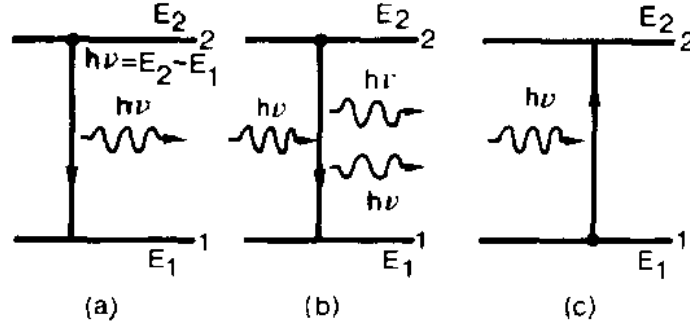
Figure 2.10. Schematic illustration of the three processes: (a) spontaneous emission, (b) stimulated emission, (c) absorption [adapted from [98]].

Of course, upward transitions can also be caused by absorption (annihilation) of resonant photons, a process known as stimulated absorption or simply absorption. An analogous rate equation for stimulated absorption, but with N_1 and B_{12} can thus be written. For a collection of identical atoms at thermal equilibrium, the rate of upward and downward transitions must be equal, which can be expressed [97]:

$$B_{12}N_1\rho(\omega) = A_{21}N_2 + B_{21}N_2\rho(\omega), \qquad (2.23)$$

The relationships between the Einstein coefficients can be derived by assuming that the atoms are in thermal equilibrium with a blackbody spectrum. Based on Boltzmann statistics for a collection of atoms at thermal equilibrium, the following equation can be asserted [97]

$$\frac{N_2}{N_1} = \frac{g_2}{g_1} \exp\left(-\frac{\hbar\omega}{\kappa_B T}\right), \qquad (2.24)$$

where g_2 and g_1 denote the degeneracies of levels 1 and 2, respectively. By using Planck's blackbody radiation formula, the spectral energy density can be written:

$$\rho(\omega) = \frac{\hbar w^3}{\pi^2 c^3} \frac{1}{\exp\left(\frac{\hbar\omega}{k_B T}\right)-1}, \qquad (2.25)$$

From Eq. (2.23), Eqs. (2.24), and (2.25), the following relationships can be derived:

$$g_1 B_{12}^\omega = g_2 B_{21}^W \,, \tag{2.26}$$

$$A_{21} = \frac{\hbar\omega^3}{\pi^2 c^3} B_{21}^\omega \,, \tag{2.27}$$

2.5 **Atom- Photon coupling inside microcavity**

The study of the interaction between an atom and a confined electromagnetic field within an optical cavity, which contributes considerably to the formation of quantum information, is called cavity quantum electrodynamics (CQED). A microcavity can confine photons and atoms within the same small volume, and thus greatly enhance the interactions between them. For near-resonant conditions, the interaction between a two-level atom and light inside a microcavity is governed by three main parameters:

- the photon decay rate of the cavity 2κ
- the non-resonant decay rate 2γ,
- the atom-photon coupling parameter $2g_0$.

Figure 2.11 illustrates these three parameters. The majority of applications of atom-cavity coupling are based on achieving one of the following two regimes: i. strong-coupling conditions, where $g_0 \gg (\kappa, \gamma)$ or ii. weak-coupling conditions, where $g_0 \ll (\kappa, \gamma)$, but typically with $\kappa \gg g_0 \gg \gamma$. We focus only on the weak coupling regime here, since it has most relevance to the proposed research.
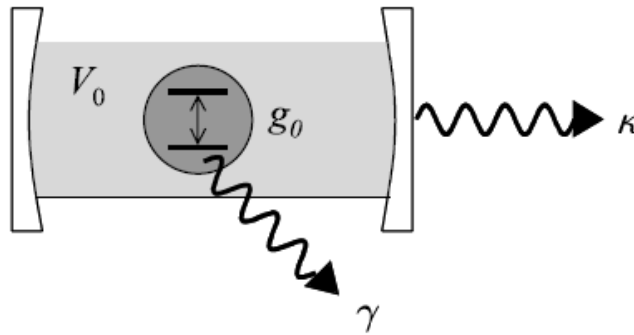
Figure 2.11. Diagram of a system showing the interaction between an atom and resonant mode inside the cavity [Adapted from [97]].

2.5.1 weak -coupling (Purcell) regime

In the weak coupling regime, the atom-cavity coupling constant g_0 is lower than the loss rate, which arises either from the escape of photons from the cavity mode (κ) or from emission into non-resonant modes (γ). In this scenario, the emission of photons from atoms inside the cavity is irreversible. Thus, there is zero possibility of re-absorption of a photon that is emitted into a non-resonant mode, or which is lost (by absorption, scattering, or transmission by the mirrors) from the cavity mode. Nevertheless, in the Purcell regime, the cavity has ability to control (i.e., suppress or enhance) the spatial and temporal emission profile of photons compared to the free space value, depending on if there is a match between the atomic transition and the resonant mode of the cavity. In the case of an emitter (i.e., atom) located inside the air cavity at a mode field maximum, and with the assumptions that the atomic transition is resonant with the cavity mode and $\gamma < \kappa$ [99,100], then the emission rate in a cavity mode of interest compared to the free space is specified by the well-known Purcell factor:

$$F_p = \frac{W^{\mathrm{cav}}}{W^{\mathrm{free}}} = \frac{3}{4\pi^2}\frac{Q}{(V_M/\lambda_0^3)} \; ,$$

(2.28)

where Q is the quality factor, V_M is mode volume, and λ_0 is the free space wavelength. The expression in Eq. 2.28 assumes an emitter in a vacuum. Thus, a high Purcell factor requires small mode volume and high Q. It should also be noted that the expression above assumes that the spectral width of the cavity resonance is broader than line-width of the emitter.

2.6 Buckling delamination: morphology and theoretical aspects

2.6.1 Buckling delamination of thin films

The buckling delamination of thin-film structures has mainly been studied as an unwanted phenomenon that causes failure in electronics and optoelectronics applications. High biaxial compressive stresses and low adhesion are the main factors that play a significant role in the buckling delamination of a deposited thin film from its substrate. As mentioned, this phenomenon is typically unfavorable and is associated with device failure. However, our group has exploited a

controlled delamination and buckling process in order to fabricate air-core microcavities and waveguides [1,81]. In this approach, film buckling due to the above-mentioned conditions is exploited as a 'self-assembly' process, by patterning some specific regions of the proposed wafer to possess lower adhesion. Experimentally, this can be achieved through the deposition and patterning of a weak adhesion layer. To maintain good optical properties of the produced cavity (i.e., low absorption and scattering loss in the visible and near-infrared wavelength ranges of interest), most of this work has employed a Teflon-like fluoropolymer layer deposited using the passivation cycle of a standard deep reactive ion etching (DRIE) process (i.e., the well-known 'Bosch' process). This fluorocarbon layer has the properties of being highly transparent and has typically been found to have negligible effects on the optical properties of the resulting microcavity. It should be noted that using this method of fluorocarbon thin-film fabrication has contributed to the production of many functional optical and MEMS-like devices reported in the literature [1,81,82,101].

2.6.2 Circular delamination buckles – basic theory

The formation of delamination buckles over a circular region of low adhesion and driven by compressive stress can be analyzed by employing the so-called elastic buckling theory of a circular plate having clamped boundaries on the edges [102]. According to this theory, buckling will take place if the compressive stress of the 'film' (i.e., the top mirror multilayer in our case) exceeds the critical stress value σ_c derived from the elastic buckling theory:

$$\sigma_c = 1.2235 \left(\frac{E}{1 - v^2} \left(\frac{h}{a} \right)^2 \right), \tag{2.29}$$

in which E is the modulus of elasticity of the considered layer (i.e., which is a multilayer Bragg mirror treated as an effective medium in our case), v is the Poisson ratio of the layer, h is the thickness of the layer, and $a = D/2$ is the radius of the circular region subject to delamination. As shown in Figure 2.13 (the process flow), when a compressively stressed upper mirror is deposited over patterned circular regions of low adhesion, and an empirically optimized heating step is applied, circular delamination buckles are induced to form 'spontaneously'.

According to these predictions of elastic buckling theory, these circular delamination buckles have a specific shape described mathematically by a Bessel function equation (see Eq. 2.30 below) and shown schematically in Figure 2.12. In practice, the profile can be influenced by other factors such as plastic deformation occurring in the stacked multi-layer and relaxation of the compressive stress in the buckled film. By neglecting the plastic deformation effect on the final geometry shape of the buckles and assuming a pure elastic elongation behaviour for the deformed thin film with clamped rigid boundaries at the ends (see Figure 2.12 for clarification), the buckling profile can be predicted by the following expression [86,103]:

$$\Delta(r) = \delta[0.2871 + 0.7129.J_0(\mu r)]. \tag{2.30}$$
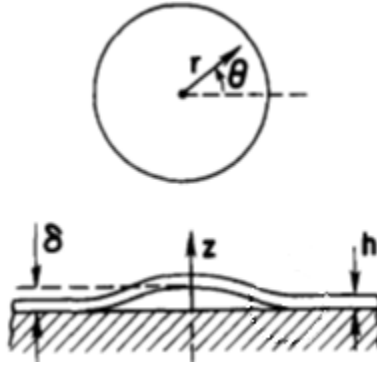
Figure 2.12. Configuration of the buckled film, showing δ is a height of the delamination, and h is a thickness of the film [adapted from [103]].

Here Δ is the vertical displacement of the thin film structure, r is the normalized radial coordinate of the buckled dome, J_o is the Bessel function of the first kind and order zero, δ is the peak height of the buckle dome, and $\mu = 3.8317$ is the first zero of the Bessel function of the first kind and order one. The peak height or displacement of the buckled dome can be calculated analytically for a known biaxial thin-film compressive stress [86]:

$$\delta = h\left[1.9\left(\frac{\sigma}{\sigma_c} - 1\right)\right]^{1/2} \approx \left[\frac{1.9\sigma(1 - v^2)}{1.2235E}\right]^{1/2}\frac{D}{2}. \tag{2.31}$$

The above-derived expression is valid provided $\sigma \gg \sigma_c$ and assuming purely elastic deformation of the buckled film. As we stated earlier, plastic deformation can occur in highly stressed films and may consequently cause some deviation between the true measured and predicted values of the peak buckle height as well as the profile of the delamination buckle.

The effective radius of curvature of the buckled mirror is another crucial parameter that controls the modal volume and specifies the optical modal behaviour of the Bragg reflector mirror. It can be calculated through applying the following formula [1]:

$$R_{CD} = \frac{D^2}{8\delta} + \frac{\delta}{2}.$$

(2.32)

It is worth mentioning that to induce buckling at the first onset of the process, the applied heat load should be controllable. This starts by heat up the substrate, which in turn will transfer the applied heat flux to the other different components of the proposed structure (listed in the Table 2.1) and cause a state of thermal expansion due to the different thermal properties in addition to the disintegration of the weak adhesion layer. A temperature of $\cong 300 - 350 \ {}^oC$ has typically been used to satisfy the condition of buckling onset and at the same time adhesion reduction as well as redistribution of compressive stresses.

Table 2.1. Mechanical Properties of materials.

Material	E(GPa)	v
a-Si	60-100	0.22
SiO_2	72	0.17
Ta_2O_5	100-140	0.23

2.7 Fabrication

In this section, we describe the general steps that are used to fabricate dome microcavities by buckling self-assembly. In general, the fabrication of Dome microcavity is partitioned into four stages (see Figure 2.13):

i. Deposit the bottom distributed Bragg reflector (DBR) mirror onto a cleaned, double-side-polished silicon wafer, using an RF magnetron sputtering system.

ii. Deposit and pattern a thin layer of the low adhesion layer, which is a 'Teflon-like' fluorocarbon film, deposited using the Bosch process passivation cycle (DRIE).

iii. Deposit a top mirror using the same RF magnetron sputtering system used for the bottom mirror.

iv. Subject the sample to a high temperature around 300 °C, in order to induce loss of the adhesion over the area of the patterned fluorocarbon layer, and thereby produce buckle dome cavities.

Bottom Mirror Dep

Low Adhesion Layer

Top Mirror Dep

Heat Sample to Introduce Buckling
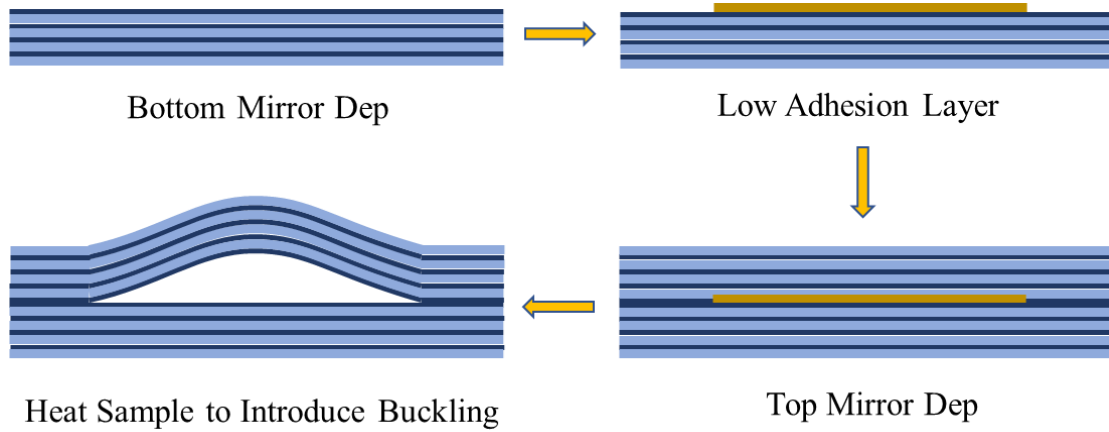
Figure 2.13. Schematic diagram showing fabrication process.

Chapter 3 [1]

Cooperativity enhancement in buckled-dome microcavities with omnidirectional claddings

We describe a theoretical study of dipole emitters inside buckled-dome Fabry-Perot cavities with Si/SiO$_2$-based omnidirectional Bragg mirrors. The low penetration depth of the mirrors contributes to low mode volumes, potentially enabling large enhancement of spontaneous emission into moderate-quality-factor cavity modes. Furthermore, the omnidirectional mirrors can significantly inhibit background emission. For a representative cavity operating in a fundamental spatial mode regime at $\lambda \sim 1550$ nm, and an optimally located emitter, we predict simultaneous enhancement of emission into the cavity mode by ~120 and suppression of background emission by ~25, implying the potential for a cooperativity $C \sim 1500$. This is combined with $Q \sim 10^3$, significantly lower than is required to attain similar values of C without background inhibition, and thus implying better compatibility for broad line-width emitters.

3.1 Introduction

As first described by Purcell (see for example [104]), spontaneous emission must be viewed as a cooperative process involving an emitter and its surrounding electromagnetic environment. This has led to widely studied concepts for the enhancement of emission into a desired mode [9–11] or the suppression/inhibition of emission into undesired modes [12,13], with optical microcavities playing a central role. Control over spontaneous emission is the key enabler of several proposed 'quantum' light sources, such as the threshold-less laser [105] and the controlled source of single photons (i.e., the single-photon source, SPS) [54,106].

Micro-scale confinement of light results in a set of sparsely distributed, small-volume cavity modes, such that the rate of emission into a single preferred mode can be greatly enhanced (i.e., the 'Purcell effect') [104]. However, control of emission through the Purcell effect alone requires that both the cavity and the emitter have a narrow linewidth. This requirement is effectively lifted in cases where the microcavity inhibits emission into other modes (e.g. the leakage into

---

[1] This chapter was published in *Optics Express*, vol 26, no.9 pp. 11201, 2018

background radiation modes [12]). Most microcavities (e.g., microspheres, micro-pillars, microdisks, defects in 2-D photonic crystals) rely at least partially on total-internal-reflection-based confinement, and require additional engineering [107] to suppress emission into background radiation modes. A more ideal scenario is provided by defect micro-cavities formed within 3-D photonic crystals, which can, in principle, greatly suppress the local density of optical modes (LDOM) within one or more stop bands, thereby enabling essentially all spontaneous emission (over a broad wavelength range) to be directed into a single desired mode [13]. However, such cavities are challenging to implement at optical frequencies.

As is now well-known, 1-D photonic crystals (i.e., thin-film Bragg mirrors), under appropriate conditions [89], can exhibit an omnidirectional reflection band for light incident from a lower-index external medium. However, unlike 3-D photonic crystals, the 1-D omnidirectional reflector (ODR) supports in-plane 'guided' modes at all frequencies [108], including the spectral bands associated with external omnidirectional reflection. Nevertheless, for an emitter that is located in the external medium and at a sufficient distance to minimize coupling to the evanescent fields of these in-plane modes, it is possible for the 1-D ODR to facilitate significant inhibition of spontaneous emission [51,109].

Motivated by this, Xu *et al*. proposed and fabricated [52] a novel 'onion' microcavity with a spherical air core surrounded by ODR claddings, and subsequently analyzed its potential for the modification of spontaneous emission [53,110], showing that it might be possible to inhibit background emission by several orders of magnitude. This is an exciting property, which makes the onion resonator resemble the defect cavity within a 3-D photonic crystal. However, the onion resonator is also a challenging structure to fabricate, and moreover does not provide a convenient means for external coupling to the cavity modes of interest. Here, we demonstrate that buckled-dome microcavities [1] clad by ODRs can provide many of the same benefits, while offering much simpler fabrication and the possibility for straightforward and efficient coupling to the cavity modes by external fibers or free-space beams.

3.2 **Background and overview**

We have previously reported [1,82,86] experimental results on half-symmetric Fabry-Perot cavities fabricated by guided delamination-buckling within a thin film mirror stack. These cavities can be fabricated in large arrays, and the self-assembly nature of the fabrication process results in

a very high defect-finesse. Reflectance-limited finesse and 'textbook' manifestations of Laguerre-Gaussian (LG) cavity modes have been achieved in both the 780 nm [82] and 1550 nm [86] wavelength ranges. Furthermore, cavity height (and thus resonance conditions) can be varied within a certain range through control of film stress and the choice of base diameter, and tuned on a finer scale through temperature control [86].

3.2.1 Representative experimental structure

As a test case for the modeling study, we focus on the small-mode-volume cavities from Ref [83]. A fundamental mode volume on the order of one cubic wavelength in the 1550 nm-range was demonstrated, and attributed in part to the high index contrast of the Si/SiO_2-based mirrors employed. Also of central importance to the present study, these mirrors provide a broad band of omnidirectional reflection for light incident from a lower index medium [89,101], such as from the air core of a buckled cavity.

As shown in Figure 3.1(a) (and detailed elsewhere [83]), the cavities considered have a base diameter of ~50 μm and a peak height of ~0.78 μm. The lower mirror is deposited on a standard silicon substrate (n_{Si} ~3.5) and the upper curved mirror is adjacent to the external environment (i.e. typically air, n ~1). Note that the cavities in Ref [83] have 5-period mirrors, but we assume 4-period mirrors (with an additional a-Si 'capping layer' on the upper buckled mirror [1,86]) for the theoretical study below. Given typical absorption losses for our a-Si layers (deposited by pulsed-DC magnetron sputtering), the addition of the fifth period produces only marginal (or even negligible) increase in reflectance and finesse, but significantly degrades the potential transmittance $\psi = T/(T + A)$ of the mirrors, and thus the out-coupling efficiency for an embedded emitter. We furthermore assume indices n_{aSi} ~3.7-0.0009i and n_{SiO2} ~1.47 at 1550 nm wavelength, for the a-Si and SiO_2 layers, respectively. While our experimental process (employing a shared-use deposition system) is subject to some variability in film loss [83], these values are representative of the lowest-loss mirrors we have produced in our previous work (resulting in R~0.999, T~A, and ψ ~0.5 [111]). Finally, quarter-wave layers at 1550 nm wavelength, corresponding to nominal layer thicknesses ~105 nm and ~264 nm, respectively, were assumed in all theoretical treatments below.
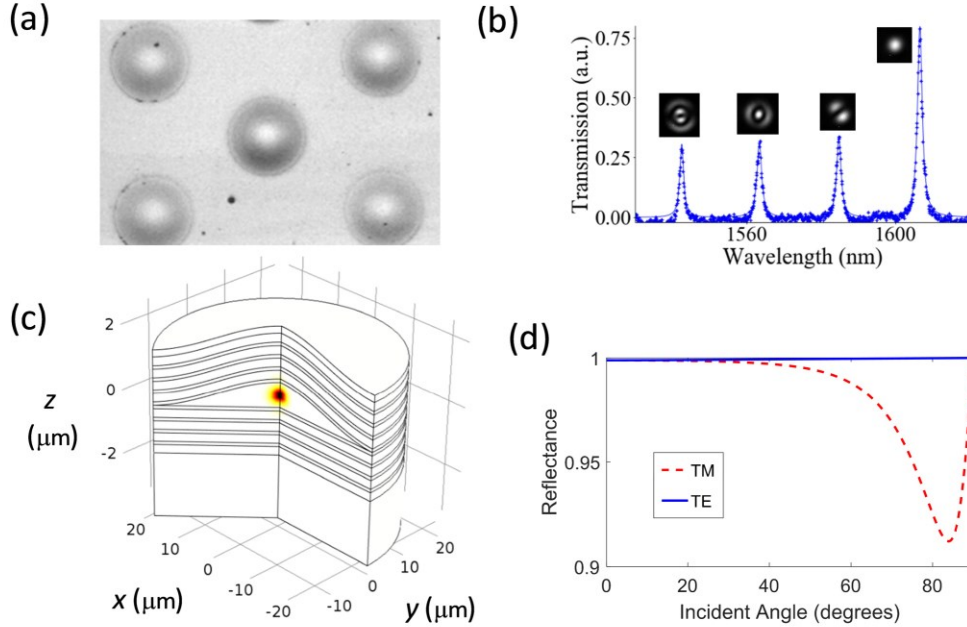
Figure 3.1. (a) Microscope image of a portion of a large array of 50-μm-base-diameter domes. (b) Typical wavelength scan showing a fundamental resonance (at ~1610 nm for this particular cavity) and several higher-order transverse resonances. The solid lines are Lorentzian fits, and mode-field-intensity images associated with each resonance are shown as insets. (c) Schematic 3-D cut-out view of a buckled dome cavity, showing the fundamental resonant mode (at ~1527 nm using the cavity parameters described in the main text) predicted by a finite-element numerical simulation. (d) Predicted reflectance versus incidence angle from air at 1550 nm wavelength, for the 4-period lower mirror of the cavities.

Figure 3.1(b) shows a typical experimental transmission scan, which as discussed elsewhere [83] reveals good agreement with predictions from paraxial Gaussian beam optics for a spherical mirror cavity. The buckled mirror has effective radius of curvature ~200 μm, resulting in a transverse mode spacing $\Delta\lambda_T$ ~22 nm for the half-symmetric cavity. The mirrors have normal-incidence reflectance R ~0.999, limited mainly by residual absorption in the a-Si layers, enabling a cavity finesse ~2-3x10^3 [111] (also note that $Q \sim \mathcal{F}$ for the fundamental spatial mode of interest here). A finite-element (COMSOL Multiphysics) simulation (see Figure 3.1(c)) predicted V_M ~1.3λ^3 at ~1527 nm, in good agreement with our previous results [83] and with the FDTD simulations described in Section 3.4. Finally, Figure 3.1(d) shows transfer matrix simulations for a planar mirror with the thicknesses and indices mentioned above. At 1550 nm wavelength, the mirrors provide high omnidirectional reflectance for both polarizations, although there is some leakage for TM polarization at large angles. The omnidirectional reflection band spans the ~1300-1700 nm range [101].

3.2.2 High-level description of spontaneous emission processes

A buckled dome cavity with an embedded dipole emitter is depicted in cross-section in Figure 3.2 (a). Note that the electromagnetic modes available to the emitter can be categorized as follows: (A) The Laguerre-Gaussian (LG) modes of the air-core half-symmetric cavity; (B) the vacuum radiation modes; and (C) the cladding modes guided within the mirrors. As discussed above, we made some key simplifying assumptions as follows. First, given the spectral separation of the LG modes, we assume that the emitter is spectrally aligned to only the fundamental cavity mode and that coupling to higher order LG modes is negligible. Second, given the high-reflectance-omnidirectional-band of the cladding mirrors, the rate of emission into radiation modes is anticipated to be very low [110]. Thus, background emission is expected to be dominated by coupling to the cladding modes (i.e. light guided within the omnidirectional mirror layers [53]).

(a) (b)
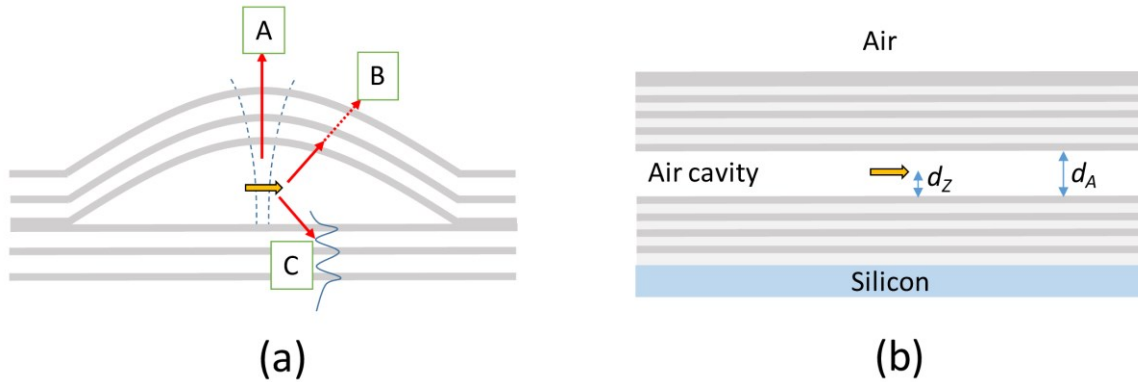
Figure 3.2. (a) Schematic diagram of a dipole emitter (indicated by the horizontal block arrow) inside a buckled dome microcavity, showing 3 possible routes for spontaneous emission. Emission into a cavity mode (A) can be predicted by the Purcell factor, emission into free-space vacuum modes (B) is assumed to be negligible due to the omnidirectional nature of the cladding mirrors, and emission into cladding modes (C) can be treated approximately using a planar model. (b) Planar model used to estimate the rate of emission into cladding modes. The dipole is placed at some distance d_Z from the interface with the bottom mirror.

Given these assumptions, the goal is to estimate the rate of emission into the cavity and cladding modes of the structure, which will in turn yield estimates of the cooperativity and the spontaneous emission coupling factor. Of course, the enhanced rate of emission into the fundamental cavity mode is the Purcell effect and can be estimated using well-known expressions [104]. To estimate emission into cladding modes, we adopt a planar model for the buckled cavity as depicted in Figure 3.2(b) and described in greater detail in Section 3.3. The

planar approximation is well-justified by the low aspect ratio of the buckled domes (i.e., peak height ~0.78 μm and base diameter ~50 μm). In other words, the electromagnetic environment for an emitter located near the center of the cavity is expected to be closely approximated by the planar environment shown in Figure 3.2(b). 3-D numerical simulations were used to verify these approximate results, and are described in Section 3.4.

3.2.3 Definition of key parameters

It is worthwhile to briefly summarize a few pertinent quantities. First, note that we define the Purcell factor as $F_P \equiv \gamma_C/\gamma_0$, quantifying the rate of emission into a cavity mode of interest relative to the free-space emission rate. For an emitter located in air and at the field maximum, and spatially and spectrally aligned to the cavity mode, the 'ideal' Purcell factor is given by the well-known expression [104] $F_{P0} = \{3/(4\pi^2)\}\{Q_{EFF}/(V_M/\lambda^3)\}$. For an emitter linewidth $\Delta\lambda_{EM}$ less than the cavity mode linewidth, we can write $Q_{EFF} \sim Q_C$, where Q_C is the cavity quality factor. On the other hand, for a broad linewidth emitter (but still aligned to the cavity mode), $Q_{EFF} = (Q_C^{-1} + Q_{EM}^{-1})^{-1}$, where $Q_{EM} = \lambda/(\Delta\lambda_{EM})$ is the effective quality factor of the emitter [110].

A related figure of merit is the single-atom cooperativity, which can be expressed [99]:

$$C \equiv \frac{g^2}{2\kappa\gamma_{BG}} = \frac{\gamma_c}{2\gamma_{BG}} , \qquad (3.1)$$

where g is the atom-cavity coupling parameter (i.e. $2 \cdot g$ is the vacuum-Rabi frequency [99]), $2 \cdot \kappa$ is the rate of photon loss from the cavity mode, and $2 \cdot \gamma_{BG}$ is the rate of spontaneous emission into all modes other than the cavity mode of interest (some authors, e.g. Ref [106], use the terminology 'transverse emission rate' to denote emission into these other modes). For many cavities, $\gamma_{BG} \sim \gamma_0$, and *in that case only* it follows that $F_P \sim 2 \cdot C$ [106]. In general, the relationship is $C = F_P \cdot (I/2)$, where we define $I \equiv \gamma_0/\gamma_{BG}$ as the inhibition factor, quantifying the suppression of spontaneous emission into modes other than the cavity mode of interest.

Another important parameter is the spontaneous emission coupling factor β, which is the fraction of photons extracted from the cavity mode of interest, often stated as $\beta = F_P/(1+F_P)$. However, the latter equation implicitly assumes $\gamma_{BG} \sim \gamma_0$ and also neglects the possibility for loss of cavity-mode photons (e.g., due to scattering or absorption by mirror layers). A more general and correct expression is as follows [99]:

$$\beta = \frac{\kappa_{out}}{\kappa} \frac{\gamma_C}{\gamma_{BG}+\gamma_C} = \frac{\kappa_{out}}{\kappa} \frac{2C}{1+2C}, \tag{3.2}$$

where (κ_{out}/κ) represents the fraction of cavity mode photons extracted in the output beam (in part determined by the potential transmittance ψ of the out-coupling mirror). The key point is that C and β can be increased both by enhancing emission into the cavity mode (i.e. the Purcell effect) and by suppressing or inhibiting emission into other modes [51,53,110,107]. A high inhibition factor is especially attractive in the case of relatively broadband emitters where F_{P0} is limited by the low Q_{EM}, since C and β can nevertheless potentially be large [110].

3.3 Quasi-analytical planar model

We first consider spontaneous emission by a dipole embedded within the planar cavity shown in Figure 3.2(b). We restrict the analysis to the case of a horizontal dipole; this is the orientation expected to couple most efficiently to the fundamental LG cavity mode of interest in the actual curved-mirror cavity. We also assume the dipole to be embedded in air, at some distance d_Z from the bottom mirror interface. Rigorous treatment of spontaneous emission requires a quantum electrodynamics formalism, which accounts directly for the polarization of the emitter by the zero-point fluctuations of the vacuum field, summing over all possible modes [112]. However, in the weak-coupling limit (expected to be valid for most emitters in the cavities described here, given their moderate Q values [104]), spontaneous emission can also be treated classically. In the classical view, the spontaneous emission rate of the dipole is modified by its own reflected field, and can be quantified by the local density of modes (LDOM), in turn given by the imaginary part of the electromagnetic Green's function at the dipole location inside the (generally) inhomogeneous environment. Multiple authors have derived the Green's function for planar (slab) structures (see for example Neyts [113], and references therein), and used the results to assess LDOM and spontaneous emission modification. Here, we follow the formalism provided by Tomas [114,115], the spontaneous emission rate into TE- and TM-polarized modes (normalized to the free-space emission rate), for a horizontal (in-plane) oriented dipole, can be written [108,116]:

$$\frac{\gamma_{TE}}{\gamma_0} = \frac{3}{4k_0} Re \int_0^\infty \frac{dk_{//} k_{//}}{k_Z} \frac{\{1 + r_{TE}^+ \exp[-2i.k_Z(d_A - d_Z)]\}\{1 + r_{TE}^- \exp[-2i.k_Z d_Z]\}}{(1 - r_{TE}^+ r_{TE}^-.\exp[-2i.k_Z d_A])} \quad ;$$

$$\frac{\gamma_{TM}}{\gamma_0} = \frac{3}{4k_0^3} Re \int_0^\infty dk_{//}k_{//}k_Z \frac{\{r_{TM}^+\exp[-2i.k_Z(d_A - d_Z)] - 1\}\{r_{TM}^-\exp[-2i.k_Zd_Z] - 1\}}{(1 - r_{TM}^+r_{TM}^-.\exp[-2i.k_Zd_A])} \qquad . \qquad (3.3)$$

Here, r^+ and r^- are the Fresnel reflection coefficients at the interface between the air cavity and the upper and lower mirrors, respectively. Furthermore, $k_{//}$ is the in-plane component of the wave-vector, conserved in all layers of the slab structure, k_0 is the free-space wave number at the frequency of interest, and $k_Z = (k_0^2 - k_{//}^2)^{1/2}$ is the normal component of the wave vector in the air-core layer containing the dipole. We evaluated the total rate of spontaneous emission $\gamma = \gamma_{TE} + \gamma_{TM}$ by numerical evaluation of the integrals in (3). Fresnel reflection coefficients were calculated using a standard transfer-matrix formalism [90]. Note that the evaluation of the integrals is somewhat simplified by inclusion of material loss in the silicon layers, which avoids the poles associated with lossless guided modes [113]. Note also that the contributions of different categories of modes can be assessed independently by changing the limits of the integration. For $k_{//} > k_0$, for example, the field in the air core layer is evanescent, and modes in this range can be identified as 'cladding modes'.

3.3.1 Dipole in a half-wavelength thick air cavity

Consider a dipole located inside the air cavity depicted in Figure 3.2(b), with both the upper and lower mirrors terminated by quarter-wavelength, high-index layers adjacent to the air core. At the design wavelength of 1550 nm, the (vertical emitting) fundamental cavity mode corresponds to d_A $\sim \lambda/2$. The standing-wave field profile (not shown) exhibits nodes at the mirror interfaces and a peak (anti-node) at the mid-point of the air cavity. Figure 3.3 shows results from numerical integration of Eq. (3.3) , with the air core thickness set at $d_A = 0.776$ µm. In order to illustrate the nature of the modes that make the dominant contributions to the LDOM, plots of the integrand in the TE expression are shown in Figure 3.3(a). For a dipole emitting at 1550 nm and located at the center of the cavity, the LDOM is dominated by the fundamental cavity mode, which occurs for near-normal incidence in this case. The four additional peaks in the LDOM spectrum are associated with the in-plane guided modes of the 4-period claddings (which can be viewed as 4-channel multilayer slab waveguides [90]), and are, relatively speaking, weakly coupled since the dipole location is $\sim \lambda/4$ removed from the mirror interfaces. Analogous behavior occurs for the TM modes, as shown for one representative case in Figure 3.3(a). The extra peak is due to coupling to a surface mode.
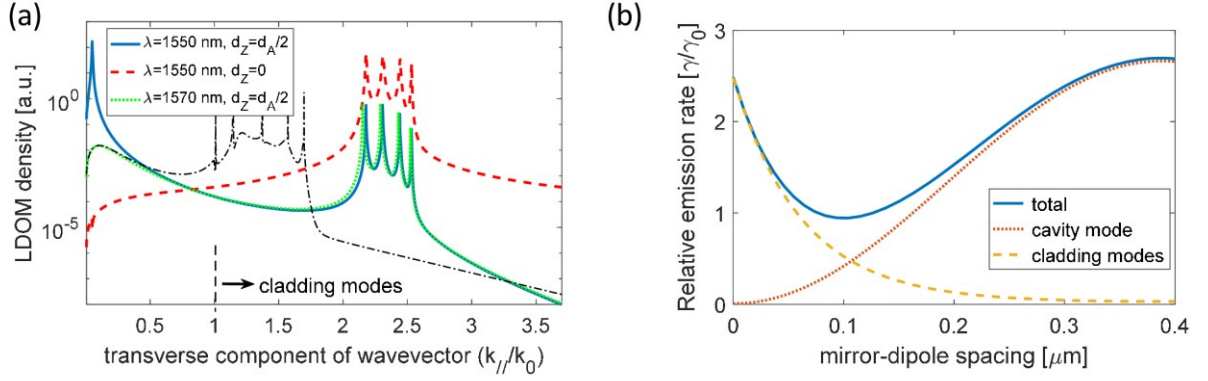
Figure 3.3. (a) The LDOM distribution (i.e., the integrand of the TE expression in Eq. (3.3)) in transverse-wave-vector space is plotted for various dipole positions and emission wavelengths. The integrand of the TM expression for one representative case ($\lambda = 1570$ n nm, $d_Z = d_A/2$) is also shown (dash-dot line). (b) The total relative emission rate ($\gamma_{TE} + \gamma_{TM})/\gamma_0$ for a dipole emitting at $\lambda = 1550$ nm is plotted versus dipole location relative to the bottom mirror interface. The contributions from the cavity mode (i.e. $0 < k_{//} < k_0$) and the cladding modes (i.e. $k_{//} > k_0$) are also shown separately.

The dashed red line in Figure 3.3 (a) corresponds to the same emission wavelength but with the dipole located at the interface to the bottom mirror. Since the cavity mode exhibits a node at this location, its contribution to the LDOM vanishes. Due to the omnidirectional claddings, emission into radiation modes is also very weak, as apparent from the relatively low LDOM density in the $k_{//} < k_0$ region. However, emission into the cladding modes is much higher in this case, since the dipole overlaps more strongly with their evanescent fields extending into the air core. Finally, the dotted green line corresponds to a dipole located at the center of the cavity but emitting at a longer wavelength subject to cut-off of the fundamental cavity mode. As might be expected, the cavity mode contribution to the LDOM is greatly suppressed but the contributions from the cladding modes is nearly identical to that predicted for the resonant case. These simulations confirm that background emission is dominated by emission into the cladding modes. In other words, $\gamma_{BG} \sim \gamma_{CLAD}$, where γ_{CLAD} is the spontaneous emission rate estimated by evaluating the integrals in Eq. (3.3) over the range $k_{//} > k_0$.

Figure 3.3 (b) is a plot of the total relative spontaneous emission rate for the same cavity as in part a, with the wavelength set to 1550 nm and the dipole position varied. Contributions from core ($0 < k_{//} < k_0$) and cladding ($k_{//} > k_0$) modes are also plotted separately. The behavior is consistent with results predicted elsewhere for omnidirectional-clad planar cavities (e.g. see Fig. 7 in ref [116]). Emission into cladding modes dominates for small dipole-mirror spacing, but becomes

negligible when $d_Z > \lambda/4$. For a dipole optimally located at the center of the air cavity ($d_Z \sim 0.375$ μm), the model predicts $\gamma_C/\gamma_0 \sim 2.7$ (which is near the upper limit for a planar structure [105]) and $\gamma_{BG}/\gamma_0 \sim \gamma_{CLAD}/\gamma_0 \sim 0.031$. A more conservative estimate can be obtained by evaluating the integrals in (3) over the entire range encompassing both radiation and cladding modes, but at an off-resonant wavelength (such as the $\lambda = 1570$ nm case depicted in Figure 3.3 (a)). This results in $\gamma_{BG}/\gamma_0 \sim 0.04$, thus $I \sim 25$. Using this latter value and neglecting mirror loss (i.e. assuming $\kappa_{out} = \kappa$), Eq. (3.2) then predicts $\beta \sim 0.992$ (when $C \sim 70$) for the half-wavelength planar cavity. This is consistent with the value ($\beta \sim 0.98$($C \sim 25$) predicted by St. J. Russell *et al.* [51] for a water-filled cavity clad by similar mirrors. The higher value here is mainly due to the assumption of an air core, which results in stronger decay of the evanescent cladding mode fields away from the mirror interfaces (i.e. γ_{CLAD} is approximately a factor of 3 lower here).

We can now speculate on the highest potential cooperativity for emission into the fundamental mode of the buckled dome microcavities described above. For the case of 3-D confinement, the maximum rate of emission into the cavity mode is given by the Purcell factor for a narrow linewidth resonant emitter. Using $V_M \sim 1.3\lambda^3$ and $Q_C \sim 2 \times 10^3$ (see Section 3.2.1), it follows that $F_P \equiv \gamma_C/\gamma_0 = F_{P0} \sim 120$. Furthermore, in keeping with the arguments above, we postulate that the background inhibition factor can be extracted from the planar model and is thus given by $I = \gamma_0/\gamma_{BG} \sim 25$. For the optimally positioned horizontal dipole, this suggests a potential for cooperativity as high as $C = F_P \cdot I/2 \sim 1500$. While similarly high values of cooperativity might be possible for highly optimized fiber Fabry-Perot cavities [54], those projections were predicated on much higher quality factor ($Q \sim 10^6$). Such high Q-factor places restrictions on the emitter linewidth, and complicates the spectral alignment of the emitter to the cavity mode.

3.3.2 Dipole at the interface of the bottom mirror

While the value for C estimated in the previous section is compelling, it represents an ideal scenario in which a dipole emitter is trapped at the center of the air cavity. Techniques for isolating and trapping atoms have become quite sophisticated [117], but this is nevertheless a daunting challenge in practice. An alternative approach is to use a solid-state emitter embedded near the interface of one of the cavity mirrors [59,118]. Typically, the mirror in question is terminated by a low-index layer, so that the cavity field anti-node is aligned with the emitter position. Figure 3.4(a) shows a plot of the mode field intensity profile at resonance, for a planar cavity formed by

combining a quarter-wave air layer and a quarter-wave 'spacer' layer (with index $n_D = n_{SiO2}$ for the particular example shown). Termination of the lower mirror by a low-index SiO_2 layer reduces its reflectance slightly, thereby reducing the cavity Q and finesse. To compensate this, such that Q_C is similar to the case above, we added an additional quarter-wave a-Si layer to the upper mirror (i.e., the a-Si capping layer was changed from a half-wave to a quarter-wave thickness, thus making it a 4.5-period mirror). The mirrors were otherwise assumed to have layer indices and thicknesses as described in Section 3.2.1. As expected, the field anti-node is aligned with the top surface of the spacer layer, so that a dipole placed there can couple efficiently to the cavity mode.
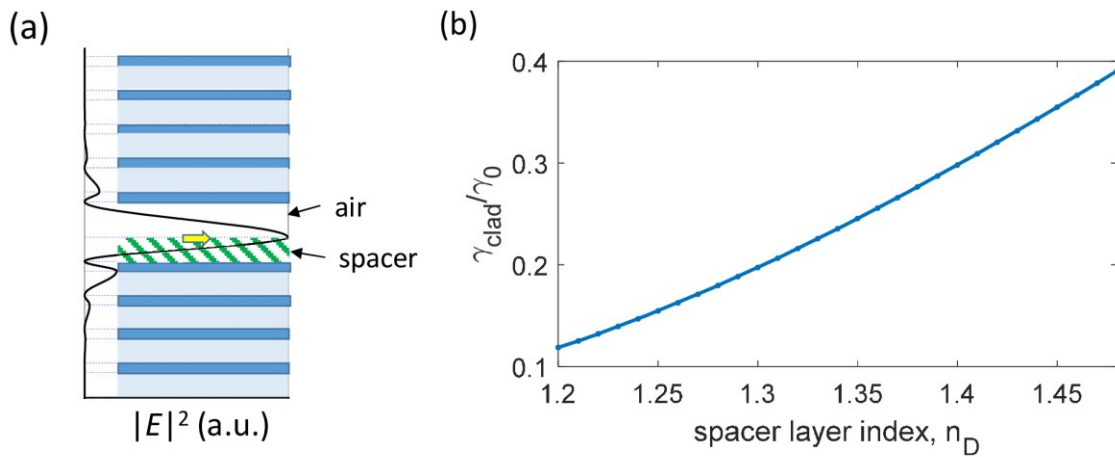
Figure 3.4. (a) The fundamental mode intensity profile is plotted for a planar cavity comprising a quarter-wave air layer and a quarter-wave spacer layer with refractive index n_D. The multilayer structure, including 4.5- and 4-period upper and lower mirrors, respectively, is overlaid on the plot. A dipole emitter at the air-spacer interface is also depicted. (b) The predicted rate of emission into cladding modes is plotted versus spacer layer refractive index, for a horizontal monochromatic ($\lambda = 1550$ nm) dipole at the air-spacer interface, and with the spacer layer set to quarter-wavelength optical thickness in each case.

Using the planar model described above, we estimated the emission rate into cladding modes as a function of the spacer refractive index, for a horizontal dipole located at the air-spacer interface. The results are shown in Figure 3.3(b), and demonstrate that, for this more practical scenario, significant suppression of the background emission rate might still be possible. For example, simply using SiO_2 as the spacer layer still results in $I \sim 2.7$, corresponding to $C \sim 160$ for the cavity mode described above. Of course, this estimate again assumes a sufficiently narrow linewidth emitter, such that $Q_{EFF} \sim Q_C$. A similar strategy for suppressing the emission into the cladding modes of an omnidirectional-clad hollow fiber was proposed by Bermel et al. [109].

3.4 **Numerical modeling results**

The quasi-analytical predictions from above clearly involve a few assumptions, particularly regarding the use of a planar model to approximate background emission for the real buckled dome cavities. To corroborate the results, a numerical study was conducted using a commercial FDTD software package (Lumerical). A 3-D structure was defined by using an experimental cross-sectional profile, fit to a Bessel function curve as predicted by elastic buckling theory [83], with peak buckle height 0.776 μm. Multilayer parameters, including thicknesses, indices, and loss were chosen as described in Section 3.2. A series of simulations were performed with increasing simulation times and decreasing mesh size, in order to confirm the convergence and accuracy of the results.

Figure 3.5(a) shows a typical fundamental mode-field profile extracted from the FDTD solution, which predicted $V_M \sim 1.3\lambda^3$ and $Q_C \sim 2000$ at the fundamental mode resonant wavelength ($\lambda \sim 1527.3$ nm in this case). Figure 3.5(b) shows the relative emission rate predicted for an electric dipole oriented parallel to the plane of the substrate and located precisely at the center of the air cavity. Note that the software has a built-in capability to calculate dipole emission rates relative to the case of the dipole in vacuum. In very good agreement with the analytical approximations above, the predicted on-resonance emission rate is ~ 120 and the off-resonance emission rate saturates (for long wavelengths) to a value of ~ 0.04. As discussed in Sections 3.2 and 3.3, these correspond approximately to the Purcell factor $(\gamma_C/\gamma_0 \sim 120)$ for the fundamental cavity mode and to the inhibition factor ($I \sim 25$) for background emission, thus confirming the estimate $C \sim 1500$ from Section 3.3.1.
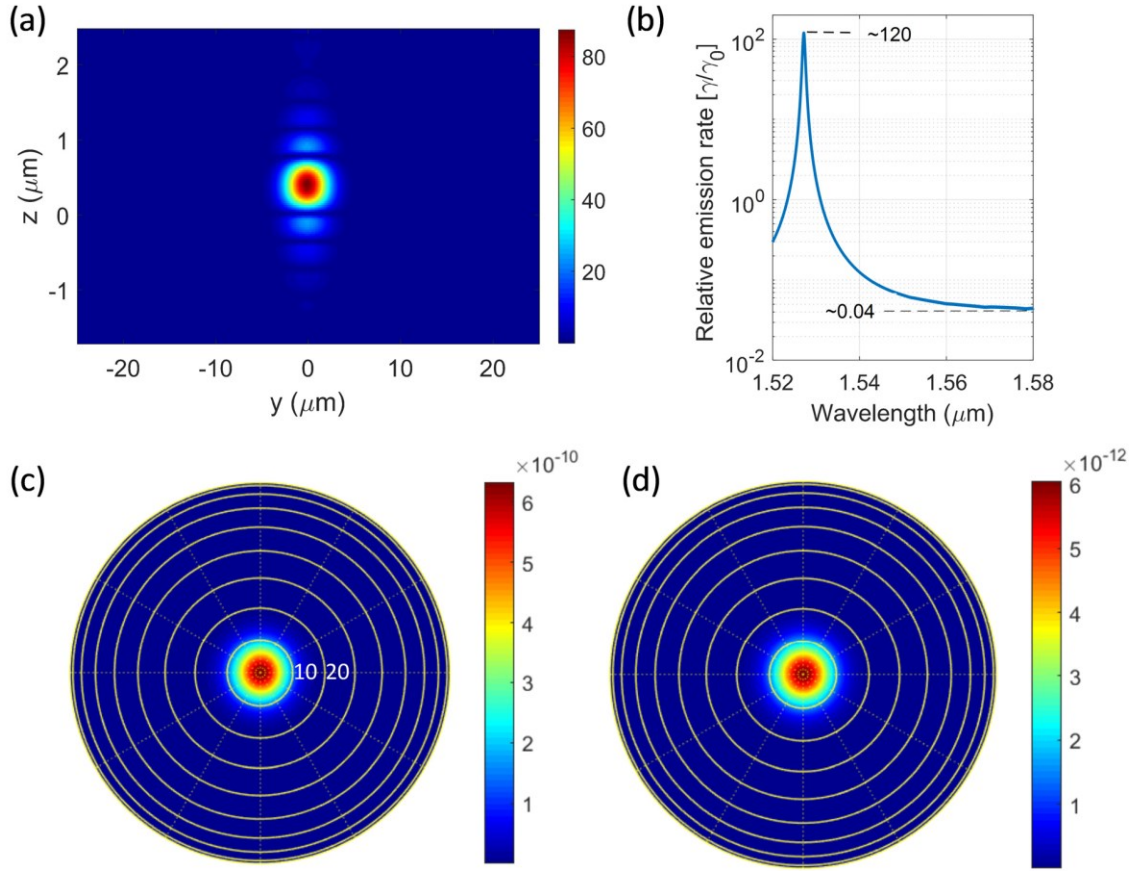
Figure 3.5. (a) Cross-sectional mode-field profile at the resonant wavelength λ ~1527.3 nm for a buckled cavity with ~λ/2 air-core thickness, as predicted by the FDTD-based solution. (b) Wavelength-dependent emission rate relative to the free-space emission rate, for a horizontally oriented dipole located in the middle of the air cavity. (c) Far-field projection of the power radiated from the top of the buckled cavity at the resonant wavelength. The plot is a 2-D representation (i.e., 'overhead' view, with the angle relative to normal indicated by the concentric circles in increments of 10 degrees) of the power distribution on a hemispherical surface of radius 1 m. (d) As in part (c), but for λ ~1531.1 nm.

A rough estimate for the spontaneous emission coupling factor was made as follows. The angular distribution of power radiated through the upper buckled mirror of the cavity was solved using built-in 'far-field projection' capabilities of the software. As an example, the far-field intensity distribution at the fundamental resonance wavelength (~ 1527.3 nm) is plotted in Figure 3.5(c). The plot is an 'overhead' view of the power distribution on a hemispherical surface of radius 1 m, with the concentric circles indicating the polar angle relative to the normal direction. Note that the fundamental Gaussian mode waist radius is w_0 ~2.47 μm for this cavity (from the FDTD results), corresponding to a predicted far-field divergence half-angle $\theta = \lambda/(\pi w_0)$ ~11.4

degrees. It is apparent from visual inspection of the plot that most of the radiated power lies within this range, and is thus coupled to the fundamental mode. By comparing the numerically integrated power to Gaussian-beam analytical predictions, we conservatively estimated that > 0.99 of the power emitted through the upper mirror is contained within the fundamental cavity mode. A similar analysis of the power radiated through the bottom mirror was in good agreement. This calculation neglects details such as the residual coupling to cladding modes (which is small, as discussed) and the angular dependence of the residual absorption by the mirror layers, which will tend to suppress far-field emission at high angles more than at normal incidence. Nevertheless, the result is consistent with the expectation of a near-unity value for β when mirror losses are neglected. In other words, assuming $\kappa_{out} = \kappa$ and using $C = 1500$, Eq. (3.2) predicts $\beta = 0.9997$.

As a further illustration, Figure 3.5(d) shows a similar far-field plot, but for a wavelength (λ ~1531 nm) slightly detuned from cavity resonance such that F_P ~1 (see Figure 3.5(b)). Note that the emitted power is ~2 orders of magnitude less at this wavelength, as expected from the reduction in Purcell factor (and thus peak emission rate). In spite of this, even at this off-resonance wavelength, most of the out-coupled light is associated with the cavity mode. This is due to the strong suppression of radiation modes by the omnidirectional mirrors. From the discussion in Section 3.2.3 and neglecting mirror loss, we expect $C = F_P \cdot I/2$ ~12.5 and β ~0.96 in this case. As above, we compared the numerically integrated power to the Gaussian beam prediction, and estimated that > 0.95 of the far-field radiated power is contained in the fundamental cavity mode at this wavelength. This provides further corroboration of the results in Section 3.3, and furthermore illustrates that, even without significant Purcell enhancement, a high spontaneous emission coupling factor can be attained when background emission is suppressed [110].

Finally, Figure 3.6(a) shows the fundamental field profile predicted for a 'spacer-embedded' cavity, of the type discussed in Section 3.3.2. For this cavity, an additional SiO_2 (spacer) layer was added to the bottom mirror. Furthermore, the base diameter of the buckled mirror was set to 44 μm and the peak buckle height was set to 0.388 μm (i.e., a quarter-wave air layer at ~1550 nm wavelength). These values of base diameter and peak height were estimated based on the predictions of elastic buckling theory, as verified in our previous experimental work [86]. As discussed in Section 3.3.2, a 4.5-period upper mirror was used to compensate the reduced reflectance of the bottom mirror due to its low-index termination by the spacer layer. Also due to

the addition of the spacer layer, the field penetration into the bottom mirror is somewhat increased (i.e. compare Figure 3.5(a) and Figure 3.6(a)). Thus, both Q_C and V_M are increased slightly compared to the non-spacer cavity above, but the ideal Purcell factor is similar in both cases. Figure 3.6(b) shows the predicted relative emission rate versus wavelength, for a horizontally aligned dipole located at the interface to the bottom mirror (i.e. at the top of the SiO_2 spacer layer, see Figure 3.4(a)). Both the on-resonance ideal Purcell factor (F_{P0} ~120) and the off-resonance inhibition factor (I ~1/0.3) are in good agreement with the analytical model from Section 3.3, confirming the potential for cooperativity $C > 150$. As above, these estimates assume a well-aligned emitter of sufficiently narrow linewidth to ensure $Q_{EFF} \sim Q_C$.
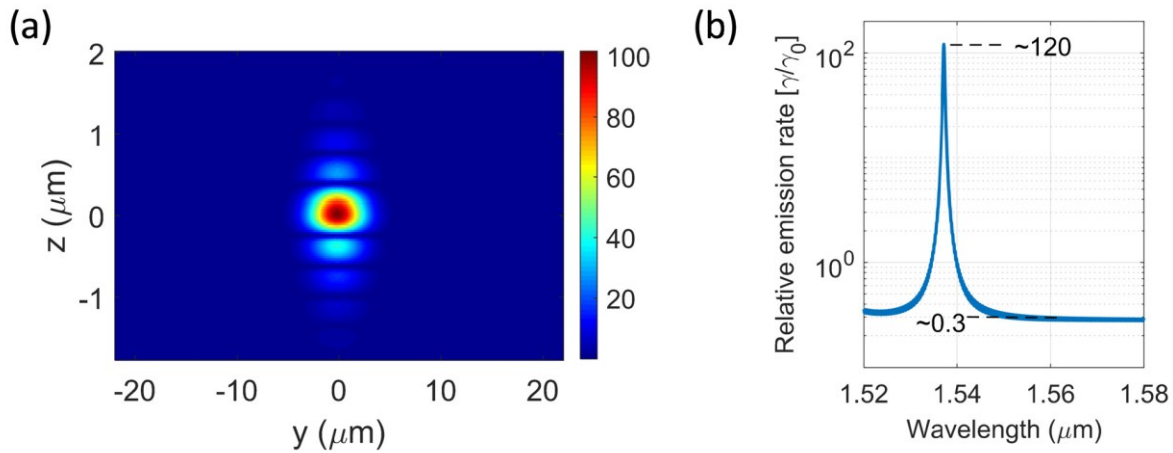
Figure 3.6. (a) Cross-sectional mode-field profile at the resonant wavelength λ ~1537.2 nm for a buckled cavity with ~λ/4 air-core thickness and ~λ/4 SiO_2 spacer layer, as predicted by the FDTD-based solution. (b) Wavelength-dependent emission rate relative to the free-space emission rate, for a horizontally oriented dipole located at the top of the spacer layer.

3.5 **Discussion and conclusions**

We have demonstrated that buckled-dome microcavities clad by omnidirectional reflectors might enable very high cooperativities, even for moderate Q. Assuming parameters extracted from previously fabricated cavities with $Q_C \sim 10^3$, we predict values as high as $C \sim 1500$ for an optimally located dipole emitter, due to significant inhibition of background emission by the omnidirectional claddings. Furthermore, assuming mirror losses can be reduced, near-unity spontaneous emission coupling factors might also be possible, even for relatively broadband emitters. It should be

emphasized that precise positioning of an atomic emitter inside a buckled dome cavity remains a significant challenge. However, the monolithic nature of the fabrication process might lend itself to incorporation of nano-scale emitters, for example by patterned assembly [119] prior to the deposition and buckling of the upper mirror. Furthermore, in our previous work we have explored the fabrication of both nano-scale holes [82] and intersecting channels [83] as a means to provide open access for liquid- or gas-phase emitters. We hope to investigate these options in future work.

The benefits described, including the suppression of background emission over a wide spectral range and the possibility for mode volume approaching λ^3, can be attributed (at least in part) to the high refractive index contrast provided by the a-Si/SiO$_2$-based mirrors. Of note, there is currently a significant worldwide effort aimed at the development of hydrogenated a-Si (a-Si:H) films for microphotonics. Optimized a-Si:H films can provide at least 3-4 orders of magnitude reduction in absorption loss at 1550 nm wavelength [120], compared to the typical value for the sputtered a-Si films described above. This could in turn dramatically improve both the attainable finesse and the out-coupling efficiency of the mirrors. Moreover, there is currently a strong motivation in the cavity QED literature to develop emitters and cavity devices for the so-called 'telecom' ranges, especially near the 1550 nm wavelength region best-suited to long-haul fiber transmission. Significant efforts towards the integration of 1550 nm range emitters (e.g., InAs/InP quantum dots [121,122], PbS quantum dots [123], and erbium [124]) with silicon-photonics devices are ongoing, and the present study is of direct relevance.

Nevertheless, cavity QED work has traditionally been conducted in the wavelength range below 1 μm, motivated by the wide variety of suitable emitters operating in this range (e.g. rubidium atoms and defect centers in diamond) and also by their compatibility with silicon-based single-photon detectors. TiO$_2$/SiO$_2$-based mirrors can be used in this range, and have sufficient index contrast to produce bands of omnidirectional reflection for incidence from air [89]. On the other hand, many studies have employed Ta$_2$O$_5$/SiO$_2$-based mirrors [59], which cannot provide omnidirectional reflection. Interestingly, for onion cavities Liang *et al.* [53] showed that even non-omnidirectional (SiN/SiO$_2$-based) mirrors could provide significant suppression of background emission under certain conditions. The degree of spontaneous emission modification possible in buckled cavities with lower-contrast mirrors is thus an interesting topic for future study.

Finally, it is worth mentioning that there is significant scope for optimization of the buckled-dome cavities. The present study was focused on a particular cavity geometry previously

shown [83] to provide operation in a fundamental spatial mode regime, with correspondingly low mode volume. As discussed above, the moderate cavity Q is determined primarily by the residual absorption losses of the mirrors, and might be significantly increased through the use of a-Si:H. Furthermore, larger cavities can easily be fabricated [1], and could enable greater suppression of background emission for emitters located in the air core, due to the possibility for greater separation between the emitter and the mirror interfaces. The choice of a larger cavity would also imply higher V_M and Q_C (at relatively fixed F_{P0} [54]), which would be desirable for certain emitters and applications.

Chapter 4

Monolithic curved-mirror Fabry-Perot cavities with embedded SiO:Er light-emitting layers

This chapter describes attempts to develop a monolithic fabrication process to embed 1550-nm-wavelength-range active light-emitting layers (SiO:Er) inside arrays of on-chip, buckled-dome Fabry-Perot microcavities. Even with the addition of these active layers, we verified that the cavities can exhibit high-finesse and predictable Laguerre-Gaussian modes. Emission from the embedded SiO:Er active layers was excited using various laser pump sources through a host-absorption-mediated process that transfers pump energy to the Er ions. Preliminary evidence for cavity-enhanced emission is provided. The work is a stepping-stone towards a future vision of on-chip arrays of tunable cavity QED systems operating at telecom wavelengths. We discuss refinements and modifications that will be needed to achieve such a vision.

4.1 Introduction

Erbium (Er) -doped glasses and crystals are immensely important in modern technology, owing to their ability to emit and amplify light in the low-loss transmission band of optical fibers (i.e., in the ~1550 nm wavelength region, sometimes called the 'telecom band'). In glasses, the emission is very broad due to local-environment variations for individual Er ions inside the inherently random glass network. Furthermore, the metastable lifetime of the transition responsible for the ~1550 nm emission is typically very long (milliseconds) [125]. Both of these properties make Er-doped glasses extremely useful as an amplifying medium in broadband fiber networks. However, they are disadvantages in the context of 'quantum' light sources such as single-photon emitters (SPEs) [126]. For quantum applications, coherent (i.e., narrow linewidth) emission from transitions between discrete energy levels, high photon emission rates (i.e., short emission lifetimes), and nearly identical properties (i.e., 'indistinguishable' photons) across all emitting sites (i.e., Er ions) is needed. This motivates the study of Er-doped crystalline hosts such as Y_2O_3 [124], which has been recently shown to retain most of its desirable properties even in the form of nanocrystals [127].

Cavity quantum electrodynamics (CQED) principles (see Chapters 1-3), such as Purcell enhancement, can partially address these challenges and are the subject of much recent interest for Er-doped materials [48,124,128]. A properly designed microcavity with small mode volume and high-quality factor can increase the interaction between a cavity mode and an emitter, and accordingly, be used to control/modify the spontaneous emission rates (i.e., to either enhance emission on resonance or inhibit emission off-resonance). In fact, integration of emitters with optical microcavities has attracted great research interest owing to their potential applications in quantum sensors [7,8] and single-photon sources for quantum cryptography [129,130]. For erbium specifically, enhanced light emission based on erbium-doped silicon in 2D Photonic crystals [48] and coherent emission by erbium dopants embedded in a high Q resonator at cryogenic temperatures [20] have been demonstrated.

The current chapter describes a set of fabrication and measurement procedures that were developed in order to: i. investigate the incorporation of patterned SiO:Er films inside buckled dome microcavities, and ii. study the emission from SiO:Er pads coupled to the cavity resonators. The fabrication of buckled dome cavities operating in the telecommunication (~1550 nm wavelength) range, and with erbium-doped silicon monoxide layers embedded into the buckling self-assembly process, was achieved. Fully integrated devices were attempted using two different strategies. The first attempt employed an a-Si/SiO$_2$ top mirror, while the second attempt employed a Ta$_2$O$_5$/SiO$_2$ top mirror. The study also investigates the applicability of a home-built microscope setup to the measurement of cavity transmission and photoluminescence (PL) by embedded Er ions.

4.2 Study of Erbium doped silicon monoxide embedded in dome microcavities.

As mentioned above, future work aimed at quantum emission in the telecom band might require Er-doped crystalline films or nanoparticles. As a stepping stone to such a future goal, we conducted preliminary studies using erbium-doped, amorphous silicon monoxide (SiO:Er) films, deposited through a collaboration with Prof. Al Meldrum (U of A Physics) [131,132]. These films are easily deposited using a thermal evaporation technique and the erbium emission is activated through a relatively low temperature (< 500 °C) annealing step [131]. This greatly simplifies their incorporation into our buckling process, compared to the use of crystalline or even SiO$_2$ hosts,

both of which typically require much higher processing temperatures. Furthermore, the SiO:Er system enables 'host-mediated' pumping (excitation) of the Er atoms over a broad wavelength range spanning from the UV to the NIR [133]. In addition to allowing great flexibility in choosing the pump source, this 'host-mediated' pumping has orders of magnitude higher effective cross-section than the conventional direct excitation of the Er atoms using laser sources at ~980 nm wavelength. This is very important for the study of photoluminescence from very thin films, as is envisioned here, since it enables the use of relatively low-power pumping sources.

In a preliminary study, thin films of SiO:Er were deposited in a high-vacuum physical vapor deposition (PVD) system. Two separate holders for thermal vaporization were equipped within the (PVD) system, to facilitate deposition of the SiO:Er thin films using two source materials, silicon monoxide (99.9 % pure) and Erbium (99.9% pure). Details of the deposition conditions can be found in Ref. [134]. A previous study by A. Hryciw *et al.* [131] showed that 0.2 at % Er concentration resulted in the highest photoluminescence yield, so that composition was chosen for the present work.

To facilitate a photoluminescence study, films of SiO:Er with varying thicknesses (~ 40, 100, 150, and 200 nm) were deposited under high vacuum onto a fused silica substrate, using a moving shutter to create a stepped thickness gradient. Subsequently, the sample was annealed for 1 hour in forming gas (95% N_2 +5% H_2) at a temperature of 500 ℃, to optically activate the Er ions [131].

To confirm the activation of the erbium, the sample was optically pumped by ~10 mW continuous wave excitation power using an Argon ion laser. For each section of the sample (i.e., each film thickness), photoluminescence spectra were gathered using an optical fiber-coupled system in Prof. Meldrum's lab. A long-pass filter was placed after the optical fiber to block residual pump light, while the long wavelengths were permitted to pass to a diffraction grating coupled to an InGaAs array detector (cooled IR detector). Figure 4.1 shows a typical photoluminescence curve measured for the SiO:Er film of 200 nm thickness. The emission spectrum exhibits a typical shape observed for Er^{3+} ions embedded in a glassy host [135–137].
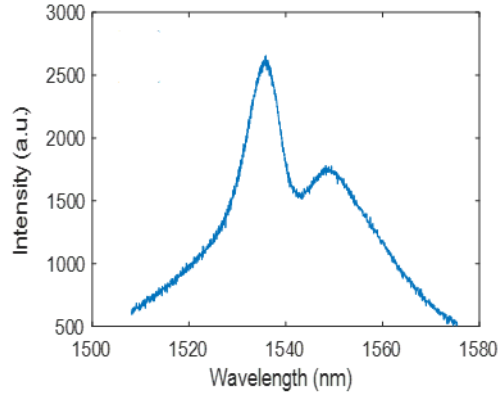
Figure 4.1. Photoluminescence curve for a typical SiO:Er film (~200 nm thick) pumped by an Argon ion laser.

4.2.1 Device fabrication

The standard fabrication procedure for buckled domes has been described in detail elsewhere [1,81,101] and an overview is also provided in Section 2.7. Here, only important steps are summarized briefly as follows. The standard process can be partitioned into four stages and starts with deposition of the bottom distributed Bragg reflector (DBR) mirror onto a cleaned, double-side-polished silicon wafer, using an RF magnetron sputtering system. Next, a thin layer of the low adhesion material, which is a 'Teflon-like' fluorocarbon film, is deposited and patterned. The passivation cycle of the Bosch (DRIE) process is used to deposit the fluorocarbon film. Later, a top mirror is deposited using the same RF magnetron sputtering system as used for the bottom mirror. Last, the wafer is subjected to an empirically optimized heating step (either on a hot plate or in a rapid thermal annealing system) up to a maximum temperature of ~300 °C. This heating promotes loss of adhesion in the areas of the patterned fluorocarbon layer, and thus produces buckled dome cavities. To integrate an emitter layer inside the cavities, the basic fabrication process was slightly modified as described in the following sections.

4.2.1.1 First attempt: a-Si/SiO₂ Based Top Mirror

A first attempt to incorporate erbium-doped silicon monoxide (SiO:Er) films into buckled dome microcavities was implemented using a slightly different fabrication strategy as compared to the process previously described in Refs. [1] and [81]. Prior to the beginning of the fabrication process, it was speculated that the patterned pad of the SiO:Er layer inside the dome microcavities might degrade their optical properties (i.e., finesse and quality factor). In addition, it was expected that if the alignment of the SiO:Er pads was a little bit off the center of the cavity, then the cavity field anti-node wouldn't overlap perfectly with the emitter position. Such a misalignment would lower the targeted enhancement of the spontaneous emission. To scrutinize the effect of the SiO:Er films inside a cavity, we first made a mask with a variety of sizes of the SiO:Er pads (from 1μm to 10 μm in diameter) aligned to buckled dome cavities with base diameters in the range from 30 μm to 150 μm. The process flow for embedding SiO:Er pads into buckled dome cavities is depicted in Figure 4.2.
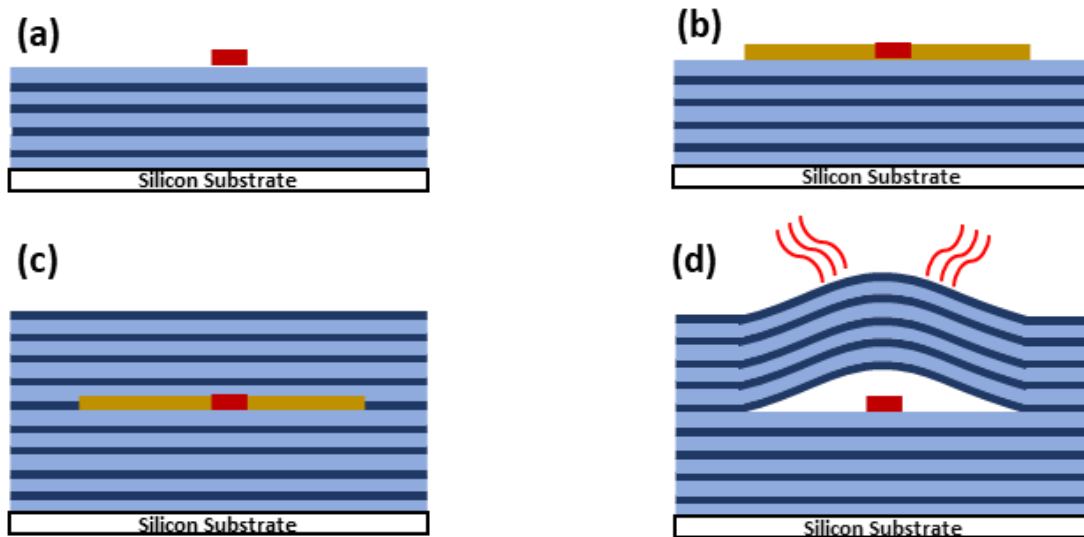
Figure 4.2. Process for embedding SiO:Er emitter 'pads' inside buckled dome cavities. (a) The thin layer of SiO:Er is deposited using PVD onto an a-Si/SiO₂ Bragg mirror, then patterned by liftoff, and annealed. (b) To define locations for the buckled dome cavities, a low-adhesion fluorocarbon layer is then deposited and patterned by liftoff, aligned to the SiO:Er pads from the previous step. (c) A second (top) Bragg mirror is deposited. (d) Heating is applied to the sample to drive the 'self-assembly' of cavities through delamination buckling over the circular patterned regions of the fluorocarbon layer.

As shown, the process started with the deposition of a 4.5-period SiO_2/a-Si quarter-wave-stack (QWS) mirror, using a reactive magnetron sputtering system (the 'Doug' system at the U of A nanoFab) onto a Piranha cleaned double-side-polished silicon substrate. The layer thicknesses were chosen in order to center the fundamental stop band of the Bragg mirror at ~1550 nm wavelength. Prior to the mirror deposition, optical constants were estimated using variable-angled spectroscopic ellipsometer (VASE) measurements on single thin films. At a wavelength of 1550 nm, the extracted refractive indices for a-Si and SiO_2 were $n_h \approx 3.7$ and $n_l \approx 1.47$, respectively, and the estimated extinction coefficients were $\kappa_h < 1 \times 10^{-2}$ and $\kappa_l < 2 \times 10^{-3}$ for a-Si and SiO_2, respectively. All depositions were performed at a substrate temperature of ~ 150 °C to ensure the correct stoichiometry of the silicon dioxide films [138] and in order to get high compressive stress and low loss for the films. In all cases, the base chamber pressure was 1×10^{-6} Torr, and Argon flow rate was fixed at 50 SCCM for all materials. For both a-Si, and SiO_2, the identical targets of 99.999% pure n-type Si were utilized. The rates, parameters, and pressures for the materials used are summarized in Table 4.1.

Note that the bottom mirror was terminated by a low-index $\lambda/4$ SiO_2 layer. As shown later, this is to ensure good alignment between antinodes of the resonant cavity electric field and the embedded emitter (SiO:Er) layer. Bottom mirror deposition was followed by the etching of alignment markers; these marks were etched through the bottom mirror and into the underlying silicon substrate to a depth of ~1.7 µm. Next, on top of this mirror, features for SiO:Er pads were patterned in HPR 504 photoresist using a standard recipe, and then a thin layer of Erbium-doped silicon monoxide (SiO:Er) (~40 nm thickness) was deposited by physical vapour deposition (PVD) as described above and in Refs. [131,132]. A standard lift-off technique was then applied to form circular SiO:Er pads, with diameters of 1.5 µm, 2µm, and 10 µm. However, only the 10 µm diameter features survived after the liftoff process. After deposition and patterning of the SiO:Er pads, the wafer was diced into four quarters, and then annealed at 500 °C for 1 hour under forming gas (95% N_2+5% H_2) in order to 'activate' the erbium layer [131].

Table 4.1. Parameters used to Deposit Layers in the 'Doug' Sputtering System

Material	Deposition Pressure (mTorr)	Deposition Rate (nm/s)	O_2 flow(sccm)	Ar flow(sccm)
a-Si	3.0	0.142	NA	50
SiO_2	4	0.26	3.2	50
Ta_2O_5	4	0.23	20	40

A spectroscopic ellipsometer (VASE) was used to assess the reflectance of the bottom mirror after SiO:Er deposition. The experimental result from VASE along with the transfer matrix simulation for the target DBR [101] is plotted in Figure 4.3(a) and they showed good agreement. The stress of this Bragg reflector mirror was measured using the Flexus Wafer Stress Measurement system, revealing overall compressive stress of ~230 MPa.

To construct Fabry-Perot 'dome' microcavities, circular features were defined in photoresist using the alignment markers described above to align these circles with the SiO:Er pads. This was followed by deposition of a low-adhesion layer (the fluorocarbon layer as described above), see Figure 4.3(b). In order to smooth the top surface of the LAL [81], the sample was then annealed on a hot plate for 1 hour. The temperature of the hot plate was kept at 100 $^\circ$C throughout the annealing procedure.

Finally, a second (4-Period) Si/SiO_2 Bragg reflector, terminated with a half-wave amorphous Si (a-Si) capping layer, was deposited on the top of the patterned low adhesion layer (LAL) [83]. The total thickness of the top mirror is ~1.7 μm. Since the chips have a variety of dome sizes (from 30 μm to 150 μm), the quarter-wafer was diced into ~1 cm by 0.5 cm dies. Through an additional heating step on individual dies, buckling of the upper mirror was induced over the circular fluorocarbon features, producing a low yield of half-symmetric (i.e. dome-shaped) microcavities with embedded SiO:Er pads (see Figure 4.3(c)).
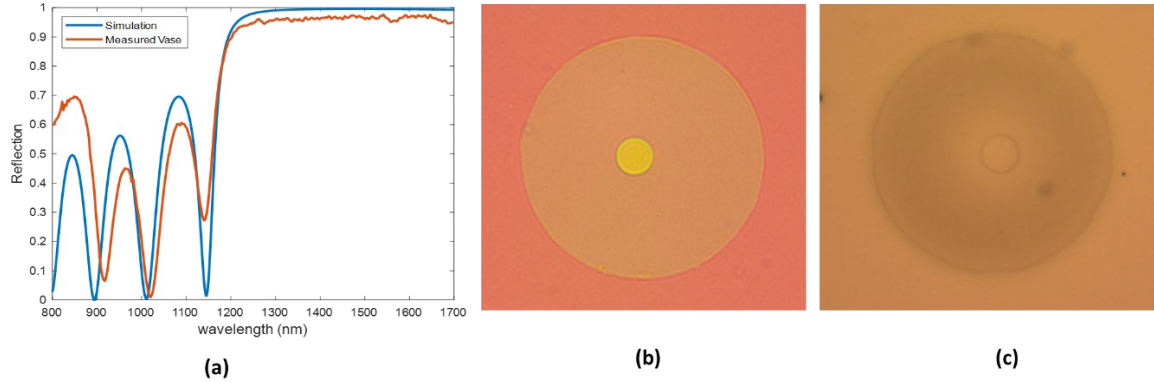
Figure 4.3. (a) VASE-measured reflectance of a 4.5-period SiO_2/a-Si mirror terminated by a thin layer of SiO:Er, plotted alongside the reflectance predicted by a transfer matrix simulation. (b) Microscope photograph showing a patterned low-adhesion layer (the larger circle, 70 μm in diameter) aligned (approximately) to a SiO:Er pad (the distinctly yellow, smaller circle in the middle, 10 μm in diameter). (c) Microscope image of a buckled-dome cavity with 70 μm base diameter and peak height ~ 2 μm. The embedded SiO:Er pad is visible near the center of the cavity.

Unfortunately, this fabrication attempt resulted in a very low yield of buckled domes, with less than 4% of the patterned fluorocarbon circles producing a delamination buckle. For example, for one chip that contained 450 potential domes, only 10 domes of 70 μm base diameter and 7 domes of 60 μm base diameter were successfully formed in the buckling step. In retrospect, this was attributed to the fact that the fluorocarbon layer was deposited directly onto a SiO_2 film surface here, conditions which we have previously associated with low buckling yield [139]. Apparently, the fluorocarbon/SiO_2 interface is too adhesive to allow consistent and reliable delamination. One of the best results, with a patterned SiO:Er pad contained within a buckled dome cavity and reasonably well-aligned to the center of the cavity, is shown in Figure 4.3 (c). In spite of the low yield, the morphology and optical properties of the few 'good' domes were studied, and information about those domes is summarized in Section 4.3.1. For example, optical profilometer (ZYGO) scans can be used to estimate the peak heights (δ) of the domes.

Unfortunately, in this first set of domes, none were initially found that had a suitable height to produce a low-order cavity resonance overlapping with the Er emission band in the ~ 1520 – 1560 nm wavelength range. Nevertheless, transmission scans with a tunable laser did reveal the existence of higher-order cavity modes, as shown for example in Figure 4.4(a). In an attempt to bring some of the domes into alignment with the Er emission band, a chip was annealed to release some of the compressive stress in the upper mirror, and thus to reduce the height of the domes. Tests were first conducted on other buckled chips (from another study), in order to establish a

suitable peak temperature and ramp rate to achieve the targeted height reduction. Different peak temperatures of 200 °C, 250 °C, 300 °C and 350 °C, and ramp rates of 10 °C/min and 15 °C/min were examined. These tests revealed that 300 °C at a ramp rate of 15 °C /min was a suitable set of conditions to satisfy our goals. However, when the SiO:Er-pad samples were subsequently annealed in this manner, it was observed that the pre-existing domes had been destroyed (the upper mirrors essentially 'popped off' during the annealing). Fortunately, some of the previously unbuckled features on the sample were found to have successfully formed into dome cavities after this additional annealing step. Furthermore, several of the new domes were measured to have heights lying in a promising range to produce fundamental resonances within the Er emission band. As an example, a fundamental mode resonance for a particular cavity is shown in Figure 4.4(b).

(a)   (b)
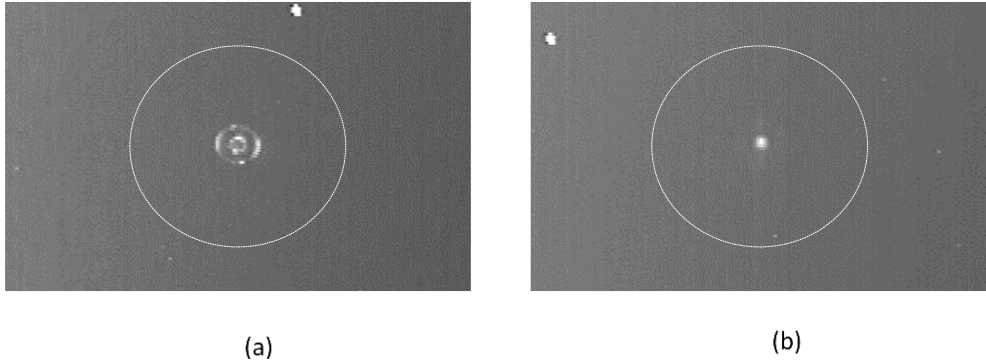
Figure 4.4. Infrared camera images of a mode-field intensity profile for: (a) a higher-order mode, and (b) a fundamental transverse mode, for domes of 70 μm base diameter and with an embedded SiO:Er 'pad' (diameter ~ 10 μm). The white dashed line indicates the perimeter of the dome cavity in each case. The peak cavity height was estimated (from profilometer measurements) to be ~ 2.1 μm and ~ 1 μm for the domes shown in (a) and (b), respectively.

4.2.1.2 Second attempt: Ta$_2$O$_5$/SiO$_2$ Based Top Mirror

The first fabrication attempt using a-Si/SiO$_2$-based top mirror encountered some challenges with respect to the buckling yield as mentioned above, and also with respect to limiting the options for the optical pumping of the embedded SiO:Er layer (as discussed below). To overcome these issues, we attempted a second fabrication run which is briefly described below, and summarized by the process flow shown in Figure 4.5.
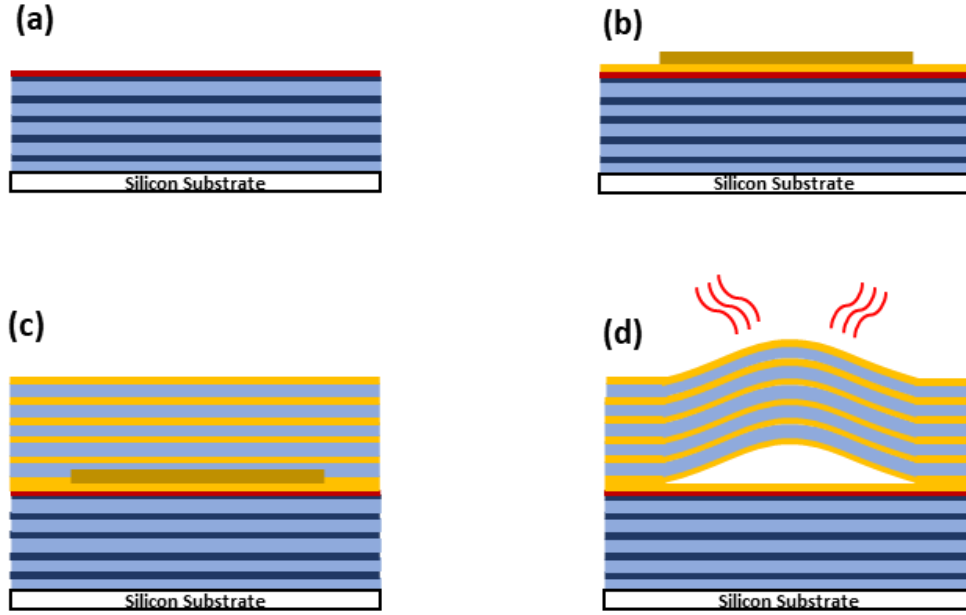
Figure 4.5. Process for embedding an SiO:Er layer inside buckled dome cavities with a hybrid mirrors approach. (a) A thin (10 nm) layer of a-Si followed by the active (~100 nm) layer of SiO:Er were deposited on the top of the 4.5-period a-Si/SiO$_2$ lower Bragg mirror. The wafer was then annealed to activate the SiO:Er layer (see main text). (b) A thin (~20 nm) layer of Ta$_2$O$_5$ was then deposited, followed by deposition and patterning (by liftoff) of the low-adhesion fluorocarbon layer. (c) A 5.5-period Ta$_2$O$_5$-based top Bragg mirror was finally deposited. (d) Heating is applied to the sample to induce delamination buckling over the fluorocarbon features and produce the buckled dome cavities.

In the first step, a 4.5-period a-Si/SiO$_2$ Bragg mirror (starting with a low refractive index SiO$_2$ layer) was deposited on a cleaned, double-side-polished silicon wafer. In this case, the bottom mirror was ended with a thin (~10 nm) layer of a-Si motivated by a desire to increase the buckling yield. Figure 4.6(a) shows the VASE-measured reflectance for the bottom mirror compared with reflectance predicted by a transfer-matrix simulation. Previous work by our group [139] had established that the a-Si/fluorocarbon interface results in a very high yield of buckling delamination, in contrast to the SiO$_2$/fluorocarbon interface used in the first fabrication run. However, a subsequent decision was made to use an un-patterned SiO:Er layer for this attempt, so that the inclusion of this thin a-Si layer was ultimately not particularly relevant here.

On top of the bottom mirror, a thin (~ 100 nm) layer of erbium-doped silicon monoxide (SiO:Er) was deposited as the active emitting layer (using the same procedures that were described in Ref. [131]). The wafer was subsequently diced into 4 quarters (~ 3x3 cm^2) and the quarter wafers were subsequently annealed under the same conditions as described above (500 °C for 1 hour using

forming gas) to activate the SiO:Er layer. As mentioned above, it was decided to avoid patterning of the active layer into 'pads' for this attempt, in order to remove challenges with respect to alignment between the pads and the dome cavities, and also because it was speculated that attempting to form delamination buckles over non-planar features ~100 nm thick might result in poor yield.
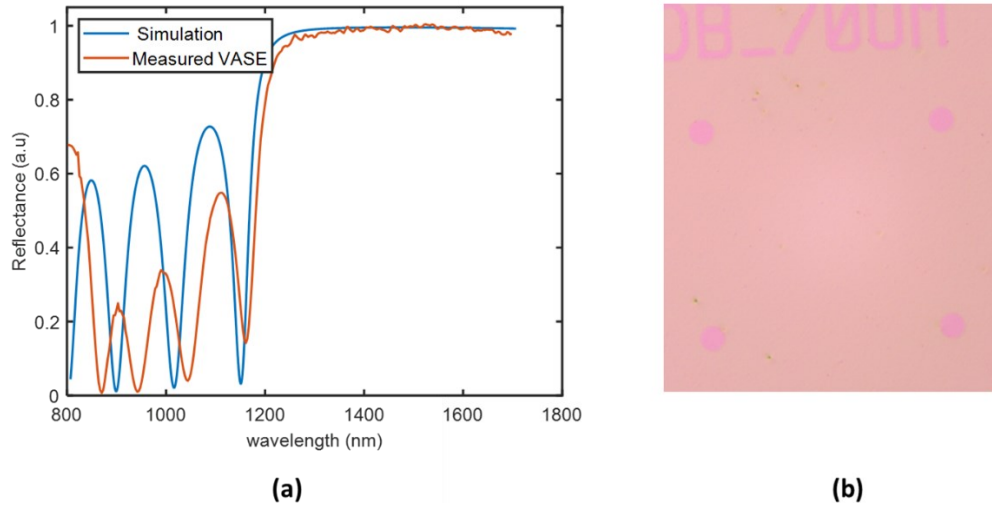
Figure 4.6. (a)VASE measured reflectance of a 4.5-period SiO_2/a-Si mirror capped by a thin layer of SiO:Er, along with the reflectance predicted by a transfer matrix simulation. (b) Fluorocarbon features patterned as 70 μm circles.

Three-quarters of the wafer were next put back into the sputtering system, and one quarter was saved in order to keep it as a reference for PL measurement. A thin (~20 nm) layer of Ta_2O_5 was sputtered on top of the active layer, The Ta_2O_5/fluorocarbon interface, similar to the a-Si/fluorocarbon interface, has been shown in previous work to produce a high yield of buckled features [139]. Next, AZ1512 photoresist was spun-cast in order to pattern a low-adhesion fluorocarbon layer. Using the Oxford Plasma Pro Estrelas 100 system at the nanoFAB, a thin Teflon-like layer was deposited using the passivation cycle of the DRIE Bosch process. The photoresist was lifted off by sonicating the wafer in acetone for 1 hour and followed by cleaning with IPA and DI water, and drying with N_2 (seen Figure 4.6(b)). On this wafer, a variety of device sizes (i.e., dome base diameters), including 30,40, 50, 60, and 70 μm, were included.

In choosing the number of periods for the top mirror, it was necessary to strike a balance between optical properties on the one hand, and the optimal mirror thickness to achieve good buckling results on the other hand. Figure 4.7(a) shows a transfer-matrix simulation for a planar

cavity with a zero-thickness air layer between the mirrors, and assuming a top mirror with 5.5 periods. Note that a resonant cavity mode is predicted at a wavelength of ~1500 nm. However, the Q-factor is fairly low (~240), and the peak transmission is also low, due to the fact that the cavity is relatively imbalanced (i.e., the 4.5-period a-Si/SiO$_2$ mirror is significantly more reflective than the 5.5-period Ta$_2$O$_5$/SiO$_2$ mirror). Nevertheless, we chose this combination due to considerations of a typical thickness for the top mirror that had historically tended to result in successful buckling. Thus, a 5.5-period Ta$_2$O$_5$/SiO$_2$ Bragg reflector was deposited on the top of the patterned low adhesion layer (LAL) for three quarters only. This top mirror was deposited at slightly different chamber pressure and with slightly different deposition rates for SiO$_2$ and Ta$_2$O$_5$ as compared to that described previously [139,140]. This was motivated by the fact that the stress measured for these films had been observed to be lower than historical values. The optical properties of the films, determined from the ellipsometry measurements, were found to be n_{Ta2O5} ≈ 2.1 and n_{SiO2} ≈ 1.47, respectively, and an extinction coefficient of κ_{Ta2O5} ≈ 1 × 10^{-1} and κ_{SiO2} ≈ 2× 10^{-3} at 1550 nm for Ta$_2$O$_5$ and SiO$_2$, respectively, was estimated. This mirror was also nominally centered at 1550 nm with a thickness of d_H ~183 nm, and d_L ~264 nm for the high- and low-index layers, respectively. The total thickness of the top mirror, in this case, is ~ 2 μm.
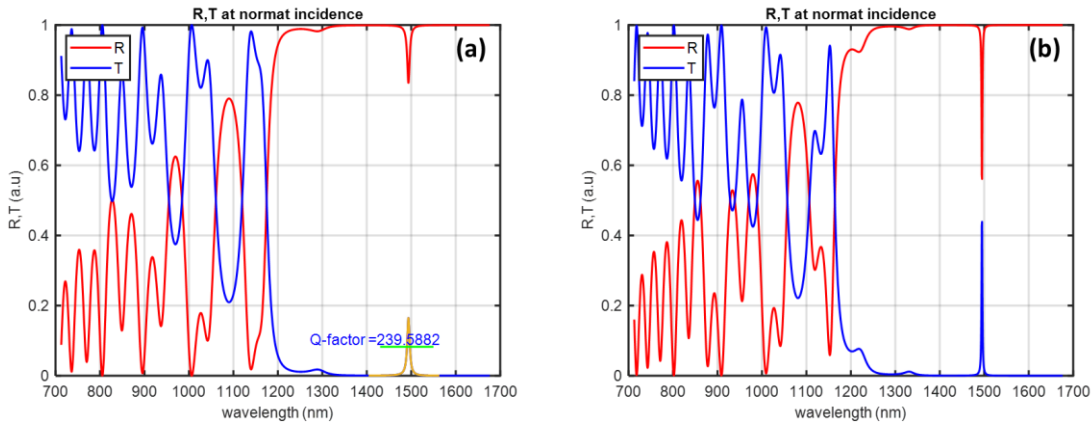
Figure 4.7. (a) Transfer-matrix simulations of a planar cavity with a 100 nm thick SiO:Er layer and a 5.5-period Ta$_2$O$_5$-based top mirror, for example as depicted in Fig. 4.5(c). (b) Transfer-matrix simulations for the same planar cavity but with a 7.5-period Ta$_2$O$_5$- based top mirror.

Vase measurements were performed for the completed structure with 5.5-period upper mirror, and also for chips with a 7.5-period upper mirror. As discussed below, these latter samples were

realized either by addition of two additional periods to the 5.5-period samples, or in one case by depositing a 7.5-period mirror in a single sputtering run onto the quarter wafer previously set aside as a reference. Representative reflectance results are shown for each of these cases in Figure 4.8.
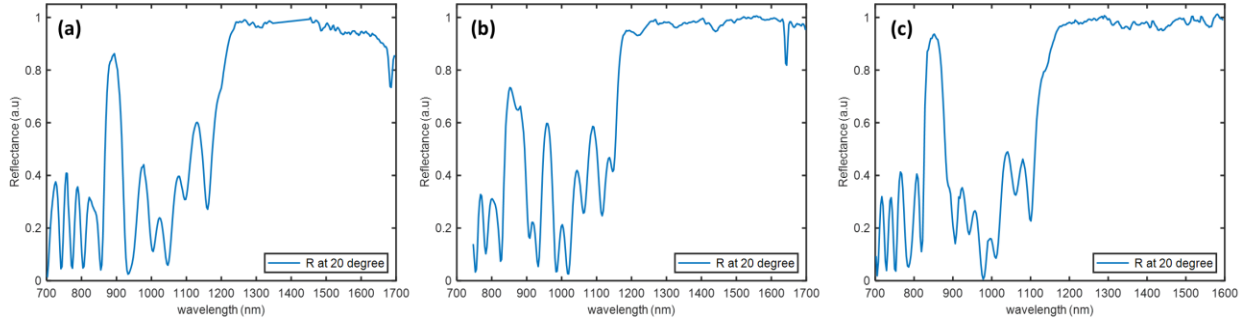
Figure 4.8. VASE-measured reflectance of a planar region of the completed structure (i.e. bottom mirror followed by SiO:Er layer followed by the upper mirror, and for: (a) the original sample with 5.5-period top mirror. (b) A chip with a 7.5-period top mirror, realized by addition of 2 periods to the original sample. (c) A sample with 7.5-period top mirror deposited in a single sputtering run, using the quarter wafer that had initially been set aside as a reference. Note that this mirror had a 'cloudy' appearance after deposition (see main text), but the measured reflectance for the completed structures is nevertheless quite similar in parts (b) and (c).

In the last step, two quarters of the wafer with the 5.5-period upper mirror were subsequently diced into ~ 1.5 cm x 2 cm chips (each chip has four cells and every cell has ~ 900 domes) and prepared for buckling. Two methods were attempted to induce buckling; chips were either placed on a hot plate or in a rapid thermal annealing (RTA) system. Some of the chips were placed on the hot plate initially set at 100 °C, and the temperature was raised up to a maximum of ~350 °C with a ramp rate of ~50 °C/ min. Likely as a result of the uneven distribution of temperature on the surface of the hot plate, and also due to the variety of dome sizes in this chip (30 µm, 40 µm, 50 µm, 60 um, 70 µm, 100 µm and 150 µm), some of the dome features popped off while others failed to buckle. In an effort to address this problem, we used RTA (rapid thermal annealing) to attempt buckling on some of the other chips. The RTA temperature was set to 400 °C for 10 sec, and a representative result is shown in Figure 4.9(a) and (b). Unfortunately, the yield of good devices (~ 20 %) was found to be relatively low using this method. In fact, the hot plate was found to produce the best yields, and we decided to use that method for all remaining attempts.

As mentioned above, we initially chose a 5.5-period upper mirror because we believed it was an appropriate thickness to yield good buckling results. However, subsequent optical experiments

(see below) revealed that the resultant dome cavities did not exhibit good optical mode structure or high-quality modes. In an attempt to improve the optical properties, two additional periods of Ta_2O_5/SiO_2 were added to several of the chips. As seen in Figure 4.7(b), this addition could in principle improve the symmetry of the cavities (as evidenced by the higher peak transmission of the resonant mode) and increase the Q-factor of the resultant cavities. However, it should be noted that sputtering a mirror in two steps (i.e., breaking vacuum between the first and second parts of the deposition) is not typically a good approach to achieve the highest quality mirrors.
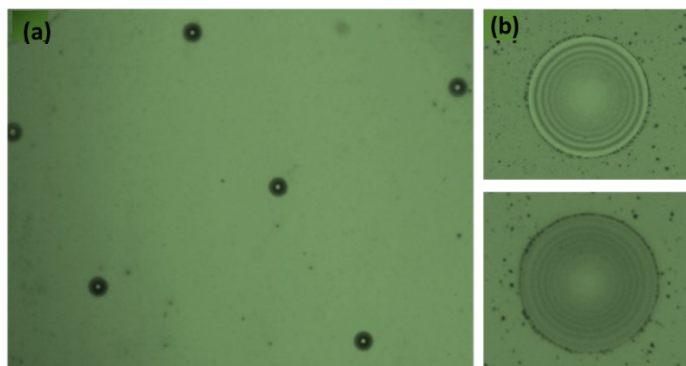
Figure 4.9. Microscope images for buckled dome cavities on a sample where buckling was induced by heating in the RTA system. (a) An array of buckled domes, (b) Higher magnification image of two buckled domes; the interference fringes provide evidence of a high degree of cylindrical symmetry.

On these chips, which were buckled before the addition of the extra mirror periods, ~ 70 % of the domes with base diameters of 60 μm and 70 μm, and ~10 % of the domes with 50 μm base diameter, were found successfully buckled, while all of the 100 μm and 150 μm domes failed due to 'pop off' of the upper mirror. As mentioned above, it is likely that each size of dome has a unique temperature profile (i.e., an optimal temperature ramp rate and peak temperature) needed to induce an optimal buckling result. For example, 50 μm diameter domes have been observed to need a longer time with a higher temperature of around 400 °C to induce buckling. In the future, it might be a good idea to ensure each chip contains only one or two different sizes of domes (e.g., 60 μm and 70 μm), so that an optimal buckling routine can be applied. This might lead to a higher yield of successfully buckled domes, and reduce the frequency of 'pop off' or unbuckled domes.

In spite of the reasonably good buckling yields mentioned above, subsequent optical scans revealed that only a small number of the buckled domes exhibited a cavity resonance overlapping with the Er emission band in the ~ 1520 – 1560 nm wavelength range. As one final attempt, we

decided to deposit a 7.5-period mirror (i.e., in one sputtering run) on the remaining quarter wafer that we had initially kept as a reference for PL measurements (see above). As above, a thin layer of Ta_2O_5 was first deposited, followed by a patterned fluorocarbon layer, and finally followed by a 7.5-period Ta_2O_5/SiO_2 mirror nominally centered at 1550 nm wavelength. This sample was patterned to include three groups (domes of 50 µm, 60 µm, and 70 µm base diameter), and with each group comprising ~ 4000 domes. This range of dome sizes, as mentioned above, had produced good buckling (moderate yield) compared to domes of smaller base diameter (e.g., 30 µm and 40 µm). Unfortunately, and for reasons that are not completely known, the mirror became cloudy on the day following deposition (see Figure 4.10(a)). We speculated that this might have been due to the shared-use nature of the Doug sputtering chamber; the chamber might have been contaminated with other materials on the day of our mirror deposition. In spite of this issue, the rest of the process to induce buckling was carried out as planned, using a hot-plate baking procedure similar to that described above. As shown in Figure 4.10(b) and (c), this resulted in a significant variation in the heights of buckled domes and a relatively low yield (~30%), with many domes 'popped-off' or delaminating outside the circular patterned region of the fluorocarbon layer. Nevertheless, a few promising domes were identified from optical scans (see, for example, Figure 4.10(d)), as discussed further in Section 4.3.2.
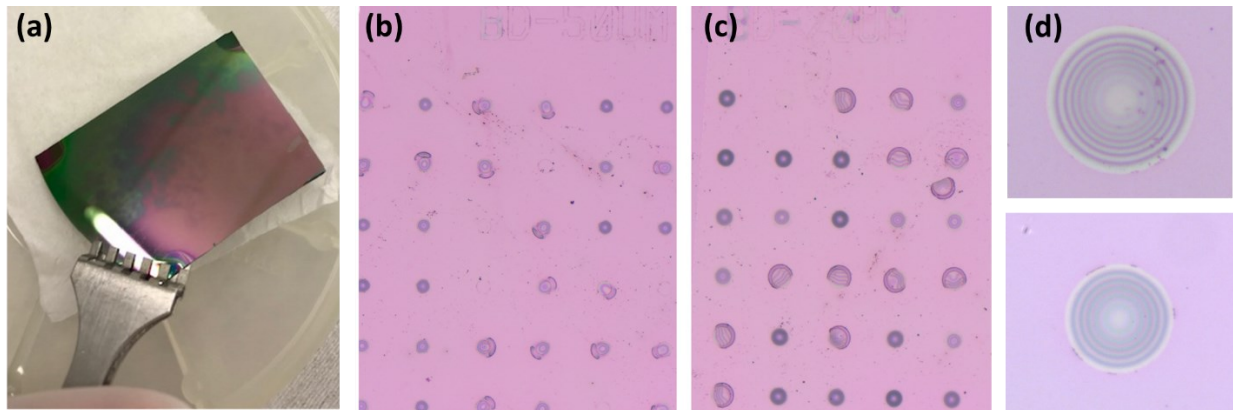
Figure 4.10. (a) Camera image showing the 'cloudy' appearance of the 7.5-period upper mirror deposited on the final quarter of the hybrid mirror wafer (see main text). (b,c) Microscope images for domes of 50 µm and 70 µm base diameter, showing that many of the domes 'popped off' or buckled outside the intended region during the heating step used to induce buckling. (d) Microscope images of two promising domes (with base diameter of 70 µm (upper) and 50 µm (lower).

4.3 Optical characterization of dome cavities with embedded SiO:Er layers

To investigate the resonant modes of the buckled dome cavities, we constructed a home-built optical microscope setup. A schematic of the experimental setup is shown in Figure 4.11. A tunable laser (Santec TSL-710, 1480 nm-1640 nm operational range), which varies wavelength and power, is coupled to a single-mode fiber (SMF) and is used to perform the transmission measurements. The laser beam propagates through a broadband reflective collimator (Thorlabs RC02FC-P01) which was connected to a 20x microscope objective lens (NA=0.4), and both (the fibre collimator and objective) were attached to a tilt/tip stage, in addition to an XYZ translation stage for alignment purposes. The laser beam was focused to a minimum spot size of ~ 3.5 µm. The chip was placed on a custom aluminum plate having a small circular window to provide light access. The plate was also mounted on an XYZ translation stage, to enable moving it within the optical path and align regions of interest on the chip. Light transmitted through a cavity was collected using long-working-distance, infinity-corrected microscope objectives (ZEISS). The latter is attached to a rotating turret to permit us to change the magnification from low to high. The light collected by the objective is passed through a dichroic mirror (950 nm cut-on wavelength, Thorlabs DMLP950R) to a 90:10 (at 1550 nm wavelength) unpolarized beam splitter (Thorlabs BS030 mounted in Thorlabs CCM1-4ER.). Most (~ 90 %) of the light is guided to the spectrometer/detector through a large beam collimator (Thorlabs F810FC-1550), while the rest (~10 %) of the light is passed through tube lenses to adjust the imaging of the sample to a near-infrared camera (Raptor Photonics Ninox, NX1.7-VS-CL-640), which also works as a power detector in our setup. The camera utilizes an InGaAs-based sensor with 15 µm pixel pitch and 640 x 512 pixels.
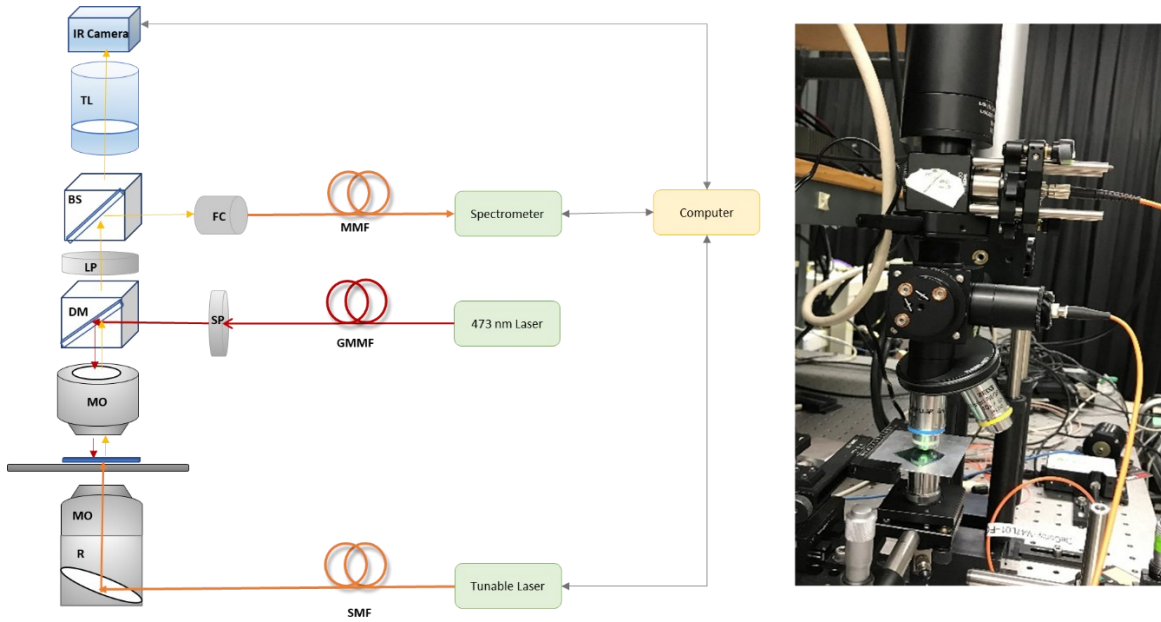
Figure 4.11. (a) Schematic diagram of the experimental setup. The symbols indicate TL (Tube lens), BS (Beam Splitter), DM (Dichroic Mirror), LP (Long Pass Filter), MO (Microscope Objective lens), FC (Fiber Collimator), MMF (Multimode Fiber), GMMF (Grad Multimode Fiber), SMF (Single Mode Fiber), R (Broadband Reflective Collimator) and SP (Short Pass Filter). (b) Photograph of the homemade confocal microscope setup used in measurements.

4.3.1 Optical measurement results for Silicon-based top mirror

Due to the relatively low yield discussed in Section 4.2.1.1, we had only 17 devices to measure and test from the wafer with the a-Si-based upper mirror. Using the microscope setup shown in Figure 4.11, the optical properties for microcavities with base diameters of 60 μm (7 devices) and 70 μm (10 devices) were studied. Light from the tunable laser was coupled into the cavities via a 20x microscope objective lens. By tuning the laser, the fundamental and higher-order optical mode-field intensity patterns were captured and imaged by the camera. Using the transmission spectra, the linewidth of the fundamental mode (defined here as the full-width at half-maximum (FWHM)) was extracted and used to estimate the Q-factor. A representative scan is shown in Figure 4.12(a) (for a 70 μm base-diameter cavity with peak height ~1.8 μm estimated from profilometer measurements), and with an input laser power of -14 dBm. The linewidth was estimated to be ~ 0.3 nm, corresponding to a Q-factor ~ 5050. The effective cavity finesse follows as $\mathcal{F} = Q/m \approx 1700$, where m = 3 is the longitudinal mode order for peak buckle height ~ 1.8 μm (see Figure 4.13 below). This is similar to finesse values reported in previous work by our

74

group [1,83], indicating that the embedded SiO:Er pad did not significantly degrade the optical properties of the cavity in this case.
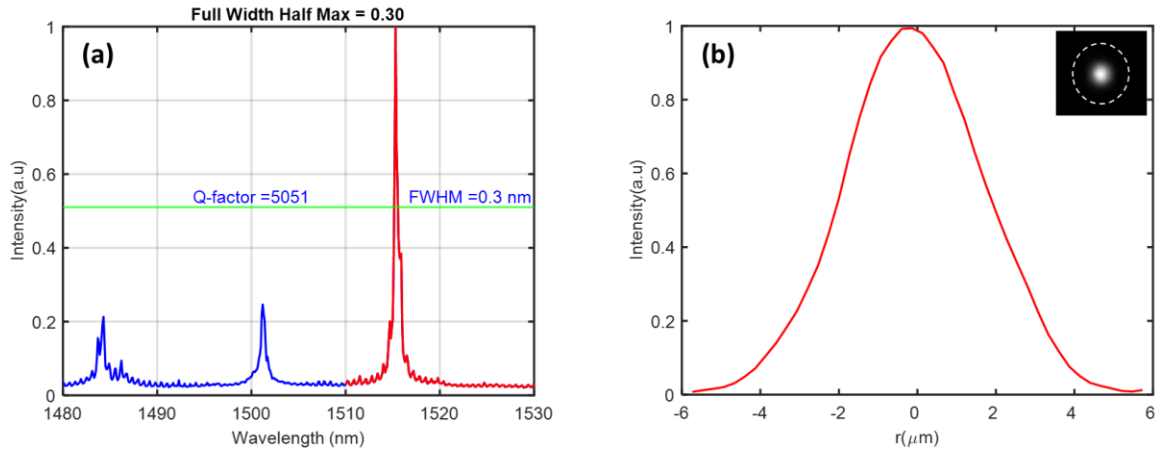
Figure 4.12. (a) A transmission scan for a buckled dome with a 70 μm base diameter, and with an embedded ~ 40 nm thick SiO:Er pad. The *Q*-factor was estimated from the FWHM linewidth of ~ 0.3 nm. (b) The cross-sectional profile for the fundamental mode- field intensity (with the laser tuned to ~ 1515 nm wavelength) is plotted, as extracted from the camera image shown in the inset.
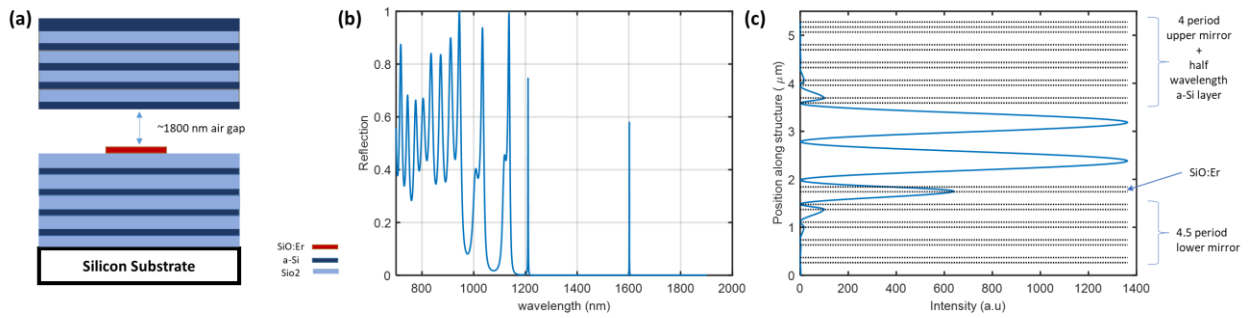
Figure 4.13. (a) A planar representation of the cavity from Fig. 4.12, with an air gap of 1800 nm. The bottom mirror is ended by a low-index (SiO2) quarter-wave layer followed by 40 nm of SiO:Er. (b) Transfer matrix simulation of the transmission for the planar structure in part a. (c) Transfer matrix simulation of the electric field intensity (i.e., $E \cdot E^* = |E|^2$) at the wavelength of the resonant mode (~1602 nm) from part (b).

Optical scans were attempted for both sets of successfully buckled domes mentioned above (i.e., with 60 μm and 70 μm base diameter), and the results are summarized in Table 4.2. In addition to the low yield mentioned, this fabrication run resulted in a much greater variation in buckle heights compared to our historical results [83]. The reasons for this are not entirely clear, although we speculated that it could be attributed to the high adhesion of the fluorocarbon/ SiO interface mentioned above, which likely results in buckles forming at relatively random and

unpredictable times during the heating step. In any case, only a few domes had the appropriate height to support optical modes in the ~1550 nm wavelength range of interest.

One of the best devices had a base diameter of 70 µm, peak height ~ 1.8 µm, and an embedded SiO:Er pad with a diameter of 10 µm; detailed results for this particular cavity are shown in Figure 4.14. An optical profilometer (Zygo) was used to determine the cross-sectional profile and this was compared to the profile predicted by elastic buckling theory (see Section 2.6). The good agreement shown indicates that the inclusion of the thin (~40 nm thick) SiO:Er pad did not dramatically affect the buckling shape. Note that the ZYGO data seems to suggest that the SiO:Er pad is adhered to the top of the buckle, but this is an artifact of the optical interference technique used to extract surface profiles from this instrument. Figure 4.14(c) shows the transmission scan along with the mode-field intensity profiles that were obtained and captured using the camera as a detector. It is worth noting that the transverse mode spacing (~17 nm) and the spot size (radius) of the fundamental mode (~ 3.7 µm) are in good agreement with the predictions of theory from Chapter 2.
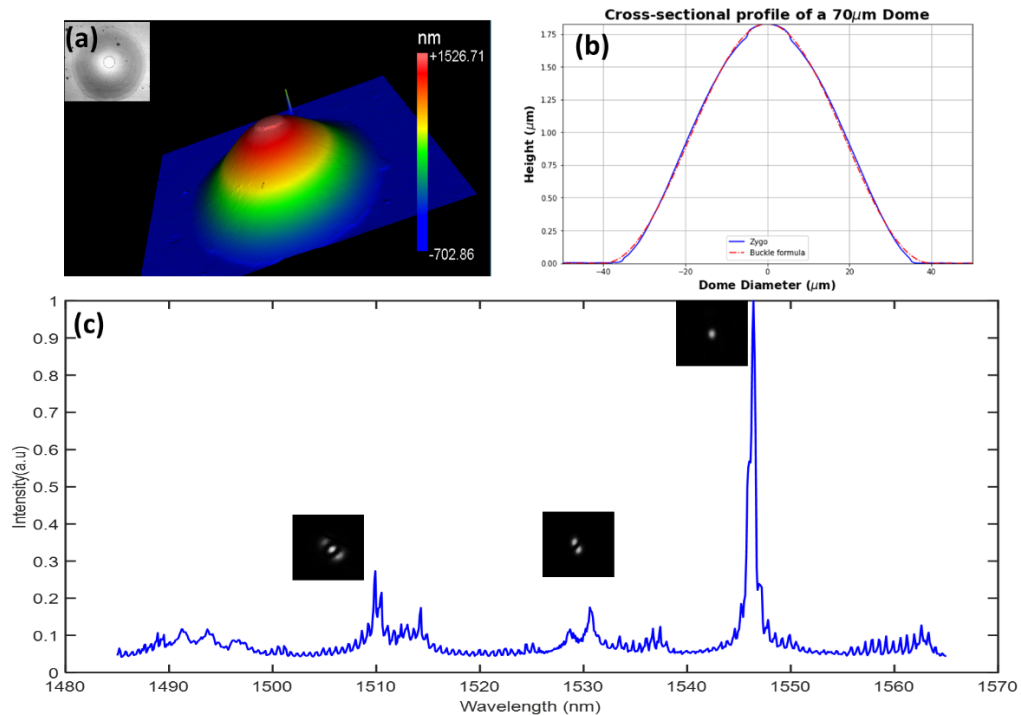
Figure 4.14. (a) Surface relief plot and microscope image (inset) for a buckled dome microcavity (70 µm base diameter) with an embedded SiO:Er 'pad' (diameter ~ 10 µm). (b) The cross-sectional profile of the 70 µm dome was measured using an optical profilometer (Zygo). (c) Spectral transmission scan for the dome from part a. The inset presents camera images of the mode-field intensity profile for various higher-order modes and the fundamental mode, captured at the adjacent resonant wavelength in each case.

We attempted to excite PL from the embedded SiO:Er pad, hoping to observe spatial and spectral signatures of cavity-modified emission. We first tried to pump Er^{+3} ions through direct excitation using 800 nm and 980 nm lasers, since the upper mirror of the cavity is relatively transparent at these wavelengths. However, we were not able to observe emission, likely in part due to the limited sensitivity of our available spectrometers (Ocean Optics NIRquest and NIRflame, hand-held spectrometers). We subsequently attempted to pump these cavities by shorter wavelength lasers to take advantage of the high-cross-section, host-mediated excitation process [131] discussed in Section 4.2, but again we observed no emission. In addition to low sensitivity in our spectrometers, transfer-matrix simulations confirmed that most of the energy from shorter wavelength pump lasers (e.g., $\lambda_0 < 800$ nm) is absorbed by the a-Si layers in the top mirror of these samples. In order to check if the 40 nm thick SiO:Er layer remained active after the complete buckling process, one of the 'popped-off' domes was pumped using a 473 nm blue laser through indirect excitation. Even in this case, unfortunately, we did not observe any luminescence. While this could possibly be attributed to the limited sensitivity of our experimental setup, it was also possible that the 40 nm thick SiO:Er layer was degraded as a result of the subsequent fabrication procedures. To check this theory, the emission from a 40 nm thick SiO:Er film on the glass slide was examined by pumping the layer with high power (~30 mW). An emission spectrum was obtained using the Ocean Optics NIRFlame spectrometer with an integration time of 10 seconds and no averaging, as seen in Figure 4.15. This provided some further support that the fabrication process used had possibly degraded the embedded SiO:Er layer. In any case, the lack of success with these experiments motivated the second fabrication attempt discussed in Section 4.2.1.2, in which we replaced the a-Si-based mirror with a Ta_2O_5-based mirror to enable more pumping options, and used a thicker (~100 nm) and un-patterned SiO:Er layer to increase the potential luminescence signal.
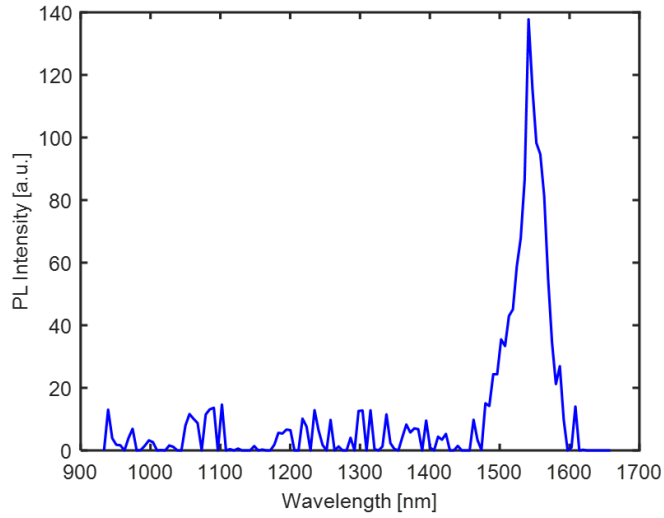
Figure 4.15. PL spectra observed from 40 nm thickness of the SiO:Er on a glass slide.

Table 4.2. Measured Properties for Buckled Dome Microcavities with a-Si-based Top Mirror.

Dome size (μm)	ZYGO $\delta\ \mu m$	Measured λo (nm)	Measured FWHM (nm)	Measured Q-Factor
60	1.16	1633	0.8	2041
	1.08	1567	0.7	2234
	0.4	No mode observed		
	1.34	Higher order		
	1.43	Higher order		
	0.58	Could not distinguish modes		
	0.46	Could not distinguish modes		
70	1.99	1633	0.5	3260
	1.99	1630	0.4	4077
	0.64	Could not distinguish modes		
	3.06	1592	0.3	5305
	1.12	1579	0.8	1975
	1.76	Could not distinguish modes		
	1.9	1594	0.3	5305
	1.8	1517	0.3	5050
	2	Higher-order mode		
	1.82	1548	0.7	2209

4.3.2 Optical measurement results for cavities with a Ta₂O₅ -based top mirror.

As discussed in Section 4.2.1.2, chips having either 5.5- or 7.5- period upper mirrors were fabricated on the hybrid mirror wafer. Initially, buckled devices from the 5.5-period chips were identified and scanned using the same microscope setup described above. In an attempt to identify devices whose fundamental resonance overlaps with the erbium emission band, thousands of devices were scanned using the tunable laser and the infrared camera. However, none of these scans indicated cavities with high-quality HG/LG modes. Rather, it was typically difficult to identify clear signatures of individual LG/HG modes, as shown for example in Figure 4.16. We speculated that this was attributable to the relatively low reflectance of the 5.5-period mirror (see Sec. 4.2.1.2) and the typically poor shape of the buckled cavities on these chips. Profilometer scans (not shown) revealed that these cavities typically had low height and a relatively low curvature for the buckled mirror curvature. Taken together, these factors would result in low-Q optical modes with a tendency to be overlapping spectrally, and thus difficult to isolate experimentally.
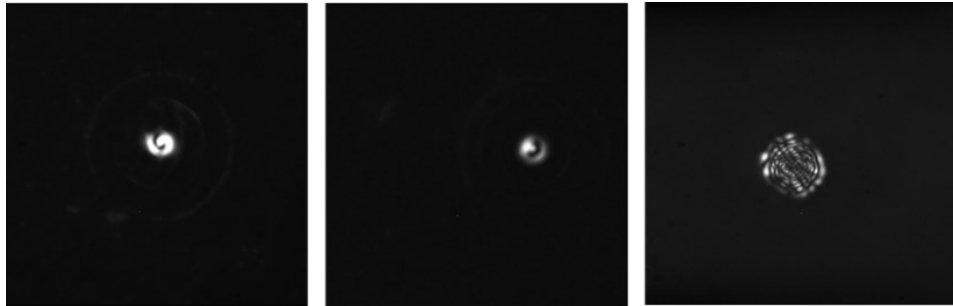
Figure 4.16. Captured camera images for possible optical modes for buckled cavities with a 5.5-period Ta₂O₅-based top mirror. The intensity patterns did not resemble isolated HG/LG modes, but rather are likely the result of multiple spectrally overlapping, low-Q modes.

Subsequently, as discussed in Section 4.2.1.2, two extra mirror periods were added on four of the chips, in an attempt to increase the cavity Q-factor and improve the optical mode properties. These chips contained a few buckled domes of base diameters 30 μm and 40 μm, although the yield was low (~ 30%), and microscope images (see Figure 4.17(a) and (b)) suggested that these domes had low height. Very few of these domes were found to support any resonance in the 1520 –1560 nm wavelength range that overlaps with the erbium emission band. The transmission for

one of the best 40 µm cavities is shown in Figure 4.18(a); this dome has a fundamental resonance (at ~ 1597 nm) outside the primary range of the erbium emission.
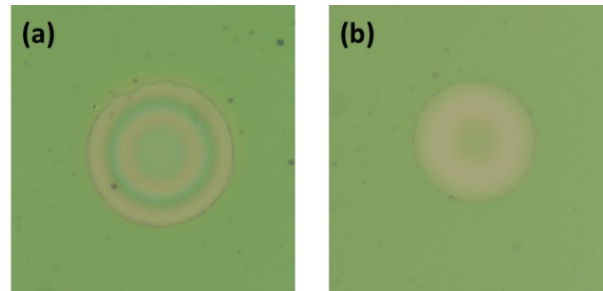
Figure 4.17. Microscope images for buckled domes with (a) 40 µm and (b) 30 µm base diameters. The interference fringes suggest a high degree of cylindrical symmetry, but a relatively low profile (i.e., the peak height of the domes is small).

Several of these smaller domes looked to have promising spectra, but with their fundamental resonance lying at a wavelength above ~1600 nm and thus outside the erbium emission band of interest. In an attempt to shift this resonance to lie within the erbium band, we tried to adjust the fundamental resonance (i.e., to shrink the height of the cavity) by annealing the sample. That was done by following the same procedure as described in Ref. [81], which studied the effect of annealing on the residual stress for an a-Si/SiO$_2$ mirror. In our case, we applied it on the samples with a Ta$_2$O$_5$/SiO$_2$ upper mirror. Tests were carried out on a chip containing 40 µm base-diameter buckled domes. Initially, the sample was placed on the hot plate and the temperature was raised to 50 °C at a ramp rate of 15 °C/min. The sample was then allowed to cool slowly back down to room temperature. However, the resonance did not show a shift after this procedure. The process was next repeated with a higher end-point temperature of 100 °C at a ramp rate of 15 °C/min. After this procedure, the resonance showed a noticeable shift. In an effort to increase the shift, these steps were repeated 2 times and with the temperature raised to 150 °C at a ramp rate of 15 °C/min, as shown in Figure 4.18(b). After the third run, the process did not show any additional shift, so we decided to stop the process.
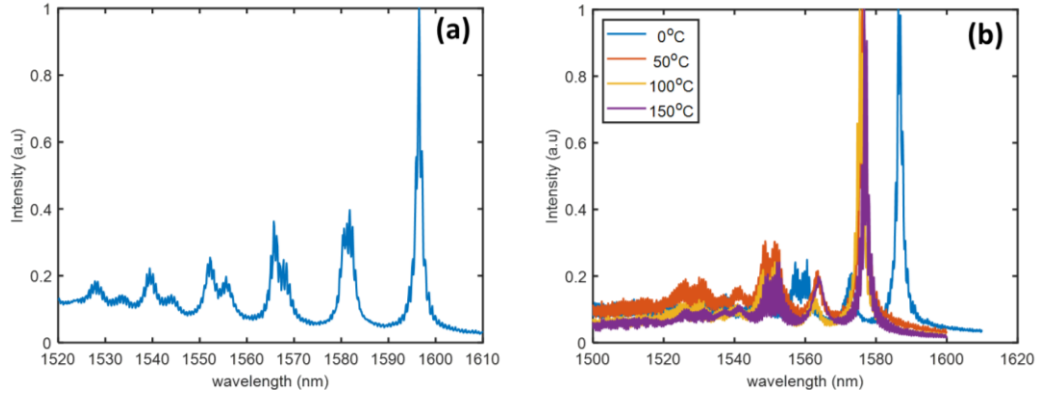
Figure 4.18. (a) Transmission scan for a 40 µm base-diameter dome from one of the chips which had 2 mirror periods added. (b) Plots showing shifts in the resonance spectrum induced by annealing the sample on a hot plate at different temperatures (see main text).

It is important to note that the effective cavity length includes the air gap (approximately given by the peak buckle height) plus the optical thickness of the $\lambda/4$-thick SiO_2 capping layer, plus the optical thickness of the SiO:Er layer, plus the field penetration depth of the Bragg mirrors. Figure 4.19(a) shows a schematic planar representation of the layer structure, assuming a 1.8 mm air gap, Figure 4.19(b) shows the predicted transmission through this structure from a planar transfer matrix model, and Figure 4.19(c) is the electric field profile at the wavelength of the resonant mode (~1667 nm) from part (b). Note that this can be viewed as a 3rd-order ($m = 3$) longitudinal resonance, by considering the first high-index layer (i.e., adjacent to the cavity) as the mirror boundary for both the upper and lower mirrors.
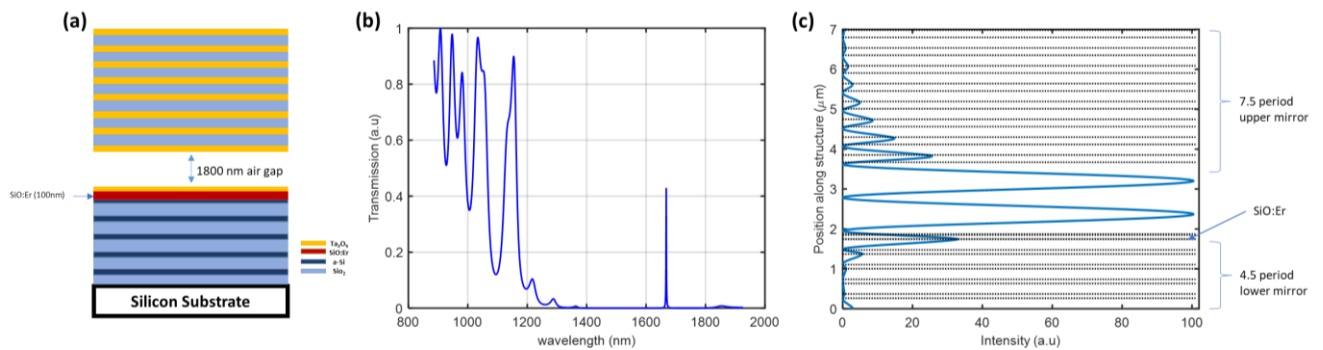
Figure 4.19. (a) A planar structure for our cavity with air gap of 1800 nm. The bottom mirror is ended by a low-index (SiO_2) quarter-wave layer followed by 10 nm of a-Si, 100 nm of SiO:Er, and finally a 20 nm thin layer of Ta_2O_5. (b) Transfer matrix simulation of the transmission for the planar structure in part a. (c) Transfer matrix simulation of the electric field intensity (i.e., $E \cdot E^* = |E|^2$) at the wavelength of the resonant mode (~1667 nm) from part (b). The SiO:Er layer is centered on a field anti-node, although the peak electric field intensity is only lower at this position (by a factor of ~ 0.34) relative to the peak field intensity in the air gap layer.

Finally, we consider results for the last quarter of the wafer, which had its 7.5-period upper mirror deposited in a single sputtering run. As mentioned in Section 4.2.1.2, this sample appeared somewhat 'cloudy' after the top-mirror deposition. Nevertheless, from VASE measurements (see Figure 4.8(c)), the sample exhibited good reflectivity and the expected signatures of a stop band in the wavelength range of interest. As shown above (see Figure 4.10), the buckling of this chip produced a reasonable yield of intact dome cavities. Transmission scans were performed using the microscope setup, and some typical results are shown in Figure 4.20. As for all of the devices from the 'hybrid' wafer (i.e., with the silicon-based upper mirror and Ta_2O_5-based upper mirror), the transmission scans did not suggest the existence of high-quality optical modes. For example, all of the transmission scans exhibit high-frequency ripples due to substrate reflections, and the small spacing of the HG/LG transverse modes (i.e., compared to Figure 4.12 for example) suggests that these buckles have relatively small curvature for their buckled mirrors. Nevertheless, the cross-sectional profile of some domes showed a good fit to the profile predicted by elastic buckling theory (see Figure 4.21(b and c)). Thus, the poor optical properties of these domes can most likely be attributed to sub-optimal mirror reflectance, probably in particular for the Ta_2O_5/SiO_2 upper mirror. This in turn might have partly been due to lack of care in wafer cleaning and handling, which might have introduced debris and particulates (visible in most of the microscope and Zygo images here), and which in turn likely caused large optical scattering losses. It is also possible that the 'cloudy' appearance of this sample after sputtering of the upper mirror (the cause of which was not determined) was a visual indication of high-loss optical films. Notably, and as evident in Figure 4.20, it was found that the quality of the lower order modes was worse for cavities with a fundamental mode below ~ 1600 nm (i.e., compare Figure 4.20 (b) and (c) to Figure 4.20(a)). This likely indicates that the reflectance of the upper mirror was lower at these shorter wavelengths, which was unfortunate given the goal was to align a fundamental cavity mode with the main part of the Er emission band lying in the ~1520-1560 nm wavelength range.
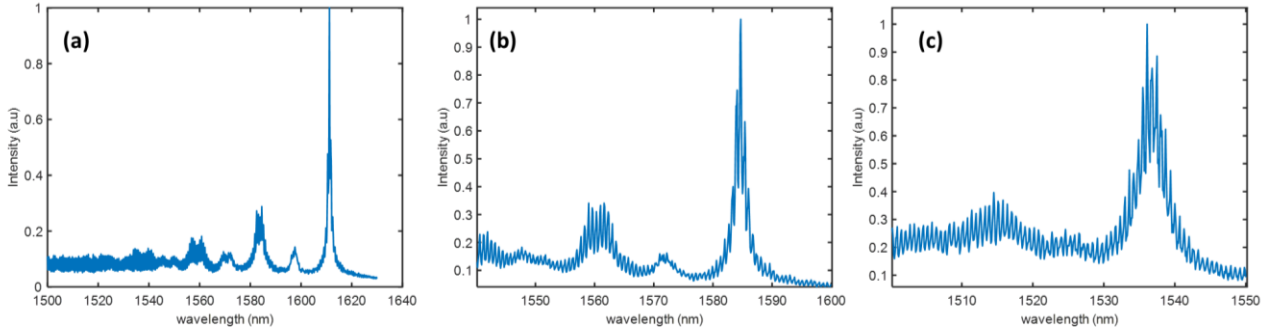
Figure 4.20. Representative scans for 50 µm base-diameter dome cavities from the 'cloudy' chip with a 7.5-period upper mirror. (a) A device with its fundamental resonance at 1611 nm. (b) A device with its fundamental resonance at 1584 nm. (c) A device with its fundamental resonance at 1536 nm.
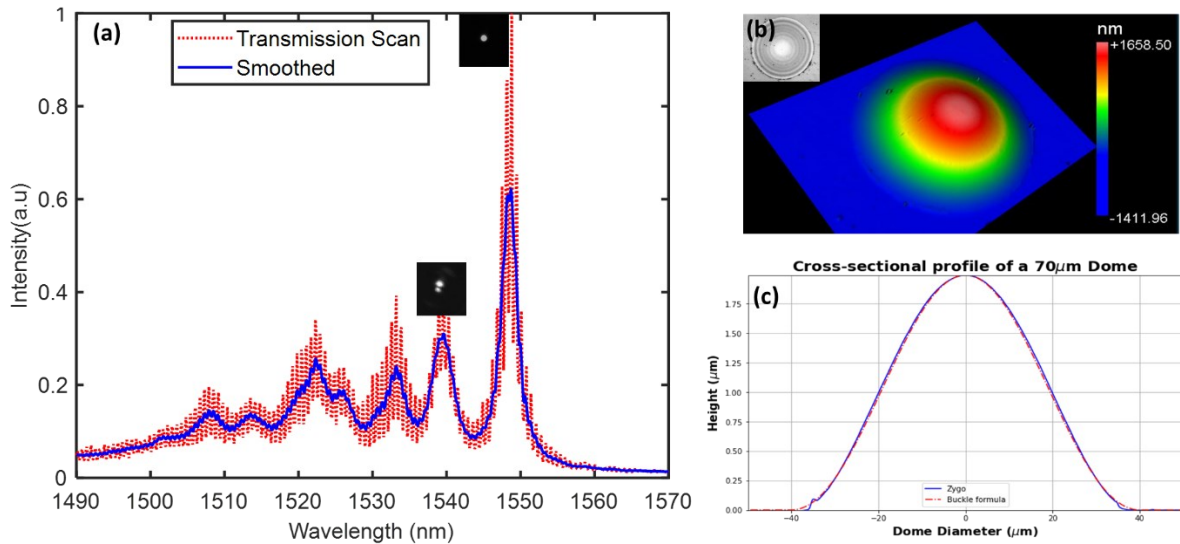
Figure 4.21. (a) Transmission scan for a dome with 70 µm base diameter, from the 'cloudy' chip with the 7.5-period upper mirror deposited in a single sputtering run. (b) Surface relief plot for the dome measured in part a. (c) Cross-sectional profile for the dome in part b, showing a peak cavity height of ~1.8 µm, and a good fit to the profile predicted by elastic buckling theory.

In spite of the sub-optimal optical properties of these cavities, we nevertheless proceeded with room-temperature photoluminescence (PL) measurements using the same home-built microscopy system described above (see Figure 4.11). A blue laser (473 nm wavelength, peak power ~ 30 mW) was used for excitation. It was coupled into the microscope system via a graded-index multimode fiber and a collimator (Thorlabs F950FC-A, 350-700 nm), and the collimated beam was passed through a short pass (Thorlabs FESH0950) filter. PL detection was carried out with a spectrometer and Raptor NIR camera. The excitation laser was focused onto the sample using an

infinity-corrected objective lens with 50x magnification (with a numerical aperture of 0.85). The PL was collected by the same objective lens, and pass through the dichroic mirror (Thorlabs DML950) and the long-pass filter (Thorlabs FELH 1450) to further suppress residual scattered light from the blue pump laser. The collimated beam inside the microscope tube is incident onto a beam splitter (90:10 R:T, Thorlabs BS030). The output of the 90% port is collected by the large beam collimator (Thorlabs F810FC-1550) and delivered via a multimode fiber to the spectrometer (Flame NIR) for spectroscopic investigations. The output from the 10% port of the beam splitter is routed to the Raptor camera for imaging purposes.

We were able to detect emission from these samples by focusing the pump beam using a high numerical aperture (0.85) microscope objective and collecting the resulting PL spectrum with the same objective lens. All of the spectra below were recorded with an integration time of 10 seconds and no averaging, using the Ocean Optics NIRFlame spectrometer (950 nm -1650 nm operational range), under excitation power of 0.4 mW. Note that the spectral resolution of the NIRFlame instrument is limited to ~ 6 nm. A typical result, for a dome with a base diameter of 60 μm and a peak height of ~ 2.3 μm, is shown in Figure 4.22. As for all of the domes on this wafer, the optical spectrum is not of particularly high quality (see Figure 4.22(a)), exhibiting significant ripple and HG/LG modes with large linewidth. Because of this, there is very little evidence for spectral modification of the Er emission (see Figure 4.22(b)).
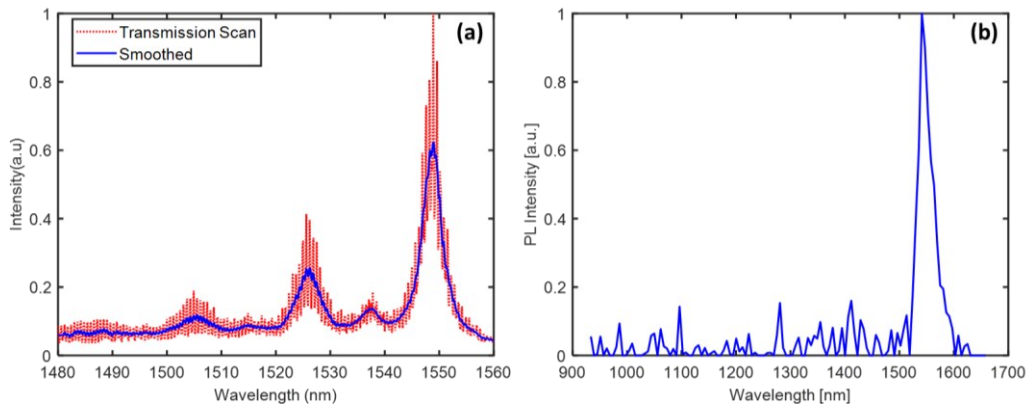
Figure 4.22. Transmission scan for 60 μm buckled dome, (b) PL measurement for the same dome as in part a.

While no obvious signatures of spectral reshaping of the Er emission into cavity modes could be discerned, preliminary evidence for cavity-enhancement of the emission intensity was observed,

as follows. The emission spectra from three different samples, each with a 100 nm thick SiO:Er layer, were collected under identical excitation and collection conditions. The three samples were as follows: - SiO:Er on a glass slide, SiO:Er on the bottom mirror only (half cavity), and SiO:Er inside a buckled dome cavity with base diameter 70 μm and peak height ~ 1.8 μm. For all of these measurements, the NIRFlame spectrometer was configured with an integration time of 3 seconds and the data points were averaged 45 times, while the laser excitation power was fixed at ~ 30 mW, and focused onto the samples via an infinity-corrected objective lens with 50x magnification.

Figure 4.23 compares the PL emission collected from the three samples. As above, there was no clear evidence for spectral re-shaping of the erbium emission for the mirror or cavity samples. However, there was a significant increase in the intensity of the collected emission, with the mirror sample exhibiting ~ 5x stronger emission compared to the glass-slide sample, and the cavity sample exhibiting ~ 9x stronger emission compared to the glass slide sample. Given that some of the pump light is undoubtedly absorbed, reflected, or scattered by the upper mirror in the cavity sample, we concluded that this result could be interpreted as preliminary evidence for cavity-enhanced erbium emission.
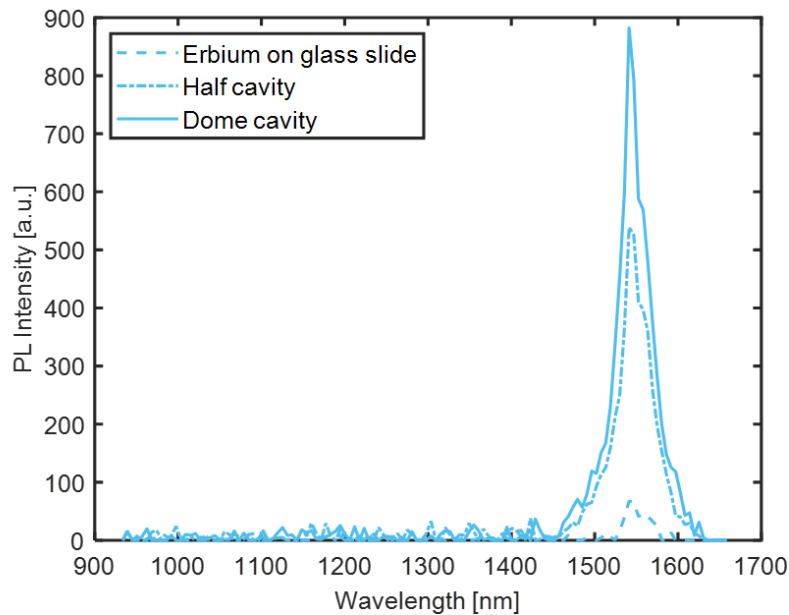
Figure 4.23. PL measurements for three different samples with nominally identical (~100 nm thick) SiO:Er active layers, and with fixed excitation and collection conditions, provided preliminary evidence for cavity-enhanced emission. The plot shows PL emission collected for an SiO:Er layer on a glass slide (dashed curve), SiO:Er layer on a bottom mirror (dotted curve), and SiO:Er layer inside a buckled dome cavity (solid curve) with 70 μm base-diameter and ~1.8 μm peak height.

An obvious question to consider is whether the ~9x enhancement observed above is reasonable. Note that for the domes on this chip exhibiting a fundamental resonance aligned to the Erbium emission band (i.e., ~ 1520-1560 nm), the linewidth was found to be ~ 5 nm or greater, suggesting a cavity $Q \sim 300$, at best. Given the height of the dome considered in Figure 4.23, a cavity finesse $\mathcal{F} \sim Q/3 \sim 100$ can thus be estimated. Using a planar Fabry-Perot approximation, the general expression for the finesse is $\mathcal{F} \sim \pi \cdot (R_t R_b)^{1/4}/(1-(R_t R_b)^{1/2})$, where R_t and R_b are the effective reflectance of the top and bottom mirrors, respectively. Here, $R_b \sim 0.999$ can be assumed for the 4.5-period a-Si/SiO$_2$ bottom mirror [83]. It follows that $R_t \sim 0.94$ in the wavelength range of interest, much lower than the projected value for a 7.5-period Ta$_2$O$_5$/SiO$_2$ Bragg mirror, but perhaps not surprising given the visual damage (cloudiness) described above.

Now, if the emission collected by the objective lens could be entirely associated with a single cavity mode, it would make sense to compare the observed enhancement to the predicted Purcell factor. However, here the cavities are characterized by a family of relatively low-Q and overlapping Laguerre-Gaussian modes, and several of these modes lie within the broad Er emission band (see for example Figure 4.22). Thus, it is more reasonable to use a planar Fabry-Perot model (i.e., as in Figure 4.19) to assess the emission inside these cavities. For such a cavity, the emission in the surface-normal direction is enhanced relative to the no-cavity case, with the enhancement factor given by [141]:

$$G = \frac{\left(1+\sqrt{R_b}\right)^2 (1-R_t)}{\left(1-\sqrt{R_t R_b}\right)^2} \cdot \left|\frac{E}{E_{max}}\right|^2 \quad , \tag{4.1}$$

where $|E/E_{max}|^2 \sim 0.34$ is the relative modal electric field intensity at the emitter position (see Figure 4.19). Combining this with the mirror reflectance estimates from above gives G ~ 85, which is an order-of-magnitude higher than the observed ~ 9x enhancement from above. Residual discrepancy can partly be attributed to the use of a planar model, which is only approximately representative of the real cavity, and partly to the reduced pump intensity at the active layer of the cavity sample, mentioned above. Moreover, the preceding equation is strictly valid for emission into the surface-normal direction only, while our experimental setup collects emission over the entire angular range lying within the numerical aperture of the objective lens. While the agreement between theory and experiment is not particularly good, a more conclusive study would require higher-quality devices and is left for future work.

4.4 Conclusions

Two different strategies were investigated for embedding an erbium-doped silicon monoxide active layer inside buckled domed microcavities. Moreover, an optical microscope system for performing cavity transmission and micro-PL measurements was assembled. In the first fabrication attempt, we embedded patterned SiO:Er pads inside cavities with a-Si/SiO$_2$-based upper and lower mirrors. This attempt unfortunately produced a low yield of successful buckling (~ 4 %), which was later attributed to the use of a SiO$_2$ layer as the last layer in the bottom mirror. While the few domes realized in this case showed promising optical properties, we were not able to measure PL from the SiO:Er layer inside these domes. This was partly due to the absorptive nature of the a-Si-based upper mirror in the wavelength range below ~ 800 nm, where the SiO:Er layer can be most efficiently pumped through host-mediated absorption.

In the second fabrication attempt, we employed a uniform (un-patterned) and slightly thicker (~ 100 nm) SiO:Er layer. We also used a Ta$_2$O$_5$/SiO$_2$-based upper mirror, which has potential for low absorption throughout the visible wavelength region. On this wafer, chips with either 5.5- or 7.5-period upper mirrors were fabricated. While this second attempt resulted in a much better yield of buckled devices (~ 50 % on some chips), the optical properties of the devices were of significantly lower quality. We speculated that this was due to a combination of a low upper-mirror reflectance, possibly arising from contaminated sputtering depositions, and sub-optimal buckle shape, possibly arising from lower-than-expected stress in the buckled mirror. In spite of the somewhat inferior optical properties (i.e., low Q-factor optical modes), preliminary evidence for cavity-enhanced PL was achieved. With future improvements in the fabrication processes, the strategies outlined here could lay the groundwork for future implementations of monolithic CQED devices operating in the telecom wavelength range.

Chapter 5 [1]

Pressure sensing with high-finesse monolithic buckled dome microcavities

We describe the use of on-chip buckled-dome Fabry-Perot microcavities as pressure sensing elements. The cavities, fabricated by a controlled thin-film buckling process, are inherently sealed and support stable optical modes (finesse $>10^3$), which are well-suited to coupling by single-mode fibers. Changes in external pressure deflect the buckled upper mirror, leading to changes in resonance wavelengths. Experimental shifts are shown to be in good agreement with theoretical predictions. Sensitivities as large as ~1 nm/kPa, attributable to the low thickness (< 2 μm) of the buckled mirror, and resolution ~ 10 Pa are demonstrated. We discuss potential advantages over traditional low-finesse, quasi-planar Fabry-Perot pressure sensors.

5.1 Background and introduction

Optical pressure sensors have well-known attributes such as immunity to electromagnetic interference (EMI) and potential for operation in harsh environments [142,143]. Diaphragm-based extrinsic Fabry-Perot interferometers (DEFPI) [143] have been amongst the most popular types. In the DEFPI, a flexible membrane is configured as one mirror in a typically low-finesse, planar Fabry-Perot structure, separated from the second 'mirror' (often a simple optical interface such as the cleaved end facet of an optical fiber) by a sealed and 'empty' (typically air) cavity. Changes in external pressure deflect the membrane and modify the interference spectrum, thereby enabling optical detection [143]. Most DEFPI work has targeted high-sensitivity, low-pressure [144] and acoustic wave [145] applications, although high-pressure sensors have also been achieved [146]. The thickness, material stiffness (i.e., Young's modulus), and diameter of the membrane correlate directly with the pressure sensitivity, operating range, and maximum frequency response of the device [75,147]. Thus, a wide variety of membrane materials have been studied, ranging from graphene [148] to stainless steel [149], amongst many others. Most are fabricated using some combination of surface- and bulk-micromachining, involving a membrane

---

[1] This chapter was published in *Applied Optics*, vol 60, No.29, 2021.

bonding (and sometimes thinning) step that seals the space between the membrane and the second optical interface [150,151]. These tend to be relatively complex and time-consuming serial processes.

As mentioned, nearly all reported DEFPI devices are planar structures with relatively low finesse. Planar FPIs are marginally unstable as optical resonators, and are thus subject to various finesse-reducing non-idealities [152], particularly when illuminated by non-collimated light from Gaussian laser beams or fiber modes [153–155]. Accordingly, sensing is typically carried out by monitoring the shift of spectrally broad, nearly periodic Fabry-Perot fringes, which limits the detection sensitivity and/or necessitates the use of relatively complex signal processing algorithms [156]. There have been some efforts towards implementing higher-finesse planar-cavity-based pressure sensors [80], but their performance (e.g., reported finesse ~ 64 in Ref. [80]) is ultimately limited by the factors mentioned above.

It is well known [157] that the detection limit (i.e., the minimum resolvable shift in some measurand) for optical cavity sensors typically scales with the linewidth of the resonance, or inversely with the quality (Q) factor. From a simplistic point of view, the minimum resolvable shift in resonant wavelength ($\Delta\lambda_{min}$) can be approximated by the linewidth ($\delta\lambda$); i.e., $\Delta\lambda_{min}$ ~ $\delta\lambda$ [158]. A more detailed treatment needs to consider various noise sources [159], but predicts similar trends. For example, White and Fan [160] estimated that $s \approx \delta\lambda/(4.5 \cdot SNR^{0.25})$, where s is the standard deviation (i.e. uncertainty) in the estimation of a resonant wavelength, $\delta\lambda = \lambda/Q$, and *SNR* is the overall signal-to-noise ratio of the detection system in linear units. These relationships and trends hold over a wide range of practical Q-factors [159] and have motivated the use of high-Q microcavities for refractive-index-based sensors [157,158,160]. A similar strategy might yield advantages for precision monitoring of low pressures and weak acoustic signals [144].

Here, we describe pressure sensing with on-chip buckled-dome microcavities [83,84,86], whose properties address many of the shortcomings of conventional DEFPI devices. First, these cavities are manufactured in a completely monolithic process which can yield high-density arrays on a single chip. Second, the process produces inherently sealed cavities with an upper curved mirror of thickness on the order of ~ 1 - 2 μm. Third, the cavities support high-quality and stable Laguerre-Gaussian modes, naturally suited to coupling by single-mode fibers and laser beams. We show that the operating range and sensitivity for pressure sensing can be varied through the choice

of the cavity dimensions, achieving sensitivities in the range ~ 0.05 – 1 nm/kPa. The cavities also exhibit high finesse ($>10^3$) and high vibrational resonance frequencies (> 1 MHz), which might make them interesting candidates for sensing of low-intensity and high-speed pressure phenomena.

5.2 Pressure-driven deflection of a buckled cavity - theory

The fabrication and optical properties of the buckled cavities used in this work have been detailed elsewhere [83,84]. Briefly, these cavities are fabricated by embedding circular patterns of a thin low-adhesion layer between two Bragg mirrors and subsequently inducing delamination buckles to form over these regions, driven by compressive stress in the upper Bragg mirror. The self-assembly nature of the process results in a highly predictable and smooth morphology, and the cavities tend to exhibit the 'textbook' Laguerre-Gaussian modes expected for a half-symmetric (plano-convex) spherical mirror cavity [83]. We have demonstrated cavities with base diameters ranging from ~50 μm to several hundred micrometers (μm), and heights ranging from sub-μm to several μm. Figure 5.1(a) shows a microscope image of a typical array of cavities, and the inset shows a typical mode-field intensity image for the fundamental TEM$_{00}$ mode of these cavities. Note that the fundamental mode-field diameter is typically on the order of several μm and can be well-matched to that of a standard single-mode fiber through appropriate engineering of the buckle shape (i.e., the effective curvature of the buckled mirror, and so on. [83]).
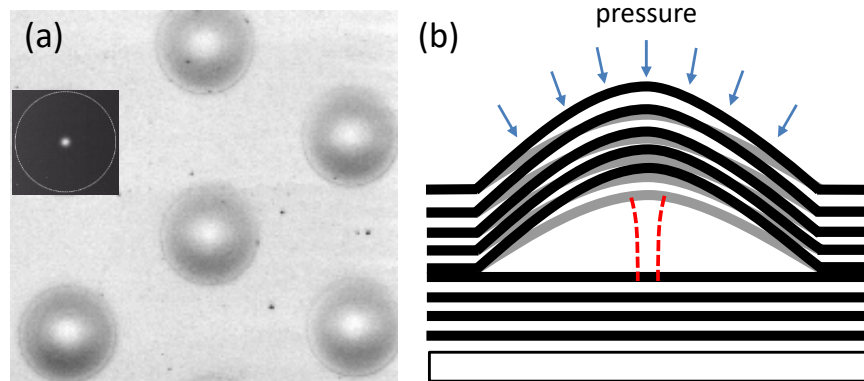
Figure 5.1. (a) Microscope image of an array of 50 μm base-diameter domes is shown. Inset: a typical fundamental mode-field profile (~5 μm diameter) is overlaid on one dome; the dashed white line indicates the dome perimeter. (b) Schematic illustration of a buckled-dome in cross-section, illustrating a reduction in cavity height (black to grey) caused by an increase in external pressure. The resonant optical cavity modes, including the fundamental mode represented by the red dashed lines, are modified accordingly.

We have previously [86] analyzed the thermo-mechanical properties of similar dome cavities, including first-order treatments of the vibrational resonance frequencies of the buckled mirror and the temperature dependence of the resonant optical modes. Here, we are concerned with the changes in the cavity height (and thus the optical properties) induced by changes in external pressure. As depicted in Figure 5.1(b), the pressure acts as a distributed force on the buckled mirror, which modifies its height and shape and thus modifies the optical spectrum.

For the present study, we focus on two types of devices borrowed from our previous work. First, we studied a set of domes with 50 μm base diameter and 5.5-period a-Si/SiO$_2$ buckled mirrors [83], which we label here as device type A. Second, we studied a set of domes with 100 μm base diameter and 4.5-period a-Si/SiO$_2$ buckled mirrors [84], which we label here as device type B. Nominally identical thin-film layers and layer thicknesses (quarter-wave layers at 1550 nm wavelength) are common to both samples. Specifically, nominal layer thicknesses are ~105 nm and ~ 265 nm for a-Si and SiO$_2$ layers, respectively, based on our typical refractive indices (~3.7 and ~1.46 at 1550 nm wavelength) for our sputtered films. Furthermore, to characterize the upper buckled mirror, we assumed the same effective-medium parameters as in Ref. [86]; Young's modulus $E = 70$ GPa, Poisson's ratio $\nu = 0.2$, and mass density $\rho = 2240$ kg/m^3.

To guide and corroborate the experimental results presented in Section 5.3, we seek an approximate theory of the pressure sensitivity. First, it is worth noting that the gas composition in the 'empty' region of the cavities is not completely known. Coupeau et al. [161] have studied this issue for sealed delamination buckles in simple metal films, and have provided evidence that the region under the buckle is evacuated. In our case, the buckling delamination arises in part from the thermal decomposition of a thin fluorocarbon layer [81], so that a partial vacuum is more likely. In any case, the impact of the internal pressure on the starting buckle profile is typically small [161]. Moreover, our main interest is to assess the changes in the buckle height (i.e., not absolute values), so we ignore this detail here.

The impact of differential (i.e., external minus internal) pressure on buckling height and profile has been studied for both straight-sided (Euler) buckles [162] and circular buckles [163]. A rigorous treatment must take into account details such as the residual stress in the buckled films [164] and substrate stiffness, and typically only numerical solutions are possible [162]. Moreover, our larger buckled cavities often deviate from the predictions of elastic buckling theory,

exhibiting a shape closer to that of a spherical dome [86] due to plastic deformation near the perimeter of the buckled feature. Here, however, we restrict our study to smaller domes (50 and 100 μm base diameters), which we have shown [83] are relatively well approximated by elastic buckling theory. In that case, and in the limit of small deflections and low residual in-plane stress, the pressure-induced deflection of a circular delamination buckle can be approximated as [165]:

$$S_{P1} = \frac{\Delta\delta}{\Delta P} \approx \frac{3\cdot(1-v^2)\cdot a^4}{16\cdot E\cdot h^3} \quad .$$ (5.1)

Here, δ is the peak height of the buckle (i.e., the effective mirror spacing), P is the external pressure, a is the base radius of the buckle, h is the thickness of the buckled mirror, and E and v are the effective-medium Young's modulus and Poisson's ratio of the buckled mirror. We expect this expression to overestimate the actual pressure sensitivity, as follows: for typically higher values of residual stress required to drive the delamination in practice, the buckled mirror will deflect less (i.e., be stiffer) in response to lateral forces [165], such that the pressure sensitivity can be expected to be a few times lower than predicted by Eq. 5.1 (see the numerical results in Fig. 8 of Ref. [163], for example). This will be particularly true for larger delamination buckles, which have higher values of σ/σ_c, where σ_c is the in-plane stress driving buckling and σ_c is the critical (i.e., minimum) stress to induce buckling, the latter of which scales inversely with the square of the base radius [1]. Nevertheless, Eq. 5.1 is expected to be 'order-of-magnitude' correct, at least in the small-deflection limit (we added the '1' to the subscript of S_{P1} to denote a first-order approximation).

In optical detection of pressure changes, it is not the change in cavity length which is directly probed, but rather changes in the spectral properties. Here, we focus mainly on the shift in peak wavelength of the fundamental cavity resonance, which can be expressed as:

$$S_{\lambda 1} \equiv \frac{\Delta\lambda}{\Delta P} \approx \frac{2\cdot S_P}{m} \quad ,$$ (5.2)

where $m \sim \delta/(\lambda/2)$ is the longitudinal mode order of the cavity.

Table 5-1. Assumed and Predicted Parameters for Cavities Studied[a]

Device type	A (Ref. [83])	B (Ref. [84])
Base radius, a	25 [μm]	50 [μm]
Mirror thickness, h	1.95 [μm]	1.59 [μm]
Mirror mass, m_B	8 [ng]	28 [ng]
Mode order, m	1	3
Pressure sensitivity, S_{PI}	0.14 [nm/kPa]	4 [nm/kPa]
Pressure response, $S_{P\lambda}$	0.28 [nm/kPa]	2.7 [nm/kPa]
Vibrational resonance, f_0	11.9 [MHz]	2.5 [MHz]

[a]Optical properties of device types A and B were detailed in Refs. [83,84], respectively.

Another parameter of interest is the fundamental vibrational resonance frequency of the buckled mirror, which plays a key role in determining its maximum response rate as a dynamic pressure sensor [145,147,151]. We can estimate this using a classical harmonic oscillator model, i.e., $\omega_0 \sim (K_0/m_0)^{1/2}$, where K_0 and m_0 are an effective spring constant and mass for the fundamental vibrational mode [86]. We use $K_0 = \Delta F/\Delta \delta \sim (\pi a^2)/S_{P1}$, where F is the lateral force induced by the differential pressure. Furthermore, we estimate $m_0 \sim 0.3\, m_B$ [166], where m_B is the mass of the buckled mirror. For the type A and B domes described above, the resulting predictions for pressure sensitivity and vibrational resonance frequency are summarized in Table 5-1, and in both cases show reasonable agreement with the experimental results in Section 5.3. Subject to the comments above, this suggests that the simple theories outlined capture the essential physics.

5.3 Pressure sensing with buckled cavities -experiment

In order to experimentally study the cavities under variable pressure, we placed them inside the custom chamber depicted in Figure 5.2. The sealed enclosure is plumbed to an air compressor to enable pressurization, and the pressure is monitored by a digital gauge (Baker B50015 Digital Pressure Gauge). Note that all pressures stated below are relative to the lab pressure. The sample sits between input and output optical windows (High-Vacuum CF Flange Viewports for Ø1.5″ Windows) to enable optical transmission measurements. A tunable laser (Santec TSL-710) was coupled to a reflective collimator (Thorlabs RC-08) followed by a positive lens (KBX 058, $f=$ 75.00 mm), and coupled into the chamber through the input window. This resulted in a spot size

~ 20 μm in diameter at the device plane. Light transmitted through the output window was collected by a long-working-distance objective lens (50x Mitutoyo Plan APO) and delivered to a near-infrared camera (Raptor Photonics Ninox 640 NX1.7-VS-CL-640). In addition to capturing mode-field images, the camera was also used as the detector in obtaining spectral scans, by summing the pixel intensity over the region of the image containing the low-order cavity modes. Some of the transmitted light was tapped off by a beam splitter and delivered to a high-speed photodetector (Resolved Instruments DPD80), to enable 'tuned-to-slope' measurements of the mechanical/vibrational spectra of the domes [86].
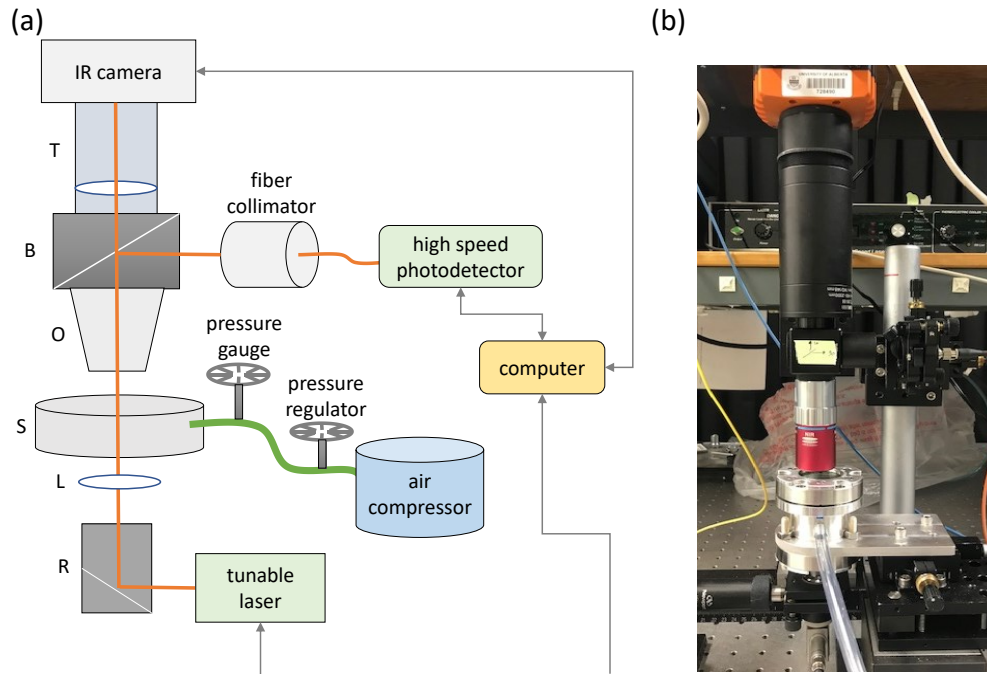
Figure 5.2. (a) Schematic diagram of the experimental setup. The symbols indicate: R (reflective collimator), L (lens), S (sample chamber), O (long-working-distance objective lens), B (beam splitter), and T (tube lens). (b) Photograph of the setup.

Typical pressure-induced changes in the optical transmission spectra for a type B dome are shown by the series of plots in Figure 5.3(a). As mentioned, these devices exhibit the characteristic resonance spectra of spherical mirror cavities, associated with stable Laguerre/Hermite-Gaussian (LG/HG) modes. The fundamental transverse mode (LG_{00m} for a given longitudinal mode order m) is associated with the longest wavelength peak in the spectrum, and the higher-order transverse modes produce a series of peaks moving towards shorter wavelengths. As the external pressure is

increased, the cavity height is reduced (see Figure 5.1(b)), and the resonance spectrum shifts towards shorter wavelengths. Notably, the overall shape of the spectrum is relatively constant, with no significant change in 'fringe contrast' or linewidth.

Figure 5.3(b) shows plots of the fundamental resonance wavelength versus the pressure for two different type B domes. These domes have a peak height of $\delta \sim 2.4$ µm and thus are operating in longitudinal mode order $m = 3$ at $\lambda \sim 1600$ nm. Slight variations in height (and thus resonance wavelength) between domes of the same base diameter are typical for our process [83]. Both domes exhibit a nearly linear response with $S_\lambda \sim 0.7$ nm/kPa, and relatively little hysteresis. Note that the wavelength was measured at a series of increasing pressures and then again as the system pressure was reduced back down. There is some discrepancy between pressure-up and pressure-down data points in the low-pressure range, which is likely due to uncontrolled drifts in temperature and lab pressure over the relatively long interval between those particular measurements. As we expected (see the discussion in Section 5.2), the measured S_λ is slightly lower than the first-order theoretical estimate derived from Eq. 5.1 ($S_{\lambda 1} \sim 2.7$ nm/kPa).

Figure 5.3. (a) Spectral scans at a series of fixed pressures (as labeled inset) are shown for a typical 100 µm base-diameter (type B) dome. The vertical axis is normalized intensity. (b) Plot of the peak wavelength of the fundamental mode resonance versus pressure, for both increasing and decreasing pressure, for a pair of similar domes (see main text for details). A linear fit to the data is also shown in each case.

In addition to good linearity and repeatability (including low hysteresis) over a wide range of pressures, another desirable property of a pressure sensor is good resolution (i.e., that the minimum pressure change that can be reliably detected is as small as possible). In general, resolution is intimately tied up with the detection algorithm and the SNR of the detection system [143]. For the present setup, we used some relatively simple experiments to place an upper limit on the resolution. Figure 5.4(a) shows scans of the fundamental resonance taken at a relatively small step size (5 pm) setting of the tunable laser, and for the smallest increment in pressure (~300 Pa) that we could reliably control in our system. Note that the shift in wavelength is greater than the linewidth ($\delta \lambda \sim 0.2$ nm), so that detection of pressure changes much smaller than 300 Pa would be possible assuming sufficiently high system SNR [167]. Also note that the periodic, low-amplitude ripple in these scans (but more obvious in Figure 5.5(a)) is caused by substrate reflections [83], and could be eliminated with the addition of an appropriate anti-reflection coating.

As a second means to assess the resolution, we extracted the peak wavelength over a relatively long period of time at a nominally fixed value of chamber pressure (0 kPa). The results of such an experiment are shown in Figure 5.4(b), where the time interval between each measurement was ~ 5 minutes, and the horizontal axis thus spans a total time > 3 hours. The data reveals the presence of a relatively slow drift, which is likely attributable to variations in the laboratory temperature (and possibly pressure, which would affect the reading provided by the differential pressure gauge) over the course of several hours. The issue of temperature-pressure cross-sensitivity is discussed in Section 5.4. Nevertheless, the 'noise level' can be characterized by the variations in peak wavelength over shorter intervals of the plot [80]. For example, the variation for trials 7-11 appears to be within ~ 10 pm. Given the pressure response sensitivity $S_\lambda \sim 1$ nm/kPa, this would suggest the potential to resolve pressure changes on the order of 10 Pa, assuming some means are introduced to compensate thermal drift.
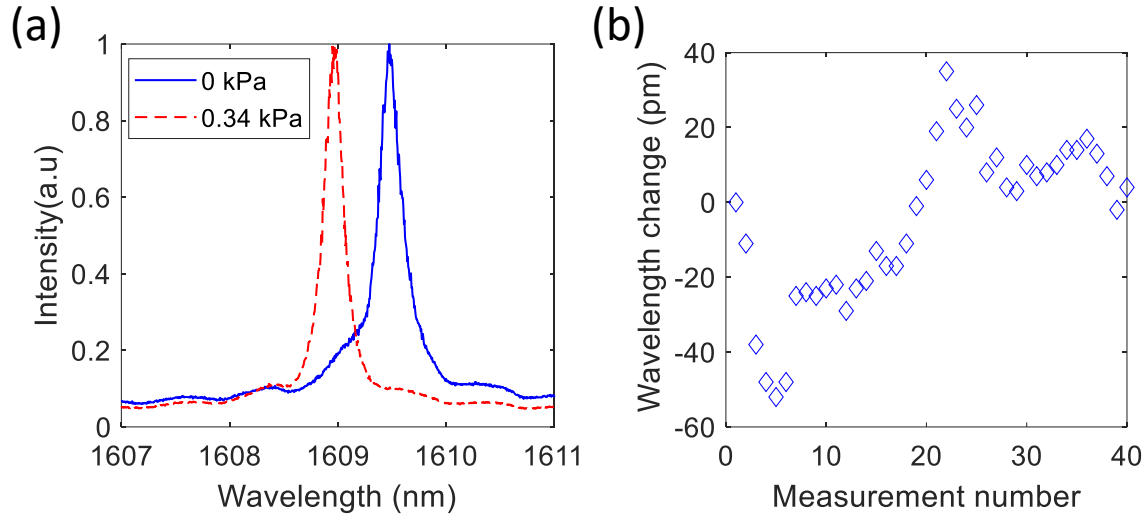
Figure 5.4. (a) Plot shows the fundamental resonance for a type *B* dome; there is a clearly-resolved shift to lower wavelength when the external pressure is increased from 0 to ~0.34 kPa. (b) The change in peak wavelength at 'fixed' pressure (0 kPa) for the cavity in part a, extracted from a large number of spectral scans (i.e., trials) taken at ~ 5 minute intervals.

We next consider results for the smaller and stiffer (type *A*) domes, with peak height $\delta \sim 0.8$ μm and operating in longitudinal mode order $m = 1$. Figure 5.5(a) shows a series of spectral scans at fixed pressure settings, revealing the same trends as discussed for type *B* domes above. Note that the substrate-reflection-induced ripple is much more noticeable in these scans. This is partly due to the poor mode matching between the input beam spot size (~20 μm) and the fundamental mode spot size (~5 μm diameter) for these cavities [83]. The fundamental mode spot size for the larger (type *B*) domes (~10 μm diameter [84,86]) is more closely matched to the input beam, although still not perfectly. The input beam spot size is determined by the long focal length lens required here, in turn due to the long distance between the optical input window and the sample plane of the pressure chamber. Improved packaging and the addition of an anti-reflection coating would be expected to significantly mitigate the ripple.
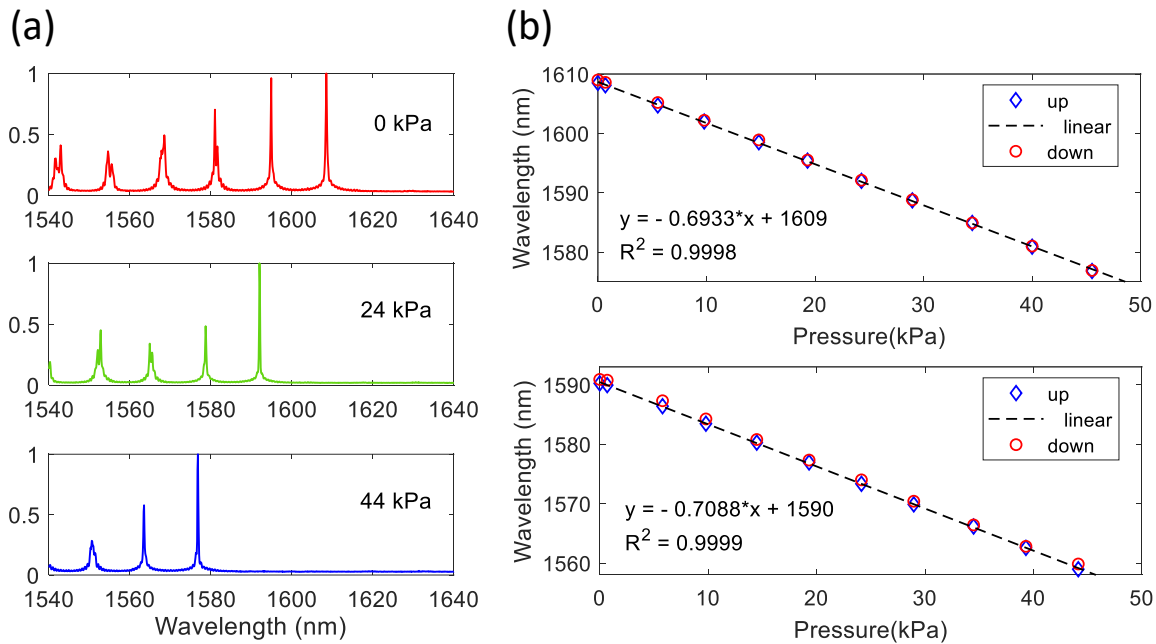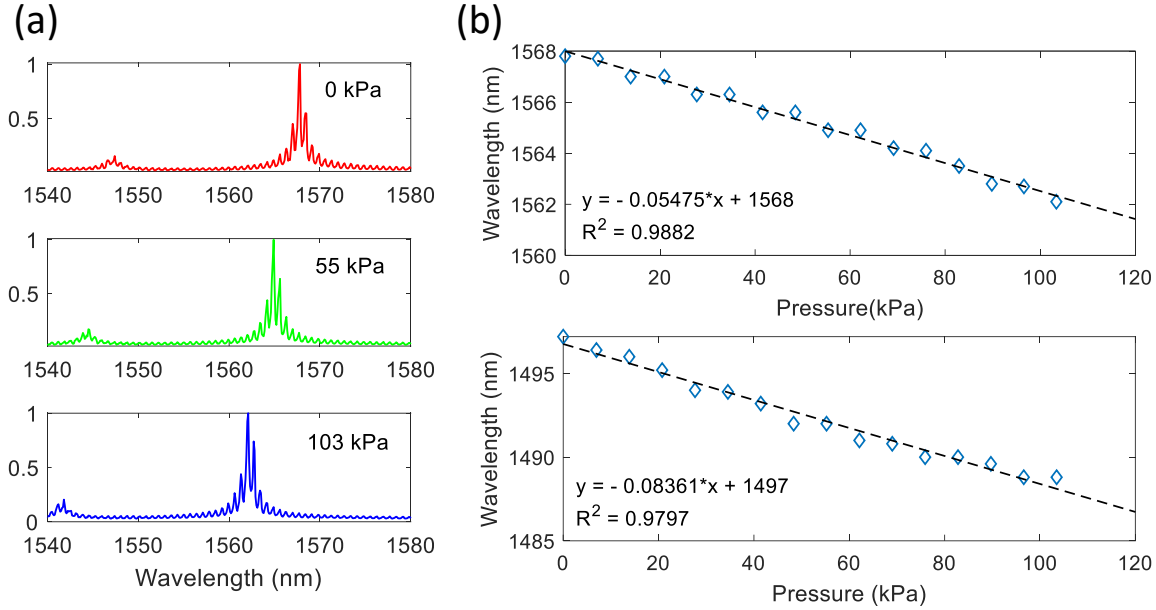
Figure 5.5. (a) Spectral scans at a series of fixed pressures (as labeled inset) are shown for a typical 50 μm base-diameter (type *A*) dome. The vertical axis is normalized intensity. (b) Plot of the peak wavelength of the fundamental mode resonance versus pressure, overlaid by a linear fit to the data, is shown for two different types *A* domes.

The fundamental resonance wavelength versus pressure for the dome from Figure 5.5(a), as well as that for a second type *A* dome, is plotted in Figure 5.5(b). For both domes, the pressure response is approximately linear over the 0 – 103 kPa range, although deviations from linearity are more apparent than for the type *B* domes above. We attribute this mainly to the parasitic ripple mentioned, which impacts the identification of the resonance peak. While the pressure range studied was limited by our experimental apparatus, we expect the approximately linear response to extend to significantly higher pressures, given that the maximum height deflection (from Figure 5.5 and Eq. (5.2)) is only a few nanometers (i.e. < 1 % of the starting height) at ~103 kPa.

The type *A* domes also showed somewhat higher variation in their pressure sensitivity, for example $S_\lambda \sim 0.055$ nm/kPa and $S_\lambda \sim 0.083$ nm/kPa for the representative cavities from Figure 5.5 (b). Slight variations in buckle height mentioned above, typical for our experimental fabrication process, likely have a greater impact on the residual stress (and thus stiffness) of the buckled mirror for these smaller and shorter cavities. In any case, these values are in reasonable agreement with the predictions from Section 5.2 ($S_{\lambda 1} \sim 0.28$ nm/kPa), again somewhat lower for the reasons

discussed above. Notably, the ratio of experimental sensitivity for type A and B domes ($S_{\lambda A} / S_{\lambda B}$ ~ 0.1) is in very good agreement with the predictions of the simple theoretical model.

Taken together, the results for type A and B domes show that, within limits of elastic buckling [165] and for buckle heights exceeding the minimum value to support resonant optical modes at the probe wavelength of interest, there is scope to design cavities to provide either higher sensitivity or higher operating range. It should also be noted that, while not done here, we routinely deposit low-stress, half-wave (i.e., optically 'vanishing') capping layers on top of existing cavities (i.e., post-buckling), which offers another means to increase the stiffness (and thus operating range) for a particular type of cavity.

Finally, we also measured the mechanical/vibrational resonance spectra of these devices using a tuned-to-slope technique described in our previous work [86,168]. In this technique, the laser is tuned to a wavelength just slightly removed from the fundamental cavity resonance (i.e., somewhere near the half-maximum transmission point of the Lorentzian cavity line-shape). In this way, vibrational motions of the upper mirror are translated to changes in cavity transmission. The thermal vibrational frequency spectrum of the buckled mirror can thus be extracted from a Fourier transform of the time-varying intensity signal recorded by a high-speed photodetector receiver. Typical results for type B and A cavities are shown in Figure 5.6 (a) and Figure 5.6 (b), respectively. Note that the lower SNR for the measurement of the type A cavity is due to the relatively poor input coupling efficiency mentioned above. The fundamental vibrational frequencies, at ~2.9 MHz for the type B cavity and at ~10.6 MHz for the type A cavity, are in good agreement with the first-order predictions from Section 5.2. Such high vibrational frequencies suggest good potential for sensing dynamic pressure (e.g., ultrasound [169]) signals. We hope to explore these applications in future work.
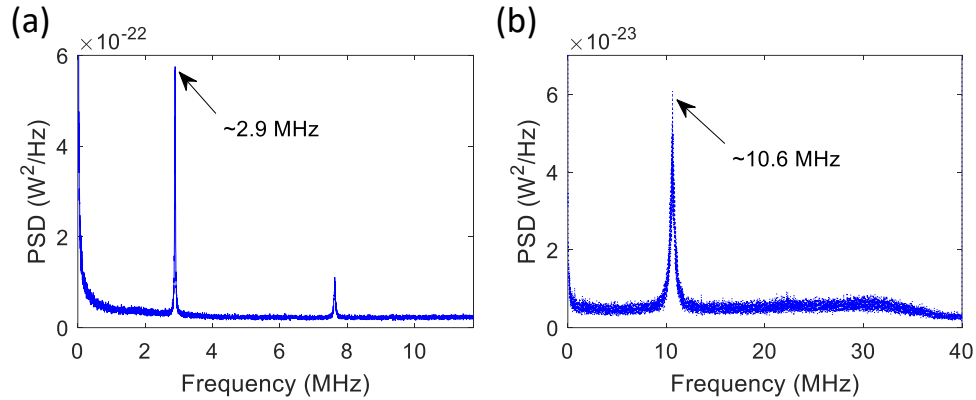
Figure 5.6. Vibrational spectrum for a typical type *B* dome, with the fundamental resonant mode indicated. (b) Vibrational spectrum for a typical type *A* dome, with the fundamental resonant mode indicated.

5.4 **Discussion and conclusions**

We described the proof-of-principle for pressure sensing using high-finesse buckled dome Fabry-Perot microcavities. While these experiments were carried out on an optical bench, there is a good potential to integrate these chips directly with optical fiber arrays, which would facilitate their use as embedded sensors. Conceivably, a buckled dome cavity could even be fabricated directly on the end of a cleaved optical fiber, although this would require additional process development. In any case, a distinct advantage of these devices is their potential for good optical mode matching to single-mode fibers, negating the need for supplementary optics such as packaged collimators [80].

Another significant advantage is their support of stable, high-finesse cavity modes. This could enable a wide range of simplified and high-accuracy detection algorithms to be employed, such as the sophisticated peak-detection algorithms widely developed for fiber Bragg grating sensors [167]. With sufficiently high system SNR and stability, those algorithms could potentially enable pressure resolution well below the value demonstrated here (~10 Pa). Finally, it is worth reiterating that the small size and high vibrational resonance frequencies of these devices, along with the fact that they can be fabricated in dense on-chip arrays, make them potentially interesting for dynamic pressure sensing applications such as photoacoustic imaging [170]. Indeed, Guggenheim *et al.* [169] have already demonstrated a host of advantages (e.g., high sensitivity, wide bandwidth, and omnidirectionality) for analogous (although serially processed) Plano-concave microcavities used as ultrasound sensors.

One challenge of note, which is a well-known issue for DEFPI-based sensors (and most pressure sensors), is that of temperature-pressure cross-sensitivity [143,150]. We have reported previously [83,86] on the temperature dependence of the buckled-dome cavities, including a basic description of the underlying physics. While temperature stabilization is always possible, it adds cost and complexity. Another approach, often employed in FBG sensing, is to embed a second sensor that responds only to temperature, and use it to calibrate/remove the temperature dependence of the pressure sensing device. In the present case, this could be achieved by using a cavity with holes machined through the buckled mirror [84]. We verified (not shown) that cavities of this type were insensitive to pressure changes within the resolution of our test setup, exhibiting constant optical spectra at a fixed temperature. A complete study of mitigating temperature cross-sensitivity is left for future work.

Chapter 6

Conclusions and Outlook

6.1 **Summary of the thesis**

The main theme of this thesis was the development of monolithic strategies for embedding solid-state emitters within buckled dome microcavities. As discussed in Chapter 1, control over spontaneous emission in microcavities could be attractive for many applications, including miniature threshold-less lasers, CQED, and sensing. The thesis work also included a study of the pressure sensitivity of buckled dome microcavities. This study showed that these cavities have unique attributes that could make them interesting for high-speed sensing of dynamic pressure signals. Viewed from another perspective, the study showed that control of ambient pressure could be used as means to tune the optical resonance spectrum of the buckled dome cavities, which is needed for most envisioned CQED applications. The following sections provide a more detailed summary of the theoretical and experimental results, and of the main contributions of this Ph.D. thesis.

6.1.1 Theoretical study of spontaneous emission control in buckled dome microcavities

In Chapter 3, a theoretical study of dipole emitters (in the 1550 nm wavelength range) inside buckled-dome Fabry-Perot cavities with Si/SiO_2-based, omnidirectional Bragg mirrors was presented. Quasi-analytical results from a planar-equivalent cavity model were supported by a numerical FDTD study for the 3-D model cavity structure. Notably, our study showed that these cavities can provide some of the same benefits as promised by 3-D photonic crystal microcavities. Specifically, simultaneous enhancement of spontaneous emission into a desired cavity mode (i.e., a high Purcell factor) and inhibition of spontaneous emission into background modes is possible. Moreover, buckled dome cavities have already been fabricated in large-scale arrays, while 3-D photonic crystal cavities (in spite of decades of effort) remain challenging to implement at optical frequencies. For the cavity considered (modeled on devices which our group has previously fabricated) and an optimally located dipole, a Purcell factor of ~ 120 combined with an inhibition

factor ~ 25 for emission into background radiation modes was predicted. It is the enclosed nature of the buckled dome microcavities, combined with the use of planar omnidirectional mirrors, which makes this possible. Finally, our study demonstrated that the inhibition of radiation into background modes could make it possible to achieve high single-atom cooperativities, even for a cavity with a moderate Q-factor. This theoretical study motivated much of the experimental work in the remainder of the thesis project, which was focused on alternative strategies for embedding (ideally using monolithic fabrication strategies) 'quantum' emitters into buckled dome microcavities.

6.1.2 Erbium emitters inside buckled dome cavities

Chapter 4 outlined two attempts to develop a monolithic fabrication process for embedding 1550-nm-wavelength-range active light-emitting layers (SiO:Er) inside arrays of on-chip, buckled-dome Fabry-Perot microcavities. A brief introduction to the erbium-doped silicon monoxide (SiO:Er) material system was given, and optical properties of the thin film were provided. SiO:Er films were fabricated using a high-vacuum physical vapour deposition (PVD) system (i.e., by thermal evaporation) as described in Ref. [131,132]. Two attempts of patterning/positioning the thin layer of the SiO:Er were elucidated. Buckled microcavities were fabricated 'around' the SiO:Er active layers, using a standard photolithography and lift-off process (e.g., in Ref [1,83]). In the first attempt, a variety of SiO:Er pads (from 1µm to 10 µm in diameter) were aligned to buckled dome cavities with base diameters in the range from 30 µm to 150 µm. However, only the 10 µm SiO:Er pads inside domes with 60 µm and 70 µm base diameters survived the buckling process. One major reason for such poor yield was that the top layer of the bottom mirror was a layer of SiO_2. Likely due to surface energy reasons, we have had consistently poor results when buckling on top of the SiO_2 surface. This first wafer employed an a-Si-based upper (buckled) mirror, which limited the choice of pump laser wavelengths (to ~800 nm or higher) that could be used to excite the embedded SiO:Er layer.

In the second attempt, a uniform (un-patterned) and thicker (~100 nm) SiO:Er layer was employed. Furthermore, the a-Si-based upper mirror was replaced by a Ta_2O_5-based upper mirror in this case, so that shorter wavelength pump sources could be used. On this wafer, buckled devices with base diameters ranging from 50 µm to 70µm resulted in a moderate yield, and many of these domes exhibited a high degree of cylindrical symmetry. However, in spite of various attempts to increase

the upper mirror reflectance (through addition of additional mirror periods), the optical properties of these cavities were not of very high quality. Speculatively, this was attributed to a combination of high film loss (possibly due to problems with the sputtering system) and sub-optimal shape of the buckled cavities (possibly due to lower-than-optimal film stress). Nevertheless, a home-built microscope setup was assembled in order to measure the photoluminescence (PL) of the active SiO:Er layer in these cavities. This active layer was excited via a host-absorption-mediated energy transfer process, using an excitation wavelength of 473 nm (i.e., non-resonant with the Er^{3+} levels). These measurements confirmed the usual PL spectrum for Er^{3+} ions embedded in a glassy host, and also provided preliminary (although inconclusive) evidence of cavity-enhanced emission.

6.1.3 Pressure sensing with buckled dome microcavities

The upper mirror of the buckled dome microcavities is basically a flexible plate, and their interior cavities are inherently closed to (i.e., sealed from) the external environment. Given this, it was speculated that they could function as a pressure-sensing device with optical readout. Using previously fabricated high finesse buckled cavities from [83,84], which were fabricated by the guided assembly of circular delamination buckles, we were able to measure the effects of ambient pressure changes on the optical resonances. We restricted our study and measurements to domes of 50 µm and 100 µm size only. The predicted pressure sensitivity and vibrational resonance frequencies were described and showed a good agreement with experimental results. Both 50 µm and 100 µm domes showed a linear response to pressure changes, with a pressure sensitivity for 50 µm and 100 µm domes of ~ 0.08 nm/kPa and 0.7 nm/kPa, respectively. A tuned–to–slope technique (same as that utilized in the Refs. [171,172]) was used to observe the mechanical/vibrational resonance spectra for those domes. The vibrational resonances were found to be 10.9 MHz and 2.9 MHz for 50 µm and 100 µm domes, respectively. Such high vibrational resonance frequencies make these devices promising for the detection of dynamic pressure signals, such as ultrasound imaging.

6.2 **Future work**

6.2.1 Erbium emitters in buckled dome cavities

To exploit the Erbium-doped silicon monoxide for buckled dome microcavities, several issues must be addressed and resolved. For example, it may be possible to improve the optical properties of the active layer film. In the current work, the SiO:Er film was fabricated via thermal evaporation, while the Ta_2O_5 and SiO_2 films were deposited using a reactive sputtering system. It might be better in the future to also deposit the Er-doped silicon monoxide film using a reactive co-sputtering system without the breaking vacuum. It should be reiterated that the SiO:Er material system was chosen mainly for its low-temperature processing and ease of integration into the existing buckling process. In future work, it will be interesting (and necessary for some applications) to explore alternative material systems. For example, erbium-doped silicon nitride has recently been shown to provide a 3-4 orders of magnitude higher emission than erbium-doped SiO_2 [173,174]. Thus, it might be interesting to explore Er-doped silicon-rich silicon nitride (SRN) deposited using reactive sputtering as an alternative to the Er-doped silicon monoxide films studied here. Recent work by Maria *et al*. [48] investigated Er-doped silicon nitride as an emitter inside photonic crystals and achieved a 20-fold enhancement of Photoluminescence at the PC cavity. However, for many CQED applications, it will be necessary to use crystalline hosts (e.g. Y_2O_3 [175]) as discussed in Chapter 4. Thus, techniques for integrating such crystalline films, or possibly nanocrystals, into the buckling process will ultimately need to be developed.

We also encountered issues with the deposition of our Ta_2O_5, and SiO_2 films. In early 2020, our group modified the standard recipe (including background pressure) used to deposit these films, due to an observed drop in the compressive stress of the films. However, this adjustment might have resulted in a degradation of the optical properties (e.g., some of the films had a cloudy appearance, See Figure A.5 in Appendix A for more detail, and also details in chapter 4), which would have a direct influence on the reflectivity of our mirrors. Some of the problems encountered might also be attributable to the use of a sputtering system in a shared-use facility, which causes chamber conditions to vary outside of our control and required the modification of our film deposition recipes. In some cases, this modification reduced the stress of our films and quite likely affected the yield of our buckling process. The further optimization of the stress in these films is the subject of an ongoing effort in our research group.

Finally, it is worth mentioning that significant ongoing efforts in our group are aimed at further material optimization of the buckled-dome cavities. For example, by replacing the a-Si films used to date with hydrogenated a-Si (a-Si:H) films, there is the potential to achieve 3-4 orders of magnitude reduction in absorption loss at 1550 nm wavelength. Additionally, this might also enable the use of omnidirectional a-Si:H/SiO_2 based mirrors at shorter wavelengths of interest (e.g., 780 nm) for many candidate emitters in CQED applications.

6.2.2 Pressure sensing

As shown in Chapter 5, buckled dome microcavities are a promising new type of optical pressure sensor, with the potential for highly sensitive detection of high-speed (dynamic) pressure phenomena. In work described, all experiments were carried out in a lab environment and on an optical bench. In the future, it might be interesting to develop these buckled dome microcavities such that they can be placed on the end facet of an optical fiber, which would make them suitable as in-situ pressure sensors for a host of biomedical and structural engineering applications. Due to high finesse, high vibrational resonance frequencies, low cost, and small size of these buckled domes microcavities, they have many significant advantages in areas such as biomedical instrumentation, and photoacoustic imaging [176,177]. Another important factor that often has an impact on pressure sensitivity is temperature cross-sensitivity [143,150]. Future experiments could address this problem by adding another sensor responsible for detecting and normalizing temperature. As discussed in Chapter 5, this could possibly be achieved by using or secondary buckled microcavity with a known temperature dependence , but with holes etched through the upper mirror so that its response is insensitive to pressure.

Bibliography

1. T. W. Allen, J. Silverstone, N. Ponnampalam, T. Olsen, A. Meldrum, and R. G. DeCorby, "High-finesse cavities fabricated by buckling self-assembly of a-Si/SiO2 multilayers," Opt. Express, OE **19**, 18903–18909 (2011).
2. S. Noda, M. Fujita, and T. Asano, "Spontaneous-emission control by photonic crystals and nanocavities," Nature Photonics **1**, 449–458 (2007).
3. A. V. Akimov, A. Mukherjee, C. L. Yu, D. E. Chang, A. S. Zibrov, P. R. Hemmer, H. Park, and M. D. Lukin, "Generation of single optical plasmons in metallic nanowires coupled to quantum dots," Nature **450**, 402–406 (2007).
4. A. Laucht, F. Hofbauer, N. Hauke, J. Angele, S. Stobbe, M. Kaniber, G. Böhm, P. Lodahl, M.-C. Amann, and J. J. Finley, "Electrical control of spontaneous emission and strong coupling for a single quantum dot," New J. Phys. **11**, 023034 (2009).
5. T. Galfsky, Z. Sun, C. R. Considine, C.-T. Chou, W.-C. Ko, Y.-H. Lee, E. E. Narimanov, and V. M. Menon, "Broadband Enhancement of Spontaneous Emission in Two-Dimensional Semiconductors Using Photonic Hypercrystals," Nano Lett. **16**, 4940–4945 (2016).
6. J. H. Jerman and D. J. Clift, "Miniature Fabry-Perot interferometers micromachined in silicon for use in optical fiber WDM systems," in *TRANSDUCERS '91: 1991 International Conference on Solid-State Sensors and Actuators. Digest of Technical Papers* (1991), pp. 372–375.
7. C. Santori, M. Pelton, G. Solomon, Y. Dale, and Y. Yamamoto, "Triggered Single Photons from a Quantum Dot," Phys. Rev. Lett. **86**, 1502–1505 (2001).
8. M. Moskovits, "Surface-enhanced spectroscopy," Rev. Mod. Phys. **57**, 783–826 (1985).
9. D. J. Heinzen, J. J. Childs, J. E. Thomas, and M. S. Feld, "Enhanced and inhibited visible spontaneous emission by atoms in a confocal resonator," Phys. Rev. Lett. **58**, 1320–1323 (1987).
10. F. D. Martini, G. Innocenti, G. R. Jacobovitz, and P. Mataloni, "Anomalous Spontaneous Emission Time in a Microscopic Optical Cavity," Phys. Rev. Lett. **59**, 2955–2958 (1987).
11. G. S. Solomon, M. Pelton, and Y. Yamamoto, "Single-mode Spontaneous Emission from a Single Quantum Dot in a Three-Dimensional Microcavity," Phys. Rev. Lett. **86**, 3903–3906 (2001).
12. D. Kleppner, "Inhibited Spontaneous Emission," Phys. Rev. Lett. **47**, 233–236 (1981).
13. E. Yablonovitch, "Inhibited Spontaneous Emission in Solid-State Physics and Electronics," Phys. Rev. Lett. **58**, 2059–2062 (1987).
14. E. M. Purcell, "Proceedings of the American Physical Society," Phys. Rev. **69**, 674 (1946).
15. J. D. Joannopoulos, ed., *Photonic Crystals: Molding the Flow of Light*, 2nd ed (Princeton University Press, 2008).
16. P. Lodahl, A. Floris van Driel, I. S. Nikolaev, A. Irman, K. Overgaag, D. Vanmaekelbergh, and W. L. Vos, "Controlling the dynamics of spontaneous emission from quantum dots by photonic crystals," Nature **430**, 654–657 (2004).
17. Y. Dumeige, R. Alléaume, P. Grangier, F. Treussart, and J.-F. Roch, "Controling the single-diamond nitrogen-vacancy color center photoluminescence spectrum with a Fabry–Perot microcavity," New J. Phys. **13**, 025015 (2011).
18. E. Janitz, M. Ruf, M. Dimock, A. Bourassa, J. Sankey, and L. Childress, "Fabry-Perot microcavity for diamond-based photonics," Phys. Rev. A **92**, 043844 (2015).
19. L. Weiss, A. Gritsch, B. Merkel, and A. Reiserer, "Erbium dopants in nanophotonic silicon waveguides," Optica, OPTICA **8**, 40–41 (2021).
20. B. Merkel, A. Ulanowski, and A. Reiserer, "Coherent and Purcell-Enhanced Emission from Erbium Dopants in a Cryogenic High- Q Resonator," Phys. Rev. X **10**, 041025 (2020).

21.   E. Dulkeith, A. C. Morteani, T. Niedereichholz, T. A. Klar, J. Feldmann, S. A. Levi, F. C. J. M. van Veggel, D. N. Reinhoudt, M. Möller, and D. I. Gittins, "Fluorescence Quenching of Dye Molecules near Gold Nanoparticles: Radiative and Nonradiative Effects," Phys. Rev. Lett. **89**, 203002 (2002).

22.   Nanguo Liu, B. S. Prall, and V. I. Klimov, "Hybrid gold/silica/nanocrystal-quantum-dot superstructures : Synthesis and analysis of semiconductor-metal interactions," Journal of the American Chemical Society **128**, 15362–15363 (2006).

23.   O. G. Tovmachenko, C. Graf, D. J. van den Heuvel, A. van Blaaderen, and H. C. Gerritsen, "Fluorescence Enhancement by Metal-Core/Silica-Shell Nanoparticles," Adv. Mater. **18**, 91–95 (2006).

24.   M. Ringler, A. Schwemer, M. Wunderlich, A. Nichtl, K. Kürzinger, T. A. Klar, and J. Feldmann, "Shaping Emission Spectra of Fluorescent Molecules with Single Plasmonic Nanoresonators," Phys. Rev. Lett. **100**, 203002 (2008).

25.   K. J. Russell, T.-L. Liu, S. Cui, and E. L. Hu, "Large spontaneous emission enhancement in plasmonic nanocavities," Nature Photon **6**, 459–462 (2012).

26.   N. Maccaferri, G. Barbillon, A. Nana Koya, G. Lu, G. P. Acuna, and D. Garoli, "Recent advances in plasmonic nanocavities for single-molecule spectroscopy," Nanoscale Advances **3**, 633–642 (2021).

27.   M. Pelton, "Modified spontaneous emission in nanophotonic structures," Nature Photonics **9**, 427–435 (2015).

28.   J. Gomez Velez and A. Muller, "Purcell-enhanced microcavity Raman scattering from pressurized gases," Appl. Phys. Lett. **112**, 041107 (2018).

29.   B. Petrak, J. Cooper, K. Konthasinghe, M. Peiris, N. Djeu, A. J. Hopkins, and A. Muller, "Isotopic gas analysis through Purcell cavity enhanced Raman scattering," Appl. Phys. Lett. **108**, 091107 (2016).

30.   B. Petrak, N. Djeu, and A. Muller, "Purcell-enhanced Raman scattering from atmospheric gases in a high-finesse microcavity," Phys. Rev. A **89**, 023811 (2014).

31.   T. P. Purdy and D. M. Stamper-Kurn, "Integrating cavity quantum electrodynamics and ultracold-atom chips with on-chip dielectric mirrors and temperature stabilization," Appl. Phys. B **90**, 401–405 (2008).

32.   Y. Colombe, T. Steinmetz, G. Dubois, F. Linke, D. Hunger, and J. Reichel, "Strong atom–field coupling for Bose–Einstein condensates in an optical cavity on a chip," Nature **450**, 272–276 (2007).

33.   D. Englund, A. Faraon, I. Fushman, N. Stoltz, P. Petroff, and J. Vucković, "Controlling cavity reflectivity with a single quantum dot," Nature **450**, 857–861 (2007).

34.   A. Faraon, P. E. Barclay, C. Santori, K.-M. C. Fu, and R. G. Beausoleil, "Resonant enhancement of the zero-phonon emission from a colour centre in a diamond cavity," Nature Photonics **5**, 301–305 (2011).

35.   P. E. Barclay, K.-M. C. Fu, C. Santori, and R. G. Beausoleil, "Chip-based microcavities coupled to nitrogen-vacancy centers in single crystal diamond," Appl. Phys. Lett. **95**, 191115 (2009).

36.   D. Englund, B. Shields, K. Rivoire, F. Hatami, J. Vučković, H. Park, and M. D. Lukin, "Deterministic Coupling of a Single Nitrogen Vacancy Center to a Photonic Crystal Cavity," Nano Lett. **10**, 3922–3926 (2010).

37.   J. Riedrich-Möller, L. Kipfstuhl, C. Hepp, E. Neu, C. Pauly, F. Mücklich, A. Baur, M. Wandt, S. Wolff, M. Fischer, S. Gsell, M. Schreck, and C. Becher, "One- and two-dimensional photonic crystal microcavities in single crystal diamond," Nature Nanotechnology **7**, 69–74 (2012).

38.   T. T. Tran, K. Bray, M. J. Ford, M. Toth, and I. Aharonovich, "Quantum emission from hexagonal boron nitride monolayers," Nature Nanotechnology **11**, 37–41 (2016).

39.   N. R. Jungwirth, B. Calderon, Y. Ji, M. G. Spencer, M. E. Flatté, and G. D. Fuchs, "Temperature Dependence of Wavelength Selectable Zero-Phonon Emission from Single Defects in Hexagonal Boron Nitride," Nano Lett. **16**, 6052–6057 (2016).

40.   L. J. Martínez, T. Pelini, V. Waselowski, J. R. Maze, B. Gil, G. Cassabois, and V. Jacques, "Efficient single photon emission from a high-purity hexagonal boron nitride crystal," Phys. Rev. B **94**, 121405 (2016).

41.   K. Konthasinghe, C. Chakraborty, N. Mathur, L. Qiu, A. Mukherjee, G. D. Fuchs, and A. N. Vamivakas, "Rabi oscillations and resonance fluorescence from a single hexagonal boron nitride quantum emitter," Optica, OPTICA **6**, 542–548 (2019).

42.   S. Ogawa, "Control of Light Emission by 3D Photonic Crystals," Science **305**, 227–229 (2004).

43.   M. J. Ventura and M. Gu, "Engineering Spontaneous Emission in a Quantum-Dot-Doped Polymer Nanocomposite with Three-Dimensional Photonic Crystals," Adv. Mater. **20**, 1329–1332 (2008).

44.   M. D. Leistikow, A. P. Mosk, E. Yeganegi, S. R. Huisman, A. Lagendijk, and W. L. Vos, "Inhibited Spontaneous Emission of Quantum Dots Observed in a 3D Photonic Band Gap," Phys. Rev. Lett. **107**, 193903 (2011).

45.   L. A. Woldering, R. W. Tjerkstra, H. V. Jansen, I. D. Setija, and W. L. Vos, "Periodic arrays of deep nanopores made in silicon with reactive ion etching and deep UV lithography," Nanotechnology **19**, 145304 (2008).

46.   R. V. Nair, A. K. Tiwari, S. Mujumdar, and B. N. Jagatap, "Photonic-band-edge-induced lasing in self-assembled dye-activated photonic crystals," Phys. Rev. A **85**, 023844 (2012).

47.   Z. Wu, Z. Mi, P. Bhattacharya, T. Zhu, and J. Xu, "Enhanced spontaneous emission at 1.55μm from colloidal PbSe quantum dots in a Si photonic crystal microcavity," Applied Physics Letters **90**, 171105 (2007).

48.   M. Makarova, V. Sih, J. Warga, R. Li, L. Dal Negro, and J. Vuckovic, "Enhanced light emission in photonic crystal nanocavities with Erbium-doped silicon nanocrystals," Appl. Phys. Lett. **92**, 161107 (2008).

49.   Y. Gong, M. Makarova, S. Yerci, R. Li, B. Baek, S. W. Nam, R. H. Hadfield, V. Zwiller, J. Vucˇkovic, and L. D. Negro, "Linewidth narrowing and Purcell enhancement in photonic crystal cavities on an Er-doped silicon nitride platform," **18**, 2601–2612 (2010).

50.   Y. Wang, J. M. An, Y. D. Wu, and X. W. Hu, "Enhancement of luminescence from Er-doped Si by photonic crystal gradient double-heterostructure microcavity," Optics & Laser Technology **89**, 69–74 (2017).

51.   P. St. J. Russell, S. Tredwell, and P. J. Roberts, "Full photonic bandgaps and spontaneous emission control in 1D multilayer dielectric structures," Optics Communications **160**, 66–71 (1999).

52.   Y. Xu, W. Liang, A. Yariv, J. G. Fleming, and S.-Y. Lin, "High-quality-factor Bragg onion resonators with omnidirectional reflector cladding," Opt. Lett., OL **28**, 2144–2146 (2003).

53.   W. Liang, Y. Huang, A. Yariv, Y. Xu, and S.-Y. Lin, "Modification of spontaneous emission in Bragg onion resonators," Opt. Express, OE **14**, 7398–7419 (2006).

54.   D. Hunger, T. Steinmetz, Y. Colombe, C. Deutsch, T. W. Hänsch, and J. Reichel, "Fiber Fabry-Perot cavity with high finesse," New Journal of Physics **12**, 065038 (2010).

55.   P. R. Dolan, G. M. Hughes, F. Grazioso, B. R. Patton, and J. M. Smith, "Femtoliter tunable optical cavity arrays," Opt. Lett., OL **35**, 3556–3558 (2010).

56.   G. W. Biedermann, F. M. Benito, K. M. Fortier, D. L. Stick, T. K. Loyd, P. D. D. Schwindt, C. Y. Nakakura, R. L. Jarecki, and M. G. Blain, "Ultrasmooth microfabricated mirrors for quantum information," Appl. Phys. Lett. **97**, 181110 (2010).

57.   M. Trupke, E. A. Hinds, S. Eriksson, E. A. Curtis, Z. Moktadir, E. Kukharenka, and M. Kraft, "Microfabricated high-finesse optical cavity with open access and small volume," Appl. Phys. Lett. **87**, 211106 (2005).

58.   A. Muller, E. B. Flagg, J. R. Lawall, and G. S. Solomon, "Ultrahigh-finesse, low-mode-volume Fabry-Perot microcavity," Opt. Lett., OL **35**, 2293–2295 (2010).

59.   H. Kaupp, C. Deutsch, H.-C. Chang, J. Reichel, T. W. Hänsch, and D. Hunger, "Scaling laws of the cavity enhancement for nitrogen-vacancy centers in diamond," Physical Review A **88**, (2013).

60.   A. Muller, E. B. Flagg, M. Metcalfe, J. Lawall, and G. S. Solomon, "Coupling an epitaxial quantum dot to a fiber-based external-mirror microcavity," Appl. Phys. Lett. **95**, 173101 (2009).

61.   J. Gallego, W. Alt, T. Macha, M. Martinez-Dorantes, D. Pandey, and D. Meschede, "Strong Purcell effect on a neutral atom trapped in an open fiber cavity," Physical Review Letters **121**, (2018).

62.   C. Derntl, M. Schneider, J. Schalko, A. Bittner, J. Schmiedmayer, U. Schmid, and M. Trupke, "Arrays of open, independently tunable microcavities," Opt. Express, OE **22**, 22111–22120 (2014).

63.   X. Hao, S. Tanaka, A. Masuda, J. Nakamura, K. Sudoh, K. Maenaka, H. Takao, and K. Higuchi, "Application of Silicon on Nothing Structure for Developing a Novel Capacitive Absolute Pressure Sensor," IEEE Sensors Journal **14**, 808–815 (2014).

64.   Z. Zhang, C. Liao, J. Tang, Y. Wang, Z. Bai, Z. Li, K. Guo, M. Deng, S. Cao, and Y. Wang, "Hollow-Core-Fiber-Based Interferometer for High-Temperature Measurements," IEEE Photonics Journal **9**, 1–9 (2017).

65.   F. Xu, D. Ren, X. Shi, C. Li, W. Lu, L. Lu, L. Lu, and B. Yu, "High-sensitivity Fabry–Perot interferometric pressure sensor based on a nanothick silver diaphragm," Opt. Lett., OL **37**, 133–135 (2012).

66.   J. Harris, P. Lu, H. Larocque, L. Chen, and X. Bao, "In-fiber Mach–Zehnder interferometric refractive index sensors with guided and leaky modes," Sensors and Actuators B: Chemical **206**, 246–251 (2015).

67.   M. Quan, J. Tian, and Y. Yao, "Ultra-high sensitivity Fabry–Perot interferometer gas refractive index fiber sensor based on photonic crystal fiber and Vernier effect," Opt. Lett., OL **40**, 4891–4894 (2015).

68.   Z. Li, P. Jia, G. Fang, H. Liang, T. Liang, W. Liu, and J. Xiong, "Microbubble-based fiber-optic Fabry-Perot pressure sensor for high-temperature application," Appl. Opt., AO **57**, 1738–1743 (2018).

69.   S. Pevec and D. Donlagic, "All-fiber, long-active-length Fabry-Perot strain sensor," Opt. Express, OE **19**, 15641–15651 (2011).

70.   S. Li, B. Yu, X. Wu, J. Shi, Q. Ge, G. Zhang, M. Guo, Y. Zhang, S. Fang, and C. Zuo, "Low-cost fiber optic extrinsic Fabry–Perot interferometer based on a polyethylene diaphragm for vibration detection," Optics Communications **457**, 124332 (2020).

71.   X. Zhou, F. Ma, H. Ling, B. Yu, W. Peng, and Q. Yu, "A compact hydrogen sensor based on the fiber-optic Fabry-Perot interferometer," Optics & Laser Technology **124**, 105995 (2020).

72.   Y. Yang, X. Zhang, H. Bai, H. Shao, H. Pan, F. Pang, and T. Wang, "Force sensors based on intrinsic fiber Fabry-Perot interferometer fabricated by the femtosecond laser," in (Optical Society of America, 2016), p. AS3E.3.

73.   L. Yuan, J. Huang, X. Lan, H. Wang, L. Jiang, and H. Xiao, "All-in-fiber optofluidic sensor fabricated by femtosecond laser assisted chemical etching," Opt. Lett., OL **39**, 2358–2361 (2014).

74.   D. C. Abeysinghe, S. Dasgupta, J. T. Boyd, and H. E. Jackson, "A novel MEMS pressure sensor fabricated on an optical fiber," IEEE Photonics Technology Letters **13**, 993–995 (2001).

75.   M. Li, M. Wang, and H. Li, "Optical MEMS pressure sensor based on Fabry-Perot interferometry," Opt. Express, OE **14**, 1497–1504 (2006).

76.   Y. Jiang, J. Li, Z. Zhou, X. Jiang, and D. Zhang, "Fabrication of All-SiC Fiber-Optic Pressure Sensors for High-Temperature Applications," Sensors (Basel) **16**, 1660 (2016).

77.   D. C. Sweeney, A. M. Schrell, Y. Liu, and C. M. Petrie, "Metal-embedded fiber optic sensor packaging and signal demodulation scheme towards high-frequency dynamic measurements in harsh environments," Sensors and Actuators A: Physical **312**, 112075 (2020).

78.   S. Pevec and D. Donlagic, "Miniature all-fiber Fabry–Perot sensor for simultaneous measurement of pressure and temperature," Appl. Opt., AO **51**, 4536–4541 (2012).

79.   W. Ma, Y. Jiang, and H. Gao, "Miniature all-fiber extrinsic Fabry–Pérot interferometric sensor for high-pressure sensing under high-temperature conditions," Meas. Sci. Technol. **30**, 025104 (2019).

80.   W. Ma, Y. Jiang, J. Hu, L. Jiang, T. Zhang, and T. Zhang, "Microelectromechanical system-based, high-finesse, optical fiber Fabry–Perot interferometric pressure sensors," Sensors and Actuators A: Physical **302**, 111795 (2020).

81.   E. Epp, N. Ponnampalam, W. Newman, B. Drobot, J. N. McMullin, A. F. Meldrum, and R. G. DeCorby, "Hollow Bragg waveguides fabricated by controlled buckling of Si/SiO2 multilayers," Opt. Express **18**, 24917 (2010).

82.   C. A. Potts, A. Melnyk, H. Ramp, M. H. Bitarafan, D. Vick, L. J. LeBlanc, J. P. Davis, and R. G. DeCorby, "Tunable open-access microcavities for on-chip cavity quantum electrodynamics," Appl. Phys. Lett. **108**, 041103 (2016).

83.   M. H. Bitarafan and R. G. DeCorby, "Small-mode-volume, channel-connected Fabry-Perot microcavities on a chip," Appl. Opt., AO **56**, 9992–9997 (2017).

84.   J. Maldaner, S. Al-Sumaidae, G. J. Hornig, L. J. LeBlanc, and R. G. DeCorby, "Liquid infiltration of monolithic open-access Fabry–Perot microcavities," Appl. Opt., AO **59**, 7125–7130 (2020).

85.   S. Al-Sumaidae, M. H. Bitarafan, C. A. Potts, J. P. Davis, and R. G. DeCorby, "Cooperativity enhancement in buckled-dome microcavities with omnidirectional claddings," Opt. Express, OE **26**, 11201–11212 (2018).

86.   M. H. Bitarafan, H. Ramp, T. W. Allen, C. Potts, X. Rojas, A. J. R. MacDonald, J. P. Davis, and R. G. DeCorby, "Thermomechanical characterization of on-chip buckled dome Fabry-Perot microcavities," J. Opt. Soc. Am. B, JOSAB **32**, 1214–1220 (2015).

87.   H. A. MacLeod, H. A. Macleod, and H. A. Macleod, *Thin-Film Optical Filters* (CRC Press, 2010).

88.   J. N. Winn, Y. Fink, S. Fan, and J. D. Joannopoulos, "Omnidirectional reflection from a one-dimensional photonic crystal," Opt. Lett., OL **23**, 1573–1575 (1998).

89.   Y. Fink, J. N. Winn, S. Fan, C. Chen, J. Michel, J. D. Joannopoulos, and E. L. Thomas, "A Dielectric Omnidirectional Reflector," Science **282**, 1679–1682 (1998).

90.   P. Yeh, *Optical Waves in Layered Media*, 2nd edition (Wiley-Interscience, 2005).

91.   P. Yeh and A. Yariv, "Bragg reflection waveguides," Optics Communications **19**, 427–430 (1976).

92.   B. E. A. Saleh, *Fundamentals of Photonics*, 2nd ed. (Wiley, 2007).

93.   S. O. Kasap, *Optoelectronics and Photonics: Principles and Practices*, 2nd ed (Pearson, 2013).

94.   J. T. Verdeyen, *Laser Electronics*, 3rd ed. (Prentice Hall, c1995.).

95.   "Gaussian beam," Wikipedia (2018).

96.   A. Yariv, *Photonics : Optical Electronics in Modern Communications /*, 6th ed. (Oxford University Press, 2007).

97.   M. Fox, *Quantum Optics : An Introduction*, Oxford Master Series in Physics (Oxford University Press, 2006).

98.   O. Svelto, *Principles of Lasers* (Springer US, 2010).

99.   A. Reiserer and G. Rempe, "Cavity-based quantum networks with single atoms and optical photons," Reviews of Modern Physics **87**, 1379–1418 (2015).

100.   K. J. Vahala, "Optical microcavities," Nature **424**, 839 (2003).

101.   M. H. Bitarafan, C. A. Potts, and R. G. DeCorby, "Cut-off-based dual-taper reflectors in on-chip hollow waveguides," Opt. Express, OE **25**, 5101–5106 (2017).

102.   A. Nunnenkamp, K. Borkje, J. G. E. Harris, and S. M. Girvin, "Cooling and squeezing via quadratic optomechanical coupling," Phys. Rev. A **82**, 021806 (2010).

103.   J. W. Hutchinson, M. D. Thouless, and E. G. Liniger, "Growth and configurational stability of circular, buckling-driven film delaminations," Acta Metallurgica et Materialia **40**, 295–308 (1992).
104.   A. V. Kavokin, J. J. Baumberg, G. Malpuech, and F. P. Laussy, *Microcavities* (Oxford University Press, 2017).
105.   Y. Yamamoto and R. E. Slusher, "Optical Processes in Microcavities," Physics Today **46**, 66 (2008).
106.   A. Kuhn and D. Ljunggren, "Cavity-based single-photon sources," Contemporary Physics **51**, 289–313 (2010).
107.   M. Bayer, T. L. Reinecke, F. Weidner, A. Larionov, A. McDonald, and A. Forchel, "Inhibition and Enhancement of the Spontaneous Emission of Quantum Dots in Structured Microresonators," Phys. Rev. Lett. **86**, 3168–3171 (2001).
108.   C. Hooijer, D. Lenstra, and A. Lagendijk, "Mode density inside an omnidirectional mirror is heavily directional but not small," Opt. Lett., OL **25**, 1666–1668 (2000).
109.   P. Bermel, J. D. Joannopoulos, Y. Fink, P. A. Lane, and C. Tapalian, "Properties of radiating pointlike sources in cylindrical omnidirectionally reflecting waveguides," Phys. Rev. B **69**, 035316 (2004).
110.   Y. Xu, W. Liang, A. Yariv, J. G. Fleming, and S.-Y. Lin, "Modal analysis of Bragg onion resonators," Opt. Lett., OL **29**, 424–426 (2004).
111.   M. H. Bitarafan, H. Ramp, C. Potts, T. W. Allen, J. P. Davis, and R. G. DeCorby, "Bistability in buckled dome microcavities," Opt. Lett., OL **40**, 5375–5378 (2015).
112.   S. E. Morin, Q. Wu, and T. W. Mossberg, "Cavity quantum electrodynamics at optical frequencies," Optics & Photonics News, OPN **3**, 8–14 (1992).
113.   K. A. Neyts, "Simulation of light emission from thin-film microcavities," J. Opt. Soc. Am. A, JOSAA **15**, 962–971 (1998).
114.   M. S. Tomaš, "Green function for multilayers: Light scattering in planar cavities," Phys. Rev. A **51**, 2545–2559 (1995).
115.   M. S. Tomaš and Z. Lenac, "Spontaneous-emission spectrum in an absorbing Fabry-Perot cavity," Phys. Rev. A **60**, 2431–2437 (1999).
116.   H. J. W. M. Hoekstra and H. B. H. Elrofai, "Theory of optical spontaneous emission rates in layered structures," Phys. Rev. E **71**, 046609 (2005).
117.   S. Nussmann, M. Hijlkema, B. Weber, F. Rohde, G. Rempe, and A. Kuhn, "Submicron Positioning of Single Atoms in a Microcavity," Phys. Rev. Lett. **95**, 173602 (2005).
118.   S. Johnson, P. R. Dolan, T. Grange, A. A. P. Trichet, G. Hornecker, Y. C. Chen, L. Weng, G. M. Hughes, A. A. R. Watt, A Auffèves, and J. M. Smith, "Tunable cavity coupling of the zero phonon line of a nitrogen-vacancy defect in diamond," New J. Phys. **17**, 122003 (2015).
119.   M. Jiang, J. A. Kurvits, Y. Lu, A. V. Nurmikko, and R. Zia, "Reusable Inorganic Templates for Electrostatic Self-Assembly of Individual Quantum Dots, Nanodiamonds, and Lanthanide-Doped Nanoparticles," Nano Lett. **15**, 5010–5016 (2015).
120.   R. Takei, S. Manako, E. Omoda, Y. Sakakibara, M. Mori, and T. Kamei, "Sub-1 dB/cm submicrometer-scale amorphous silicon waveguide for backend on-chip optical interconnect," Opt. Express, OE **22**, 4779–4788 (2014).
121.   J.-H. Kim, S. Aghaeimeibodi, C. J. K. Richardson, R. P. Leavitt, D. Englund, and E. Waks, "Hybrid Integration of Solid-State Quantum Emitters on a Silicon Photonic Chip," Nano Lett. **17**, 7394–7400 (2017).
122.   H.-Z. Song, K. Takemoto, T. Miyazawa, M. Takatsu, S. Iwamoto, T. Yamamoto, and Y. Arakawa, "Design of Si/SiO_2 micropillar cavities for Purcell-enhanced single photon emission at 155 µm from InAs/InP quantum dots," Optics Letters **38**, 3241 (2013).

123. M. Humer, R. Guider, W. Jantsch, and T. Fromherz, "Integration, photostability and spontaneous emission rate enhancement of colloidal PbS nanocrystals for Si-based photonics at telecom wavelengths," Opt. Express, OE **21**, 18680–18688 (2013).

124. E. Miyazono, I. Craiciu, A. Arbabi, T. Zhong, and A. Faraon, "Coupling erbium dopants in yttrium orthosilicate to silicon photonic resonators and waveguides," Opt. Express, OE **25**, 2863–2871 (2017).

125. Z. Zhou, B. Yin, and J. Michel, "On-chip light sources for silicon photonics," Light: Science & Applications **4**, e358–e358 (2015).

126. I. Aharonovich, D. Englund, and M. Toth, "Solid-state single-photon emitters," Nature Photonics **10**, 631–641 (2016).

127. F. Iacona, G. Franzò, E. C. Moreira, and F. Priolo, "Silicon nanocrystals and Er3+ ions in an optical microcavity," Journal of Applied Physics **89**, 8354–8356 (2001).

128. P. G. Kik, A. Polman, S. Libertino, and S. Coffa, "Design and performance of an erbium-doped silicon waveguide detector operating at 1.5 /spl mu/m," Journal of Lightwave Technology **20**, 862–867 (2002).

129. N. Gisin, G. Ribordy, W. Tittel, and H. Zbinden, "Quantum cryptography," Rev. Mod. Phys. **74**, 145–195 (2002).

130. J. L. O'Brien, A. Furusawa, and J. Vučković, "Photonic quantum technologies," Nature Photonics **3**, 687–695 (2009).

131. A. Hryciw, C. Blois, A. Meldrum, T. Clement, R. DeCorby, and Q. Li, "Photoluminescence from Er-doped silicon oxide microcavities," Optical Materials **28**, 873–878 (2006).

132. F. Lenz, A. Hryciw, R. DeCorby, and A. Meldrum, "Reversing the temperature dependence of the sensitized Er3+ luminescence intensity," Appl. Phys. Lett. **95**, 091909 (2009).

133. Y. Peng, H. Ye, Z. Li, M. Motevalli, I. Hernández, W. P. Gillin, and P. B. Wyatt, "Visible-Range Sensitization of Er $^{3+}$ -Based Infrared Emission from Perfluorinated 2-Acylphenoxide Complexes," The Journal of Physical Chemistry Letters **5**, 1560–1563 (2014).

134. E. Miyazono, T. Zhong, I. Craiciu, J. M. Kindem, and A. Faraon, "Coupling of erbium dopants to yttrium orthosilicate photonic crystal cavities for on-chip optical quantum memories," Appl. Phys. Lett. **108**, 011111 (2016).

135. F. Priolo, G. Franzò, F. Iacona, D. Pacifici, and V. Vinciguerra, "Excitation and non-radiative de-excitation processes in Er-doped Si nanocrystals," Materials Science and Engineering: B **81**, 9–15 (2001).

136. M. Fujii, M. Yoshida, Y. Kanzawa, S. Hayashi, and K. Yamamoto, "1.54 μm photoluminescence of Er3+ doped into SiO2 films containing Si nanocrystals: Evidence for energy transfer from Si nanocrystals to Er3+," Appl. Phys. Lett. **71**, 1198–1200 (1997).

137. J. H. Shin, S. Seo, and S.-J. Lee, "Effect of hydrogenation on room-temperature 1.54 μm Er3+ photoluminescent properties of erbium-doped silicon-rich silicon oxide," Appl. Phys. Lett. **73**, 3647–3649 (1998).

138. S.-I. Jun, T. E. McKnight, A. V. Melechko, M. L. Simpson, and P. D. Rack, "Characterisation of reactively sputtered silicon oxide for thin-film transistor fabrication," Electron. Lett. **41**, 822 (2005).

139. A. D. Melnyk, "Fabrication of visible range hollow Bragg waveguides," https://era.library.ualberta.ca/items/6e3320b4-ff66-4e38-93ab-7b156fe04e91.

140. C. A. Potts, "Integrated Devices for On-Chip Quantum Optics," https://era.library.ualberta.ca/items/6c168b6b-c717-43b4-bd55-c7aedc427245.

141. A. M. Vredenberg, N. E. J. Hunt, E. F. Schubert, D. C. Jacobson, J. M. Poate, and G. J. Zydzik, "Controlled Atomic Spontaneous Emission from Er 3+ in a Transparent Si/Si02 Microcavity," Phys. Rev. Lett. **71**, 517–520 (1993).

142.   P. Song, Z. Ma, J. Ma, L. Yang, J. Wei, Y. Zhao, M. Zhang, F. Yang, and X. Wang, "Recent Progress of Miniature MEMS Pressure Sensors," Micromachines **11**, 56 (2020).

143.   Q. Yu and X. Zhou, "Pressure sensor based on the fiber-optic extrinsic Fabry-Perot interferometer," Photonic Sens **1**, 72–83 (2011).

144.   E. Vorathin, Z. M. Hafizi, N. Ismail, and M. Loman, "Review of high sensitivity fibre-optic pressure sensors for low pressure sensing," Optics & Laser Technology **121**, 105841 (2020).

145.   B. Liu, J. Lin, H. Liu, A. Jin, and P. Jin, "Extrinsic Fabry-Perot fiber acoustic pressure sensor based on large-area silver diaphragm," Microelectronic Engineering **166**, 50–54 (2016).

146.   X. Qi, S. Wang, J. Jiang, K. Liu, X. Wang, Y. Yang, and T. Liu, "Fiber Optic Fabry-Perot Pressure Sensor With Embedded MEMS Micro-Cavity for Ultra-High Pressure Detection," Journal of Lightwave Technology **37**, 2719–2725 (2019).

147.   S. Watson, M. J. Gander, W. N. MacPherson, J. S. Barton, J. D. C. Jones, T. Klotzbuecher, T. Braune, J. Ott, and F. Schmitz, "Laser-machined fibers as Fabry-Perot pressure sensors," Appl. Opt., AO **45**, 5590–5596 (2006).

148.   J. Ma, W. Jin, H. L. Ho, and J. Y. Dai, "High-sensitivity fiber-tip pressure sensor with graphene diaphragm," Opt. Lett., OL **37**, 2493–2495 (2012).

149.   S. Ghildiyal, P. Ranjan, S. Mishra, R. Balasubramaniam, and J. John, "Fabry–Perot Interferometer-Based Absolute Pressure Sensor With Stainless Steel Diaphragm," IEEE Sensors Journal **19**, 6093–6101 (2019).

150.   W. Wang, N. Wu, Y. Tian, C. Niezrecki, and X. Wang, "Miniature all-silica optical fiber pressure sensor with an ultrathin uniform diaphragm," Opt. Express, OE **18**, 9006–9014 (2010).

151.   F. Guo, T. Fink, M. Han, L. Koester, J. Turner, and J. Huang, "High-sensitivity, high-frequency extrinsic Fabry-Perot interferometric fiber-tip sensors based on a thin silver diaphragm," Opt. Lett., OL **37**, 1505–1507 (2012).

152.   E. J. Eklund and A. M. Shkel, "Factors affecting the performance of micromachined sensors based on Fabry–Perot interferometry," J. Micromech. Microeng. **15**, 1770–1776 (2005).

153.   D. Guo, R. Lin, and W. Wang, "Gaussian-optics-based optical modeling and characterization of a Fabry-Perot microcavity for sensing applications," J Opt Soc Am A Opt Image Sci Vis **22**, 1577–1588 (2005).

154.   X. Wu and O. Solgaard, "Short-cavity multimode fiber-tip Fabry-Pérot sensors," Opt. Express, OE **21**, 14487–14499 (2013).

155.   D. M. Marques, J. A. Guggenheim, J. A. Guggenheim, J. A. Guggenheim, and P. R. T. Munro, "Angular Airy function: a model of Fabry-Perot etalons illuminated by arbitrary beams," Opt. Express, OE **29**, 24144–24150 (2021).

156.   Z. Wang, Y. Jiang, W. Ding, and R. Gao, "A White-Light Interferometry for the Measurement of High-Finesse Fiber Optic EFPI Sensors," IEEE Photonics Technology Letters **26**, 2138–2141 (2014).

157.   J. Hu, X. Sun, A. Agarwal, and L. C. Kimerling, "Design guidelines for optical resonator biochemical sensors," J. Opt. Soc. Am. B, JOSAB **26**, 1032–1041 (2009).

158.   T. Yoshie, L. Tang, and S.-Y. Su, "Optical Microcavity: Sensing down to Single Molecules and Atoms," Sensors (Basel) **11**, 1972–1991 (2011).

159.   M. H. Bitarafan and R. G. DeCorby, "On-Chip High-Finesse Fabry-Perot Microcavities for Optical Sensing and Quantum Information," Sensors (Basel) **17**, E1748 (2017).

160.   I. M. White and X. Fan, "On the performance quantification of resonant refractive index sensors," Opt. Express, OE **16**, 1020–1028 (2008).

161.   C. Coupeau, J. Grilhé, E. Dion, L. D. de Morais, and J. Colin, "Evidence of vacuum between buckled films and their substrates," Thin Solid Films **518**, 5233–5236 (2010).

162.   J. Colin, C. Coupeau, J. Durinck, A. Cimetière, and J. Grilhé, "Redeposition of a straight-sided buckle under pressure," Phys Rev E Stat Nonlin Soft Matter Phys **89**, 032410 (2014).

163. H. M. Jensen and M. D. Thouless, "Effects of residual stresses in the blister test," International Journal of Solids and Structures **30**, 779–795 (1993).
164. P. Goudeau, P. Villain, N. Tamura, and H. A. Padmore, "Mesoscale x-ray diffraction measurement of stress relaxation associated with buckling in compressed thin films," Appl. Phys. Lett. **83**, 51–53 (2003).
165. J. W. Hutchinson and Z. Suo, "Mixed Mode Cracking in Layered Materials," in *Advances in Applied Mechanics*, J. W. Hutchinson and T. Y. Wu, eds. (Elsevier, 1991), Vol. 29, pp. 63–191.
166. B. D. Hauer, C. Doolin, K. S. D. Beach, and J. P. Davis, "A general procedure for thermomechanical calibration of nano/micro-mechanical resonators," Annals of Physics **339**, 181–207 (2013).
167. D. Tosi, "Review and Analysis of Peak Tracking Techniques for Fiber Bragg Grating Sensors," Sensors **17**, 2368 (2017).
168. G. J. Hornig, S. Al-Sumaidae, J. Maldaner, L. Bu, and R. G. DeCorby, "Monolithically integrated membrane-in-the-middle cavity optomechanical systems," Opt. Express, OE **28**, 28113–28125 (2020).
169. J. A. Guggenheim, J. Li, T. J. Allen, R. J. Colchester, S. Noimark, O. Ogunlade, I. P. Parkin, I. Papakonstantinou, A. E. Desjardins, E. Z. Zhang, and P. C. Beard, "Ultrasensitive plano-concave optical microresonators for ultrasound sensing," Nature Photon **11**, 714–719 (2017).
170. Z. Li, A. K. Ilkhechi, and R. Zemp, "Transparent capacitive micromachined ultrasonic transducers (CMUTs) for photoacoustic applications," Opt. Express, OE **27**, 13204–13218 (2019).
171. L. Greuter, S. Starosielec, D. Najer, A. Ludwig, L. Duempelmann, D. Rohner, and R. J. Warburton, "A small mode volume tunable microcavity: Development and characterization," Appl. Phys. Lett. **105**, 121105 (2014).
172. P. H. Kim, C. Doolin, B. D. Hauer, A. J. R. MacDonald, M. R. Freeman, P. E. Barclay, and J. P. Davis, "Nanoscale torsional optomechanics," Appl. Phys. Lett. **102**, 053102 (2013).
173. S. Yerci, R. Li, S. O. Kucheyev, T. van Buuren, S. N. Basu, and L. Dal Negro, "Energy transfer and 1.54 µm emission in amorphous silicon nitride films," Appl. Phys. Lett. **95**, 031107 (2009).
174. R. Li, S. Yerci, and L. Dal Negro, "Temperature dependence of the energy transfer from amorphous silicon nitride to Er ions," Appl. Phys. Lett. **95**, 041111 (2009).
175. T. T. Van and J. P. Chang, "Controlled erbium incorporation and photoluminescence of Er-doped Y2O3," Appl. Phys. Lett. **87**, 011907 (2005).
176. K. Bremer, E. Lewis, G. Leen, B. Moss, S. Lochmann, and I. Mueller, "Feedback Stabilized Interrogation Technique for EFPI/FBG Hybrid Fiber-Optic Pressure and Temperature Sensors," IEEE Sensors Journal (2012).
177. D. Tosi, E. G. Macchi, G. Braschi, A. Cigada, M. Gallati, S. Rossi, S. Poeggel, G. Leen, and E. Lewis, "Fiber-optic combined FPI/FBG sensors for monitoring of radiofrequency thermal ablation of liver tumors: ex vivo experiments," Appl. Opt., AO **53**, 2136–2144 (2014).
178. R. Albrecht, A. Bommer, C. Deutsch, J. Reichel, and C. Becher, "Coupling of a single NV-center in diamond to a fiber-based microcavity," Physical Review Letters **110**, (2013).
179. A. Faraon, P. E. Barclay, C. Santori, K.-M. C. Fu, and R. G. Beausoleil, "Resonant enhancement of the zero-phonon emission from a color center in a diamond cavity," Nature Photonics **5**, 301–305 (2011).
180. E. Neu, D. Steinmetz, J. Riedrich-Möller, S. Gsell, M. Fischer, Matthias Schreck, and C. Becher, "Single photon emission from silicon-vacancy colour centres in chemical vapour deposition nano-diamonds on iridium," New J. Phys. **13**, 025012 (2011).
181. S. Koh, "Strategies for Controlled Placement of Nanoscale Building Blocks," Nanoscale Res Lett **2**, 519–545 (2007).

182.　D. Qin, Y. Xia, B. Xu, H. Yang, C. Zhu, and G. M. Whitesides, "Fabrication of Ordered Two-Dimensional Arrays of Micro- and Nanoparticles Using Patterned Self-Assembled Monolayers as Templates," Advanced Materials **11**, 1433–1437 (1999).

183.　S. Fan, W. Jiang, X. Li, H. Yu, B. Lei, Y. Shi, L. Yin, B. Chen, and H. Liu, "Fabrication of high-resolution reflective scale grating for an optical encoder using a patterned self-assembly process," J. Micromech. Microeng. **26**, 075015 (2016).

184.　E. Miele, M. Malerba, M. Dipalo, E. Rondanina, A. Toma, and F. De Angelis, "Controlling wetting and self-assembly dynamics by tailored hydrophobic and oleophobic surfaces," Adv. Mater. Weinheim **26**, 4179–4183 (2014).

Appendix A

Emitters inside the dome microcavities

A major goal of this project is to develop monolithic strategies to embed emitters, especially solid-state emitters, inside our buckled-dome cavities. A brief description of some early work towards this goal, not included in the main part of the thesis, is provided here. First, preliminary efforts aimed at the integration of fluorescent nanodiamonds are described. Second, preliminary efforts aimed at the fabrication of visible-range mirrors (i.e., designed for compatibility with the nanodiamond emission) is described.

A.1 Preliminary efforts to incorporate nanodiamonds

Diamond-based emitters (i.e., light-emitting defect centers in diamond hosts) coupled to tunable Fabry-Perot cavities offer a promising platform for quantum devices [60,178,179]. Nanodiamonds in colloidal solution, hosting efficient light emitters such as the well-known nitrogen-vacancy (NV) center defect [180] are now available commercially as colloidal solutions. Furthermore, various efforts to selectively position nanodiamonds onto patterned substrates have been described in the literature [119,181–184]. By combining electrostatic self-assembly principles [119] with patterned regions of low and high hydrophobicity, we had preliminary success in positioning nanodiamonds. The process that was attempted is depicted in Figure A.1
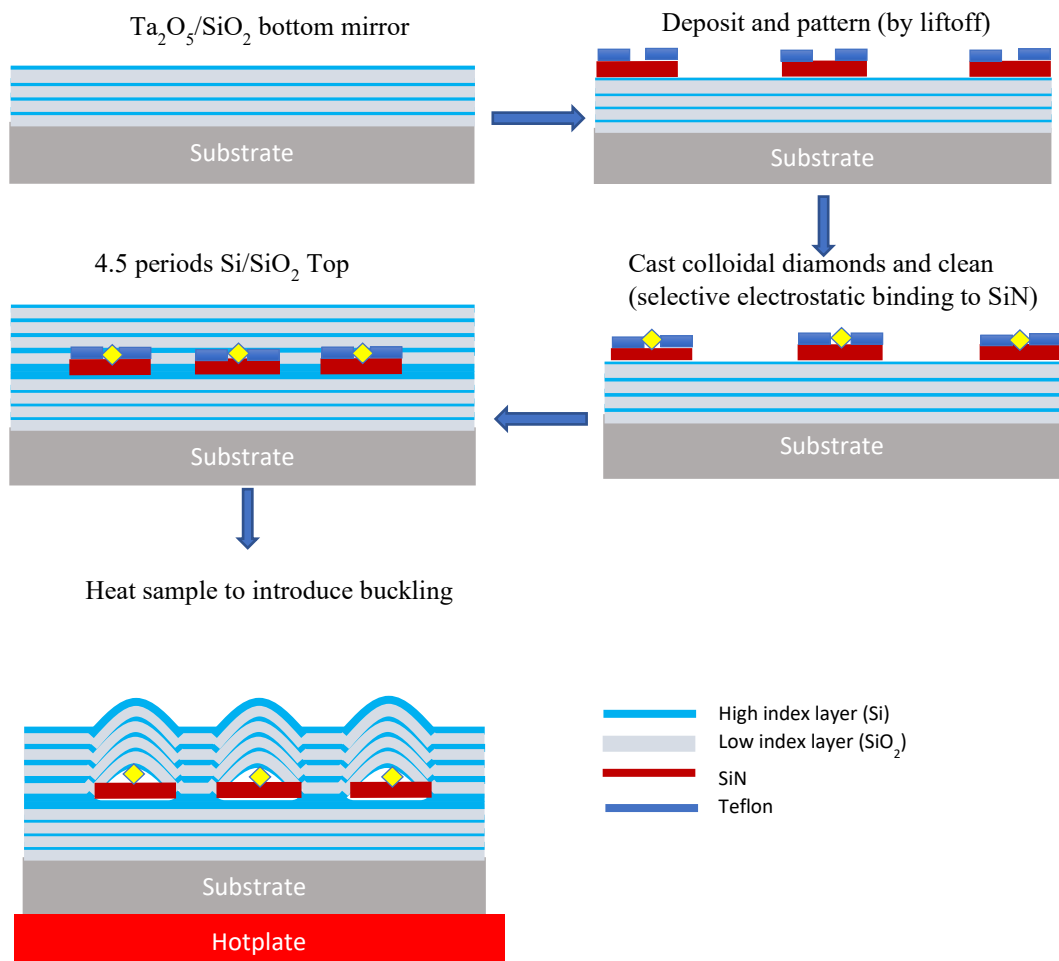
Figure A.1. Proposed process for embedding nanodiamond emitter 'pads' inside buckled dome cavities.

First, a silicon wafer was coated with a silicon nitride (SiN) film, which was chosen because SiN has a high 'iso-electric point' (IEP) value [119], implying that it will offer a strong electrostatic binding property for subsequently deposited diamond nanoparticles. On top of SiN, we patterned 'donut'-shaped fluorocarbon patterns; i.e., 'holes' with diameter 1-2 μm were patterned in the center of a typical circular fluorocarbon feature used to define the region of buckling for a dome microcavity (see Figure A.2). Next, a commercial colloidal solution of nanodiamonds (FND 35 nm, with typical emission wavelengths in the ~ 600 nm – 850 nm range) was drop-cast onto the substrate. A cleanroom wipe was used as a 'squeegee' across the surface, in order to remove the majority of the solution, and then the sample was cleaned with DI water. These samples were studied using a confocal fluorescence microscope system (Zeiss Stereo Discovery.V20 equipped with an Axiocam MRm camera). As shown in Figure A.3, there is some evidence (note the localized brighter red emission, presumably associated with the well-known NV-defect center

emission centred at ~640 nm wavelength) that nanodiamonds were 'trapped' in the holes at the centers of the fluorocarbon patterns, due to selective binding to the exposed SiN surface. Further analysis of these results, as well as efforts to fabricate nanodiamond-embedded buckled dome microcavities, is left for future work.
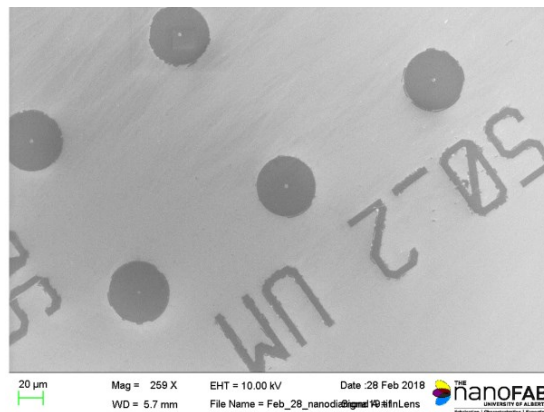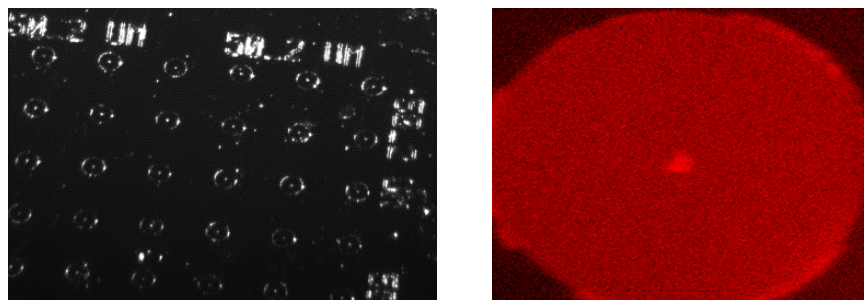

Figure A.2. SEM image of array 'donut'-shape for fluorocarbon patterns.

(a)   (b)

Figure A.3. Confocal fluorescence microscopy images of spatially patterned nanodiamonds.

A.2 Fabrication of a visible-range mirror

The primary motivation for this work was the development of a Fabry-Perot cavity with open access to the air cavity in the visible range. In order to create the open access cavity, we were involved in making holes from the top of the cavity, similar to the process described by Maldaner *et al.* [84]. First, the fabrication process was followed. The fabrication started with the deposition of an eight-period Bragg reflector onto a fused silica wafer, followed by etching the alignment marks. To prepare for the next step, the photoresist was spun coat, and circular dome features were patterned. After that, a low-adhesion fluorocarbon layer was deposited using the Bosch process, and the PR was lifted off. Finally, the second mirror was deposited using the same procedure as

used for the bottom mirror. Unfortunately, a deposition pressure adjustment for the Ta_2O_5 made the extinction coefficients quite a bit higher in magnitude than those previously reported by our group [139,140]. This negatively impacted the optical properties of the top mirror, which had a cloudy appearance, see Figure A.4 and Figure A.5. To mitigate this problem, we subsequently ran 4 test wafers at two different pressures (4 mT the new and 3.7 mT old pressure) with different O_2 flow rates. After that, the optical properties should have been checked. However, due to time constraints, this was left for future work.
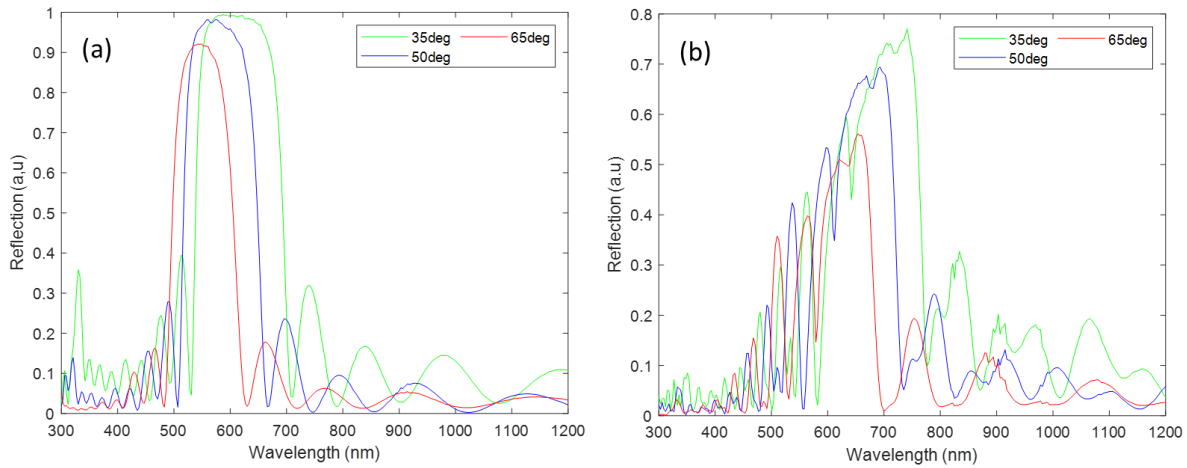
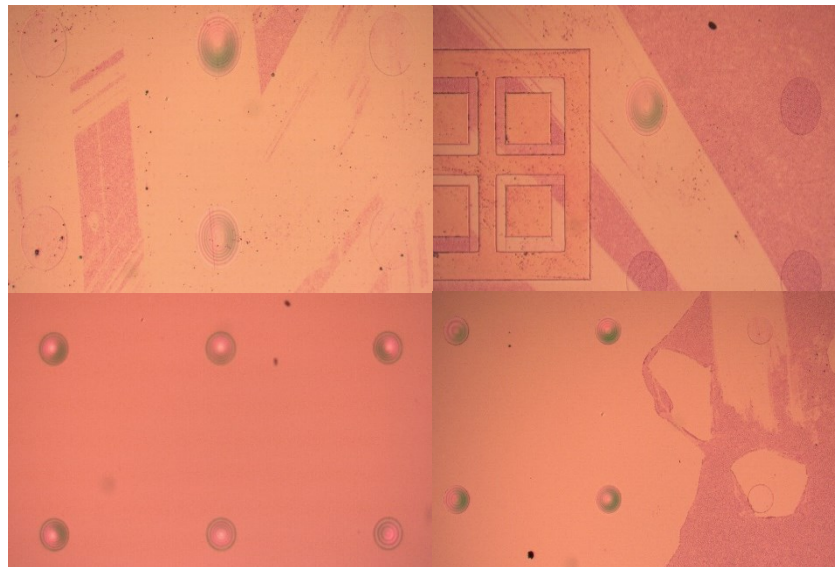Figure A.4. (a) Transmission scans the bottom mirror only. (b) Transmission scan for the top (cloudy mirror).

Figure A.5. Microscope Images show the cloudy area.

Appendix B

Pbs qdots inside buckled dome cavities

Here, we briefly desribe a method that were attempted in order to embed PbS quantum dots inside our cavities. In a parallel work within our group, the infiltration of a solvent (IPA) into our cavities via holes etched through the top mirror was demonstrated [84]. This motivated us to explore these same cavities for infiltration with PbS and PbSe quantum dots, which have attracted significant interest due to their high internal quantum efficiency and stability as infrared range emitters. First, we purchased PbS quantum dots in solution (Octane and Toluene). After that, we drop cast a little amount of PbS qdots on a microscope slide in order to test the PL using a microscope setup, see Figure B.1.
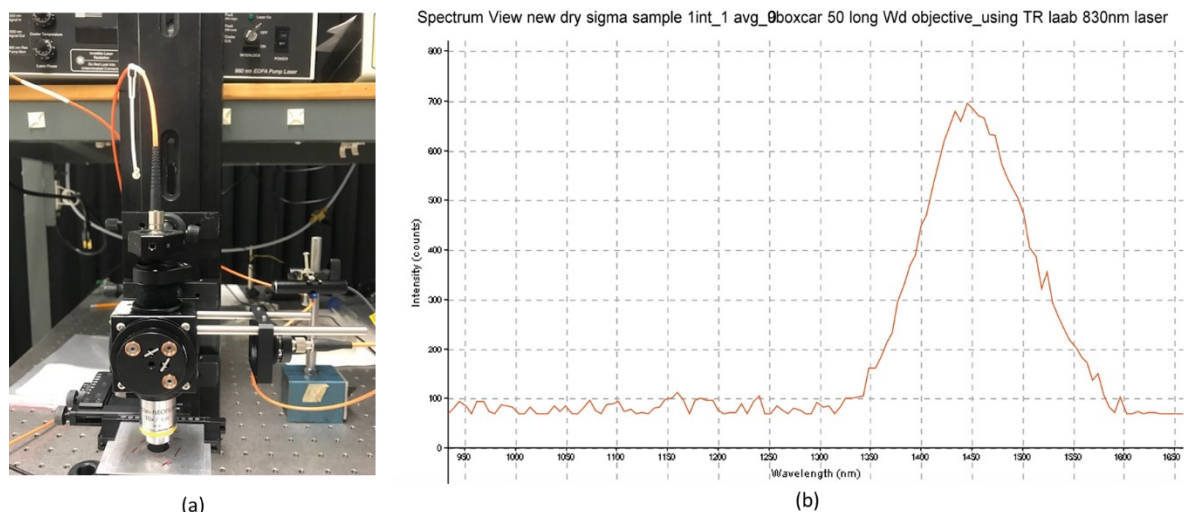

Figure B.1. (a) Microscope setup, (b) PL for PbS qdot.

We subsequently drop-cast a drop of the solution onto the previously mentioned chips containing domes with holes etched through their upper buckled mirror [84]. We hoped that some of the PbS quantum dots would infiltrate the cavities, and this would be evidenced by cavity-modified PL emission (see Figure B.2).
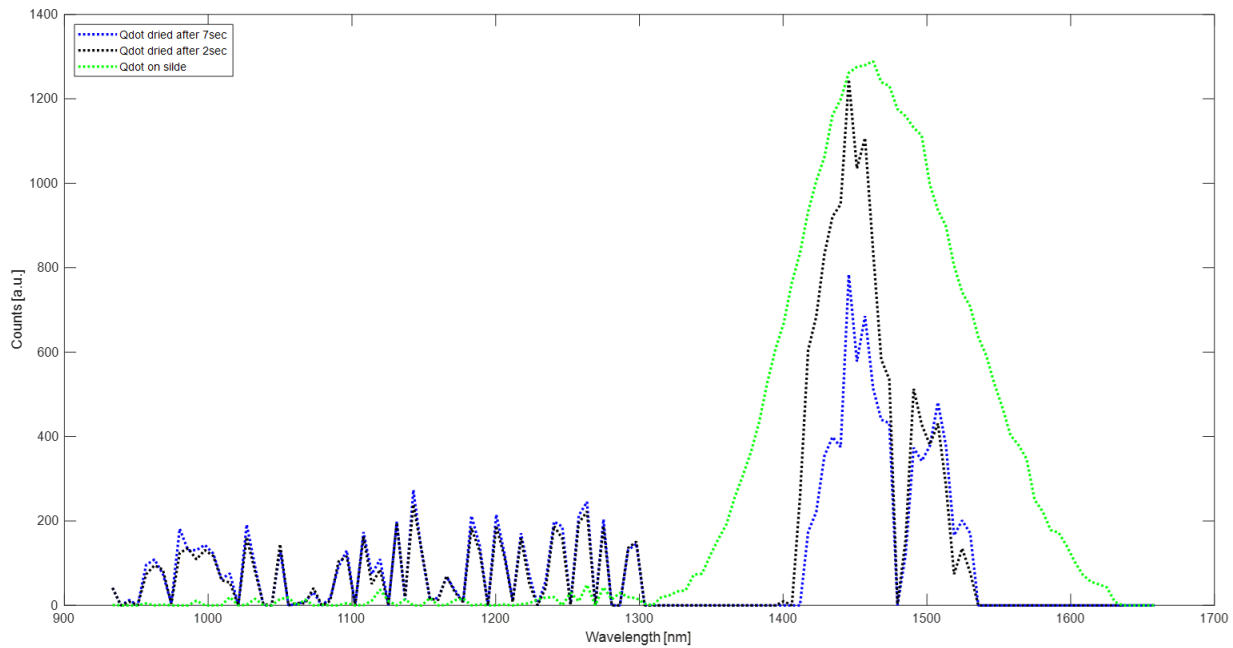
Figure B.2. showing the spectra of Pbs qdots

Appendix C

Pressure measurements for open access holes

The initial approach to measuring the adequate pressure on the microcavity was performed on both open and closed cavities. In order to see the effect of the pressure on the open-access cavity, we tried on several domes and measured the main resonance. Figure C.1 confirmed very little change in the main resonance when we applied the differential sets of pressure on a 100 μm based dome with four holes.
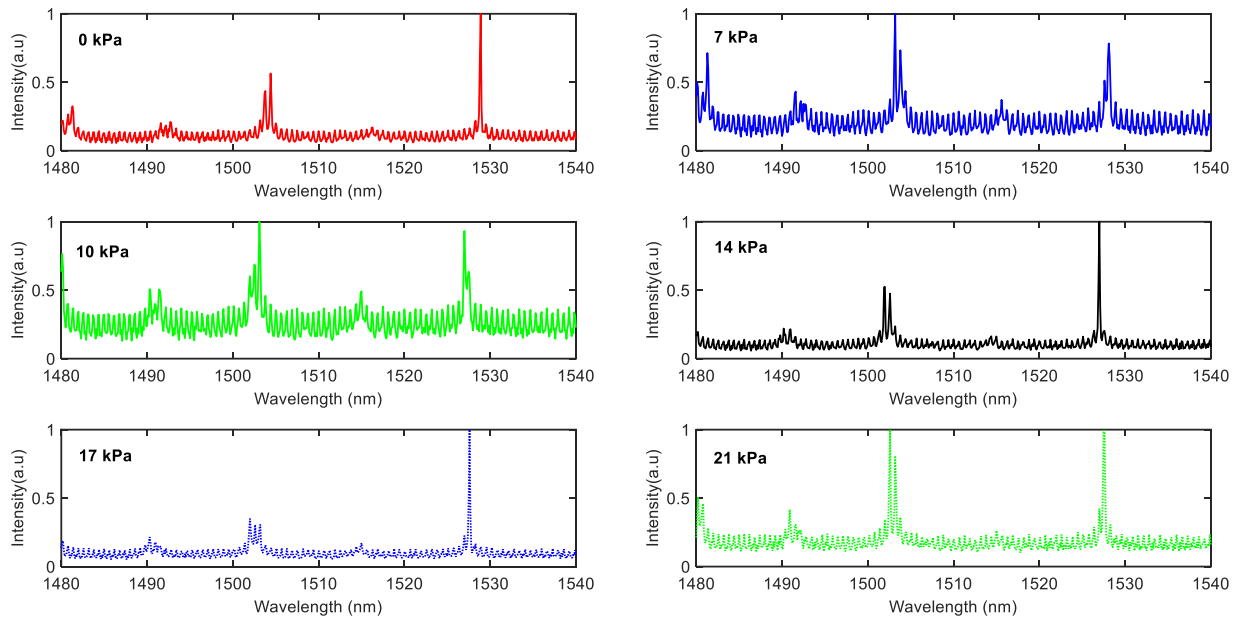

Figure C.1. shows the main resonance at differential pressure sets (as labeled inset) for 100 um dome with four holes.

We repeated the same procedure on other domes, and it shows the same behavior, with very little to no shift in the resonance (see Figure C.2). This verified that those domes with holes etched through their top mirrors are relatively insensitive to pressure.
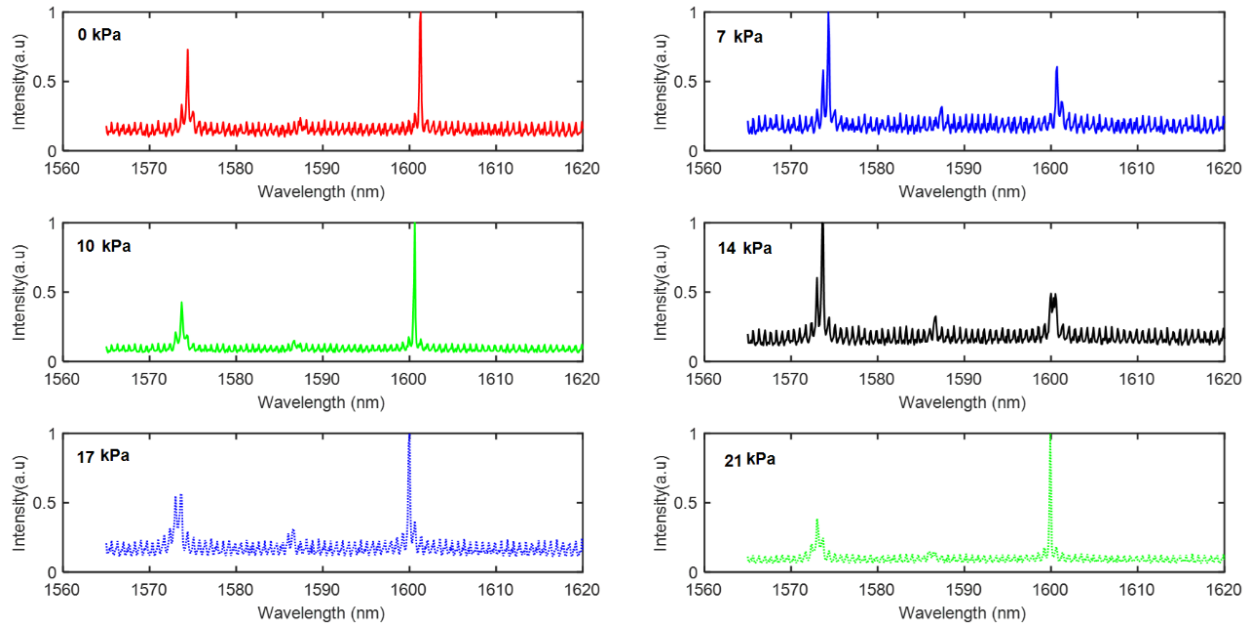
Figure C.2. shows the main resonance at differential pressure sets for 100 um dome with five holes.